FE-2476-1
Distribution Categories UC-90, UC-90g, and UC-93

GASEOUS ELECTRODE DEVELOPMENT

FINAL REPORT

M. S. Jones, Jr., E. P. Scannell,
K. Sathyanarayana, V. Thiagarajan,
R. Mallavarpu, A. J. Armstrong

REYNOLDS METALS COMPANY
ENERGY CONVERSION DIVISION
P. O. BOX 1200
SHEFFIELD, ALABAMA 35660

DECEMBER 1979

PREPARED FOR THE
UNITED STATES DEPARTMENT OF ENERGY
UNDER CONTRACT NO. EX-76-C-01-2476

ACKNOWLEDGEMENT

The participation of the following personnel in the accomplishment of this work is acknowledged and appreciated: Mr. J. O. Cook, Mr. K. R. King, and Mr. G. W. Thompson.

This project was originally initiated by Mr. M. T. Dooley who directed the program in its early phases. Important contributions to the program during this period were made by Dr. D. W. Cott, Mr. L. D. Carter, and Mr. G. E. Staats.

TABLE OF CONTENTS

TABLE OF CONTENTS (CONT.)

LIST OF FIGURES

LIST OF FIGURES (CONT.)

LIST OF FIGURES (CONT.)

LIST OF TABLES

ABSTRACT

One of the critical tasks in the commercial application of magnetohydrodynamics (MHD) topping power generation cycles is the development of appropriate long-life electrodes. Various solid electrodes developed thus far have shown short lifetime. However, the gaseous electrode concept being developed at Reynolds Metals Company had shown at bench scale the potential of offering an alternate solution to this major problem. The purpose of the present study is to optimize the gaseous electrode for use in an MHD generator and to test this optimum configuration in an operating MHD channel. This report summarizes the work performed by Reynolds Metals Company, Energy Conversion Division, on Gaseous Electrode Development under Department of Energy Contract No. EX-76-C-01-2476. The period of performance covered by this report is July 1, 1976, to June 30, 1979.

The arc gaseous electrode concept is based on the use of an arc source in the body of the MHD channel electrode, wherein the arc follows a helical path and generates a plasma which flows out of a long, thin slot cut parallel to the cylindrical annulus, to provide a low impedance path for the MHD current through the boundary layer so that electrode erosion due to arcing can be reduced.

Bench-scale tests on the arc plasma source were conducted. The effect of the parameters such as magnetic field, yaw angle with respect to the magnetic field, electrode geometry, and arc cathode materials were studied. Based on these studies, an optimum design was selected for testing in the MHD channel.

Tests were conducted with the arc gaseous electrode in the cathode wall of a diagonal conducting wall MHD generator at magnetic fields up to 3.83 Tesla, with a supersonic flow of combustion products seeded with 1.0 w/o of potassium. The measured MHD plasma conductivity varied between 12 and 22 S/m.

High-speed photography disclosed that the visible plasma ejected from the slot in the arc gaseous electrode into the MHD flow channel consisted of a series of puffs or blobs of plasma which lasted less than 120 microseconds, appearing randomly along about 2 mm of the slot, and at a period associated with the rotational frequency. Because of the small fraction of the time that the plasma was observed being injected into the channel, it was postulated that its effect on the MHD generator operation would be small.

Experiments were performed to confirm: (a) whether operation of the arc gaseous electrode had any effect on the MHD channel electrical characteristics; and, (b) whether changes in the channel transverse plasma current density, caused by switching the MHD generator load from open circuit to short circuit, had any effect on the arc gaseous electrode current. Aside from a very small (20%) change in current through the electrode frame where the arc gaseous electrode was located, no effects were found when the arc gaseous electrode was operated. For the change in electrode current observed, scatter of the data

was large. The variation in the data is due in large part to the fact that the split frame current was found to consist of a series of large pulses of current of 50 to 100 amperes which were about 100 microseconds in duration. Operation of the arc gaseous electrode did not change the spectrum of these pulses. It is speculated that the observed increase in the electrode frame current was due to modification of the electrode boundary layer caused by the injection of hot argon gas from the arc gaseous electrode into the boundary layer.

It is concluded from the experiments that were conducted with arc gaseous electrode in the channel, that the gaseous electrode concept holds promise, but if it is to be effectively implemented, it will require a plasma source which is stable, spatially uniform, and capable of operating continuously under MHD channel flow conditions. Because of the intermittent nature of the arc plasma source, no further development work on the arc gaseous electrode is recommended. However, further work on the development of the gaseous electrode system, because of its inherent advantage of long operating life, should be pursued with continuous plasma sources such as microwave discharges, R.F. discharges, or thermal sources such as flames.

1.0 OBJECTIVES AND SCOPE OF WORK

1.1 Overall Objective

The purpose of the program is to develop and demonstrate a gaseous electrode for magnetohydrodynamics (MHD) generators. This program is a continuation of in-house development work performed by Reynolds Metals Company (RMC) in 1974 and 1975 which demonstrated that it is possible to construct an arc plasma generator which could operate for extended periods of time (24-hour continuous tests were conducted). This plasma generator configuration was designed to be capable of being installed in the electrode of an MHD channel. Because of the selected geometry and orientation with respect to the magnetic field, the arc in this plasma generator travels in a helical path over the arc plasma generato electrodes. It was postulated that because of the arc movement electrode wear would be minimized. It was conjectured that the plasma generated by the arc gaseous electrode would carry the MHD generator electrode current, and thus reduce the erosion caused on the MHD channel electrode surfaces by the attachment of electric arcs between the MHD plasma and the electrode surface.

1.2 Contract Objective

The work involved under this contract was: (a) to establish baseline performance for the arc gaseous electrode system as a function of physical and material parameters; (b) to optimize an arc gaseous electrode configuration; and, (c) to test and evaluate the arc gaseous electrode performance in an MHD generator. This last objective had two major tasks. These were characterizing the MHD generator so that when the arc gaseous electrode was installed in the generator, baseline generator performance data were available upon which to judge any changes which might be observed when the arc gaseous electrode was operating. The other task was to improve existing channel flow computer programs so that they could provide analytical support for the analysis of the experimental data.

1.3 Program Results

1.3.1 Electrode Development

Development tests were performed in the RMC Electrode Development Facility (EDF) which screened different materials for use as the arc cathode. Copper, brass, thoriated tungsten, and molybdenum emerged as prime candidates based on their performance in terms of variation of magnetic field direction and strength. Thoriated tungsten and copper were eventually tested in the MHD generator.

Several internal geometrical variations were tested. The 1/4" cathodes were found to be superior to the 1/8" cathodes. It was also found that increasing the arc anode diameter near the ends reduced damage to the end insulators. It was found that injecting the arc gas tangentially into the anode cavity in the same direction as the arc rotation improved performance, and injecting inert gas into the ends of the arc cavity with angular momentum assisted in keeping the arc in the center of the assembly where its plasma could be injected into the MHD channel flow.

As part of this development, optical fiber systems with silicon photodiode detectors were used to monitor the rotation and translation of the arc. This system provided valuable insight into the internal operation of the arc gaseous electrode.

Special diagonal conducting wall MHD generator frames were constructed for testing both the 1/8" and 1/4" arc gaseous electrodes in the Generator Test Facility. The frame for the 1/4" arc cathode system also incorporated the optical fiber monitoring systems and provision for using a 4 mm x 4 mm coherent optical fiber bundle with a lens system so that the interior of the channel and the generator cathode surface which incorporated the arc gaseous electrode could be viewed while it is in operation.

1.3.2 Testing in the MHD Generator

Cold-flow testing of the 1/8" diameter arc cathode assembly in the MHD generator had just been completed on October 29, 1976, when an explosion of the liquid oxygen storage tank caused substantial damage to the Generator Test Facility and it was almost 18 months before testing in the GTF could be resumed. When checking out the MHD generator system, it was determined that the combustor volume was too small for the design flow, with the result the burning was incomplete and there was very low conductivity in the upstream end of the MHD channel. The combustor inadequacies were partially overcome by switching from diesel fuel to propane, so that faster burning would occur, and by reducing the N_2/O_2 ratio from 1.0 to about 0.3 so that the reduced mass flow resulted in a longer combustor residence time for the same heat release. Measurement of the conductivity showed levels of about 12 S/m at the channel entrance increasing to about 22 S/m in the downstream portion of the channel. While these conditions were not optimal, they did provide a baseline upon which the performance changes produced by operation of the arc gaseous electrode could be evaluated.

During the flow testing of the MHD generator, it was found that if the channel mass flow rate was greater than about 0.6 kg/sec, the flow became supersonic and at design flow there was insufficient MHD interaction to move the shock back upstream of the MHD channel for the flow to be subsonic. At full mass flow, the shock was at the downstream end of the channel.

When operated in the power producing mode, the maximum power generated by the channel was 11.9 kw delivered to an 11 ohm water-cooled load, rather than the 140 kw as designed.

After the characterization tests were completed, the arc gaseous electrode system was installed in the GTF and testing under MHD flow conditions was accomplished. Most data were taken with the 1/4" cathode, using either thoriated tungsten or copper as the arc cathode material. The arc electrode yaw angle with respect to the magnetic field was fixed at 25°. The arc gaseous electrode was operated in magnetic inductions of 1.4 to 3.84 Tesla. For all tests, the flow at the arc gaseous electrode was supersonic. It was found that in the MHD flow environment when the arc was shut off it would re-ignite at all magnetic fields when the power was restored. It did not require the radio frequency starter which was necessary in the bench-scale tests.

Under MHD channel operating conditions, three distinct criteria were used to evaluate whether the arc gaseous electrode was having any effect on the MHD channel performance. These criteria were:

(1) The effect of the arc gaseous electrode operation on the local MHD generator characteristics in the immediate vicinity of the arc gaseous electrode.

(2) The effect of the arc gaseous electrode on the overall performance of the MHD generator.

(3) The effect of the changes in the MHD generator characteristics on the arc gaseous electrode.

In addition, visual observation and high-speed photography of the electrode surface of the channel when the gaseous electrode was operating and measurement of time-resolved electrode current were used to evaluate the performance of the arc gaseous electrode.

It was observed that operation of the arc gaseous electrode did not cause any change in the channel axial voltage profile, as would be expected if the arc gaseous electrode had reduced the MHD cathode voltage drop. It was determined that there might be a slight increase (20%) in the transverse MHD current to the electrode frame containing the arc gaseous electrode when the arc gaseous electrode was operated. However, the data have such widely varying amplitudes that the differences are small and the probable errors of the two sets of data overlap. The effect, if real, is very small compared to the increase in current which would be expected if the arc gaseous electrode had overcome the MHD cathode boundary layer drop in such a small-sized channel.

When operating the MHD generator in a power producing mode, no change could be discerned in the generator open-circuit voltage or the short-circuit current when the arc gaseous electrode was either on or off. It was found that there was no discernable change in the arc current of the arc gaseous electrode when the transverse current density of the MHD duct was changed by switching the external generator load from open circuit to short circuit.

The high speed photographs disclose that visible plasma is emitted through the slot in the arc gaseous electrode in short puffs or blobs of plasma which exist for less than 120 microseconds, the minimum resolution time of the high-speed camera. These puffs appear randomly along the slot about every millisecond in agreement with the rotational frequencies. This suggests that the arc gaseous electrode could only be effective for one-tenth or less of the time and its performance could be improved by an electrode system incorporating a continuous plasma source.

During the course of the high-speed photography, intense, short-duration, bright spots were observed on the MHD generator cathode surface, suggesting that sparks were carrying the current from the central plasma to the electrodes through the boundary layer. Time-resolved measurements of the current through the split plate confirmed that the current was being carried as a series of spikes, with amplitudes up to 60 amperes recorded, and amplitudes up to 100 amperes observed, whereas the time average current was only about 6 amperes. Operation of the arc gaseous electrode did not produce a significant change in the pulse height distribution of the split frame current.

We must therefore conclude that the arc gaseous electrode under MHD channel conditions was incapable of delivering a continuous plasma and, hence, could not significantly modify or reduce the electrode boundary layer drop at the cathode of a diagonal conducting wall MHD channel. For this reason, it is concluded that the arc gaseous electrode, as presently conceived, cannot provide significant protection to the electrode surface, i.e., by reducing electrode erosion caused by arcing to the electrode from the plasma through the MHD flow boundary layer. Since this was postulated to be one of the principal advantages of the arc gaseous electrode, it is recommended that no further work be undertaken on the arc gaseous electrode at this time.

The concept of injecting plasma from a continuously operating plasma source at the interface between the electrode and the MHD plasma, so as to reduce the electrode boundary layer voltage drop, is still a valid concept for electrode protection which should be investigated. The present study has developed the experimental and analytical techniques for investigating "gaseous electrodes" which incorporate continuous plasma sources such as auxiliary burners, R.F. discharges, or microwave discharges. Systems of this nature can provide some form of electrode protection. It is recommended, therefore, that they be investigated.

2.0 ARC GASEOUS ELECTRODE DEVELOPMENT - E. P. Scannell, R. Mallavarpu

The original work[1,2] on the arc gaseous electrode was done in the RMC Electrode Development Facility (EDF), utilizing a 2-Tesla magnet with arc-generation, diagnostic, and support equipment. This facility is shown in Fig. 1.

The basic arc gaseous electrode concept, shown in Fig. 2, consists of a magnetically rotated and translated arc in an argon-nitrogen gas mixture in the annular region formed between a coaxial cylindrical cathode and anode which are incorporated in the MHD channel electrode. Because of the yaw angle with respect to the magnetic field, the arc executes a helical path along the electrode. Small inlet ports entering perpendicular to the cylindrical annulus allow neutral argon, or other inert gas, to flow past the traveling arc. The arc ionizes a part of the gas, which is then allowed to efflux from the MHD generator wall through a slot which is machined parallel to the plane of the window frame. Figure 3 shows the slot in the bottom electrode wall of the electrode frame.

In this approach, it is postulated that the conventional MHD channel solid electrode is replaced by a slot filled with a moving arc plasma. This was believed to have the following major advantages: (a) the plasma was considered to be self-replenishing; (b) the injected plasma should reduce boundary layer voltage drops; (c) the electrode should be able to carry higher current densities; and, (d) because of the controlled rapid arc motion, the electrode should be capable of long-duration continuous operation at higher current density levels with little erosion.

The objectives of Task I of the program were to: (a) conduct parametric studies of the arc gaseous electrode; (b) select an optimum configuration; and, (c) test this concept in a working MHD generator. This section of the report will discuss the parametric studies conducted in the EDF.

Tests in the EDF allowed the following variables to be changed:

(1) Magnetic induction and the angle between the electrode and the magnetic field, i.e., the yaw angle
(2) Arc current
(3) Arc gas composition and mass flow rate
(4) Arc chamber geometry
(5) Arc cathode materials
(6) Coolant flows

The initial studies showed that the yaw angle of the electrode with respect to the applied magnetic field for optimum performance was rather large, much greater than could easily be configured into presently used MHD channel designs. This effect is dependent upon cathode material. Thoriated tungsten cathodes were demonstrated to work reasonably well at the 25° yaw angle which had been built into RMC diagonal conducting wall channel test sections. Copper cathodes did not perform as well at this angle.

Geometrical changes to the annular arc chamber included a larger inert gas plenum to aid in inlet pressure control and improved location of the gas

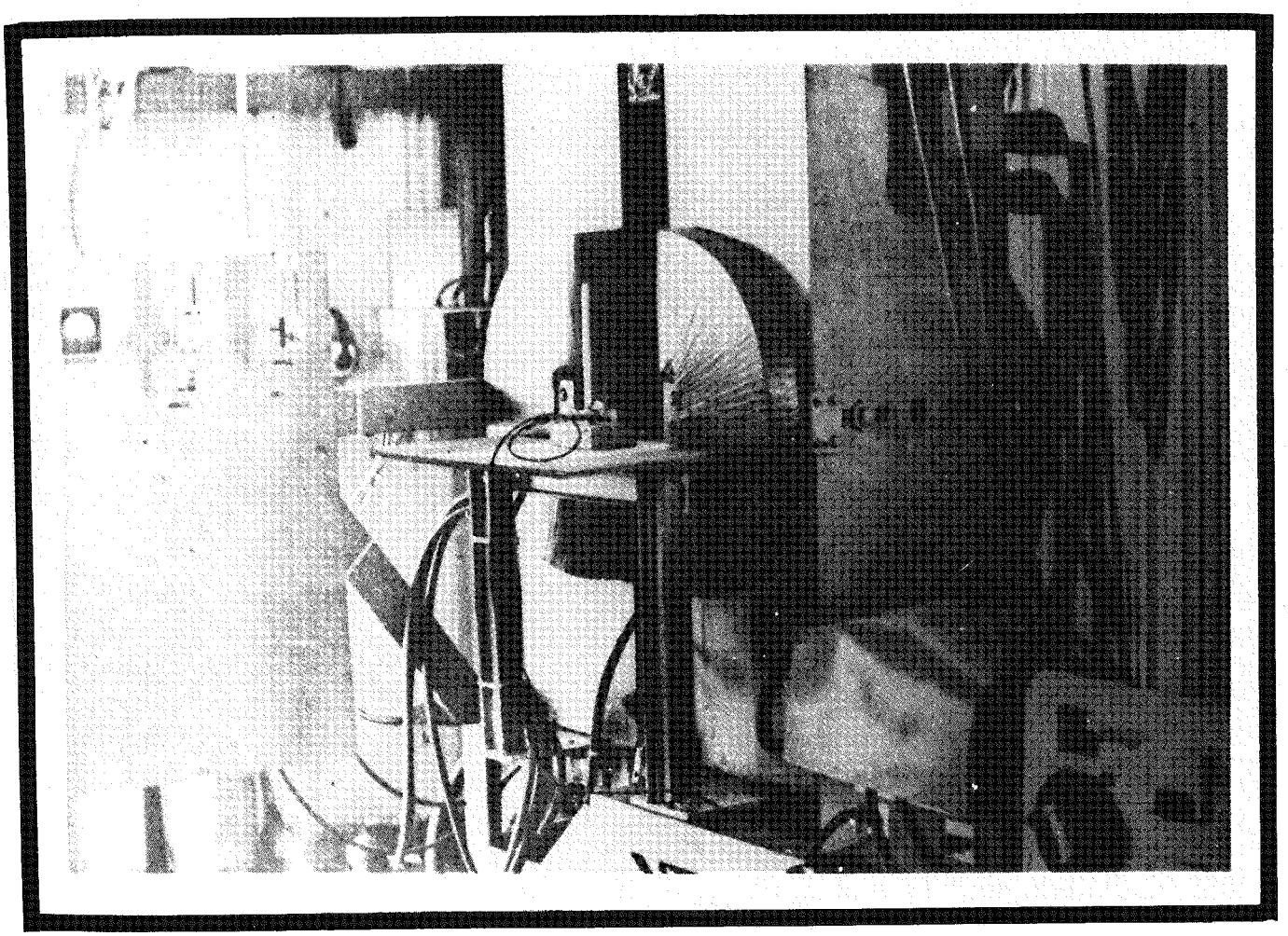

Fig. 1 Electrode Development Facility

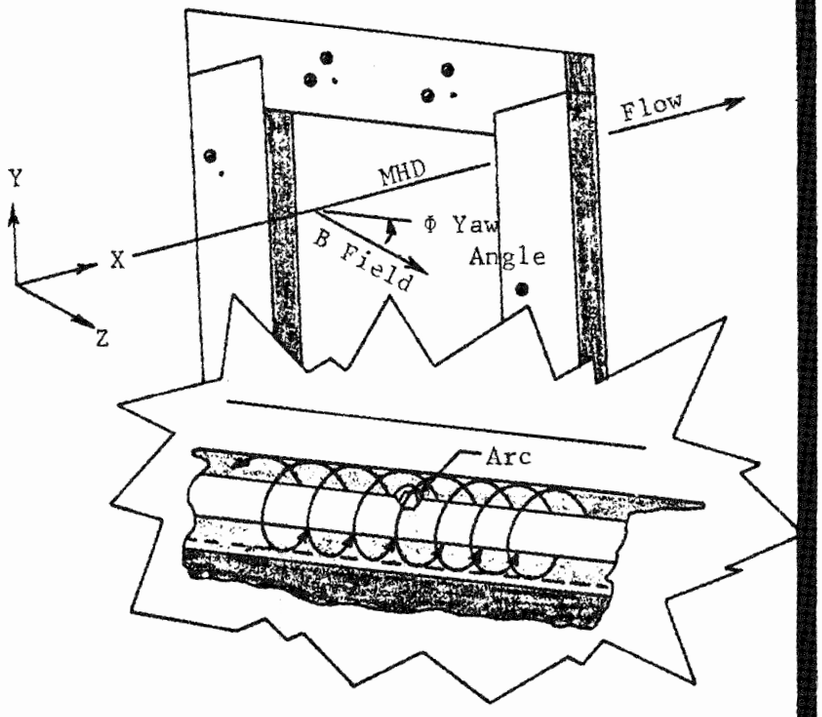

Fig. 2 Artist's Conception of Helical Arc Path in Gaseous Electrode

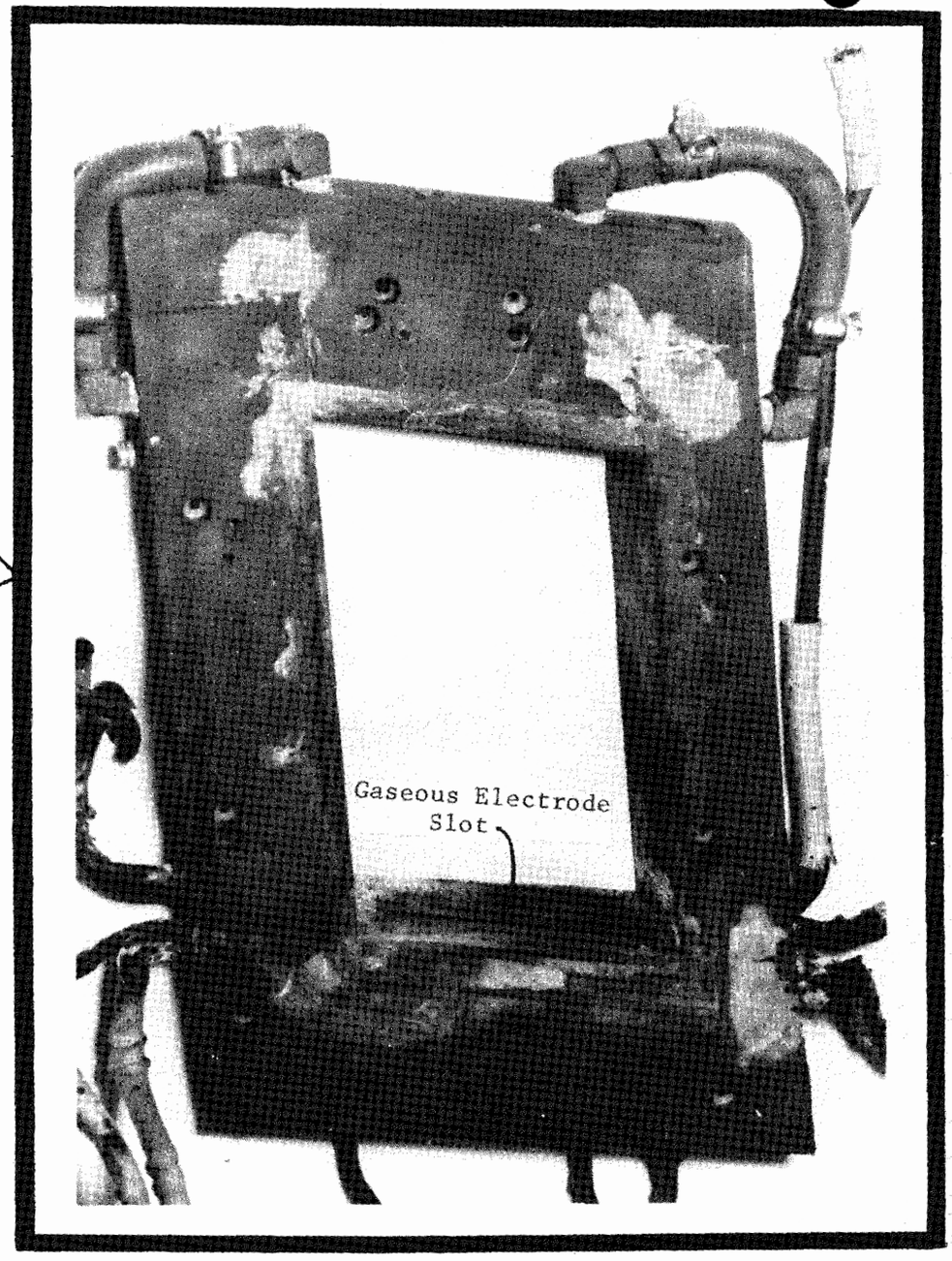

Fig. 3 MHD Channel Window Frame Segment with Gaseous Electrode in Bottom Wall

inlet and plasma exit ports so as to be tangential to the cylindrical annular arc chamber in order to provide better control of the gas/plasma flow relative to arc motion. The geometrical changes also included a larger diameter cathode (1/4") for long duration testing, and ports for several diagnostic measurements such as fiber optics.

The fiber optic systems proved to be very valuable diagnostic tools. The fiber optic bundles were arranged so that they transmitted light from the annular arc whenever it traveled through the fiber optics limited field of view. The light levels were converted to electrical signals with silicon photodiodes. By this means, the motion of the arc past the optical fiber produced a series of electrical pulses. Count rate circuits used as tachometers were then used to measure the annular arc rotational and translational frequencies. This provided a valuable tool for evaluating the operation of the annular arc.

The materials testing program evaluated several cathode materials. First, the 1/8" diameter arc cathodes with various wall thicknesses and different grades of copper were tested. This was followed by tests of a stainless steel cathode to determine water cooling and materials effects. These tests obtained data on cathode erosion and arc rotational speeds as a function of magnetic field for thick and thin walled Oxygen Free High Conductivity (OFHC) copper and slightly-magnetic stainless steels. These tests established a general curve of arc rotational frequency versus magnetic field wherein the frequency is fairly high at low fields, goes through a minimum, and then increases at a rate somewhat faster than linear for higher fields. As expected, the steel cathodes showed the whole arc frequency curve increased by a factor of 6 or higher than the copper cathodes, although the former still show higher erosion rates. It is expected that more magnetic steels would show even higher frequencies, due to the concentration of field lines on the arc cathode spot, and possibly this might be enough to reduce the erosion down to copper levels.

Several materials and geometry variations were then tested. Tests with both 1/8" and 1/4" o.d. OFHC arc cathodes of varying wall thickness were evaluated. A great improvement in plasma efflux from the electrode slot was observed when the arc was rotating in the same direction as the tangentially injected argon gas flow. By reversing the magnetic field direction, the annular arc can be made to rotate in a direction opposite to the flow. As expected, the efflux is considerably reduced. The larger diameter cathode was found to run cooler, but the cooling water flow was found to have a substantial effect on the arc rotational and translational velocities.

A number of potential arc cathode materials were screened and the test results narrowed the field to four arc cathode materials: OFHC copper, brass, thoriated tungsten, and molybdenum. Each of these materials have both good and bad characteristics. For example, brass was found to give the largest plasma efflux and operated well at the yaw angle of 25° which was built into the MHD generator test section. However, the brass cathode operated poorly at fields greater than 1.8 Tesla. Molybdenum operated somewhat erratically at all yaw angles, but its performance improved considerably at higher magnetic fields. Copper operated well at high yaw angles and high magnetic fields. Thoriated tungsten was selected as the best compromise arc cathode material because it would run reasonably well at a 25° yaw angle, and would also operate at high magnetic fields. Therefore, thoriated tungsten arc cathode with 1/4" o.d. was selected for testing in the GTF MHD generator at a 25° yaw angle.

Among the geometrical variations tried was a modification of the arc anode structure to provide space at the ends for arc extinguishment. After several attempts, an internal diameter increase in the end regions was found to be quite effective in extinguishing the arc when it reaches the slot end. With this geometric modification, it was no longer necessary to introduce an end extinguishing gas such as N_2 or SF_6. It had also been observed that anything more than a very small flow of SF_6 (> 3 SCFH) would totally extinguish the arc. Even at these small flows, the SF_6 was dissociating and the resulting products attacked the insulators. With this interior configuration, it was possible to inject small quantities of nitrogen into the end ports to purge the ends of the fiber optic cables, or to inject even greater quantities of argon with substantial angular momentum which could be used to force the arc to rotate in the central part of the cathode.

The results of this phase of the investigation were the design and construction of an electrode frame which incorporated the 1/4" cathode and the fiber-optic diagnostic capabilities. The results obtained in testing these concepts in an MHD generator are presented in Section 5.2.

One of the diagnostic techniques developed for evaluating the bench scale electrode development tests was a combination Langmuir/enthalpy/sampling probe. Appendix A describes a typical experiment where this probe was used, discusses the probe operating theory, and gives tentative results of the experiment. By the time that the probe system had been delivered, and the original probe tip which leaked had been replaced, the bench scale testing was substantially completed and attention was being addressed to testing in the Generator Test Facility. Therefore, the probe system was not utilized to its fullest capabilities.

Appendix B is a theoretical examination of plasma momentum and energy transport in the annular cavity of the arc gaseous electrode. A model was assumed and a method was developed to arrive at the dimensions of the arc, the temperature profile in the annulus as a function of space and time, and the velocity and temperature profiles of the gas entering the MHD channel from the electrode. These studies were conducted to provide a theoretical estimate of gas conditions in support of the enthalpy probe measurement.

3.0 MHD GENERATOR CHARACTERIZATION - M. S. Jones, Jr., K. Sathyanarayana, A. J. Armstrong

3.1 MHD Generator Test Facility

Tests of the arc gaseous electrode were carried out in the RMC MHD Generator Test Facility. During the early months of the program, the facility was partially destroyed by the explosion of a liquid oxygen tank. Approximately 18 months were required to bring the facility back to operational status.

3.1.1 Facility Description

The MHD GTF (Fig. 4), which has previously been described,[2] incorporates a continuous-duty, water-cooled, saddle coil magnet with an aperture of 0.254 m x 0.356 m x 1.42 m, capable of producing 4.3 Tesla when provided a power input of 5.5 MW; a water-cooled, 130-segment, diagonal-wall channel with a removable 23-segment center section for testing gaseous electrodes; a 7 MW_t clean-fuel combustor; together with the necessary fuel, oxidizer, seed, ash injection, water cooling, and data recording support systems.

Figure 5 shows the magnet and diagonal conducting wall channel. Figure 6 shows the channel and combustor assembled and placed in the bore of the magnet.

Figure 7 is a schematic diagram of the combustor. Figure 8 gives the internal dimensions of the nozzle and the MHD channel. The channel has a fixed width of 0.09 m and varies in height from 0.09 m at the entrance to 0.171 m at the exit, a half angle divergence of about 2.5° on the electrode walls. Figure 9 shows the magnetic field distribution for an input current of 10,000 amperes. The channel diagonal conducting frame angle is 37°. Figure 10 gives the dimensions of the diffuser which retains a constant height but diverges in width. After the gases exit the diffuser, they pass through a water quench system which reduces the electrical conductivity to avoid shorting out the high voltage end of the MHD generator, which is operated in a two-terminal configuration with the combustor grounded.

The facility can use either diesel oil or propane as fuels. Separate cryogenic storage tanks and feed systems for oxygen and nitrogen are provided so that the combustor oxygen-to-nitrogen ratio can be accurately controlled.

3.1.2 Facility Checkout

Following the rebuilding of the Generator Test Facility, a number of problems were experienced in getting the facility operational. Several of these problems and their solutions will be discussed with the hope that they can be of help to others who operate MHD test facilities.

3.1.2.1 Magnet Problems

The first problem was that some magnet high temperature warning lights always came on during operation at high magnetic fields. The magnet had

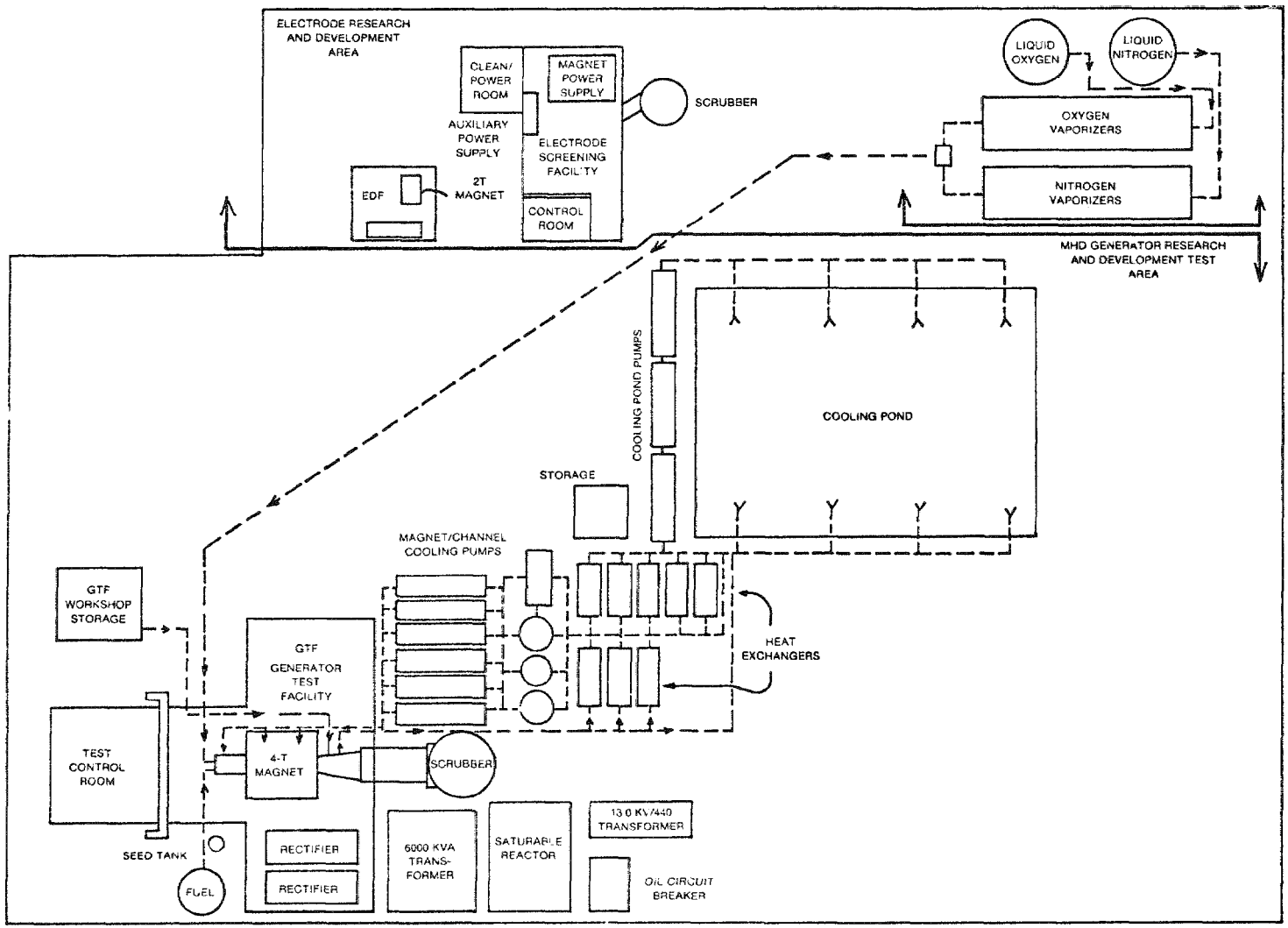

Fig. 4 Layout of RMC MHD Facilities

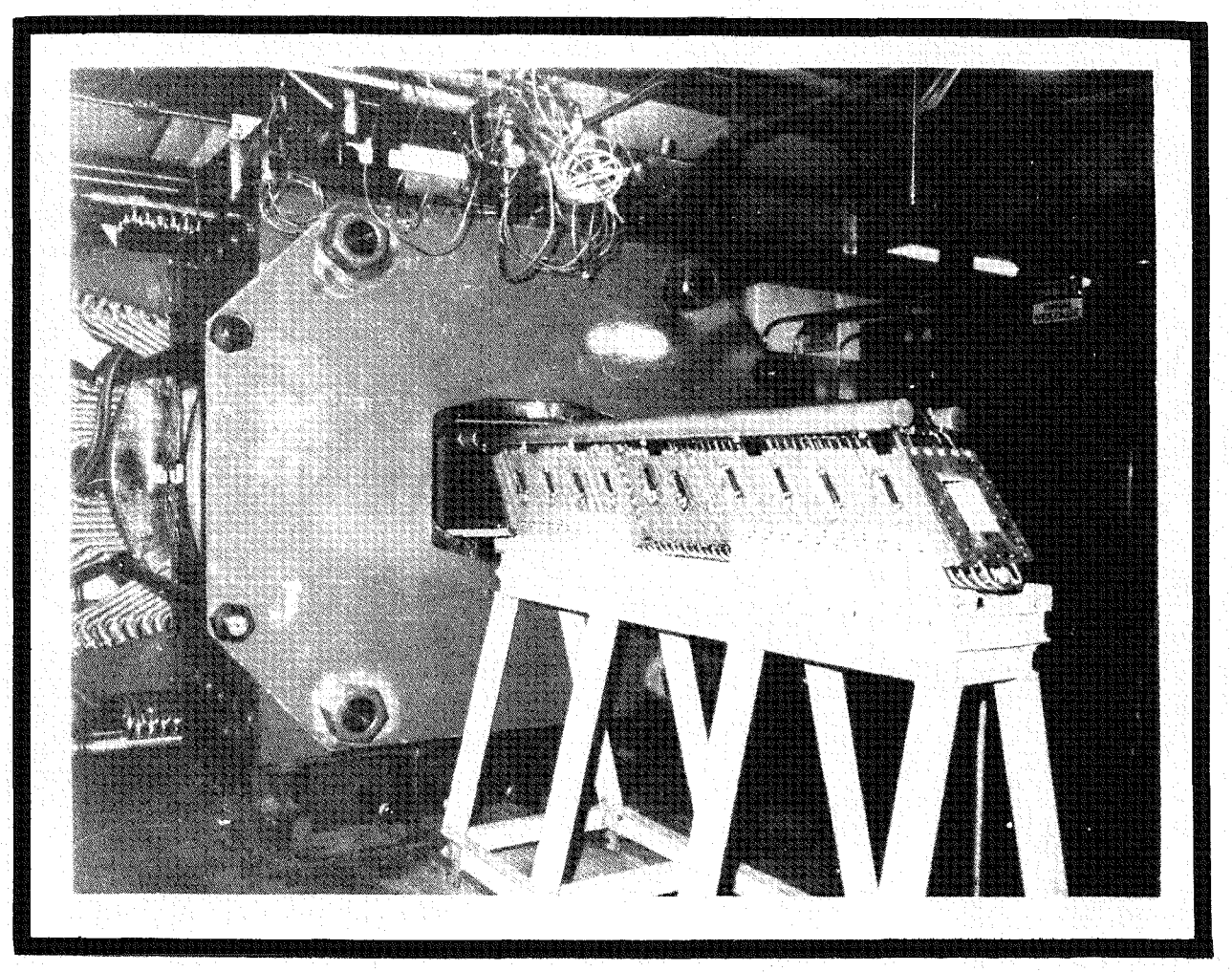

Fig. 5 Diagonal Conducting Wall Generator at Entrance to Magnet

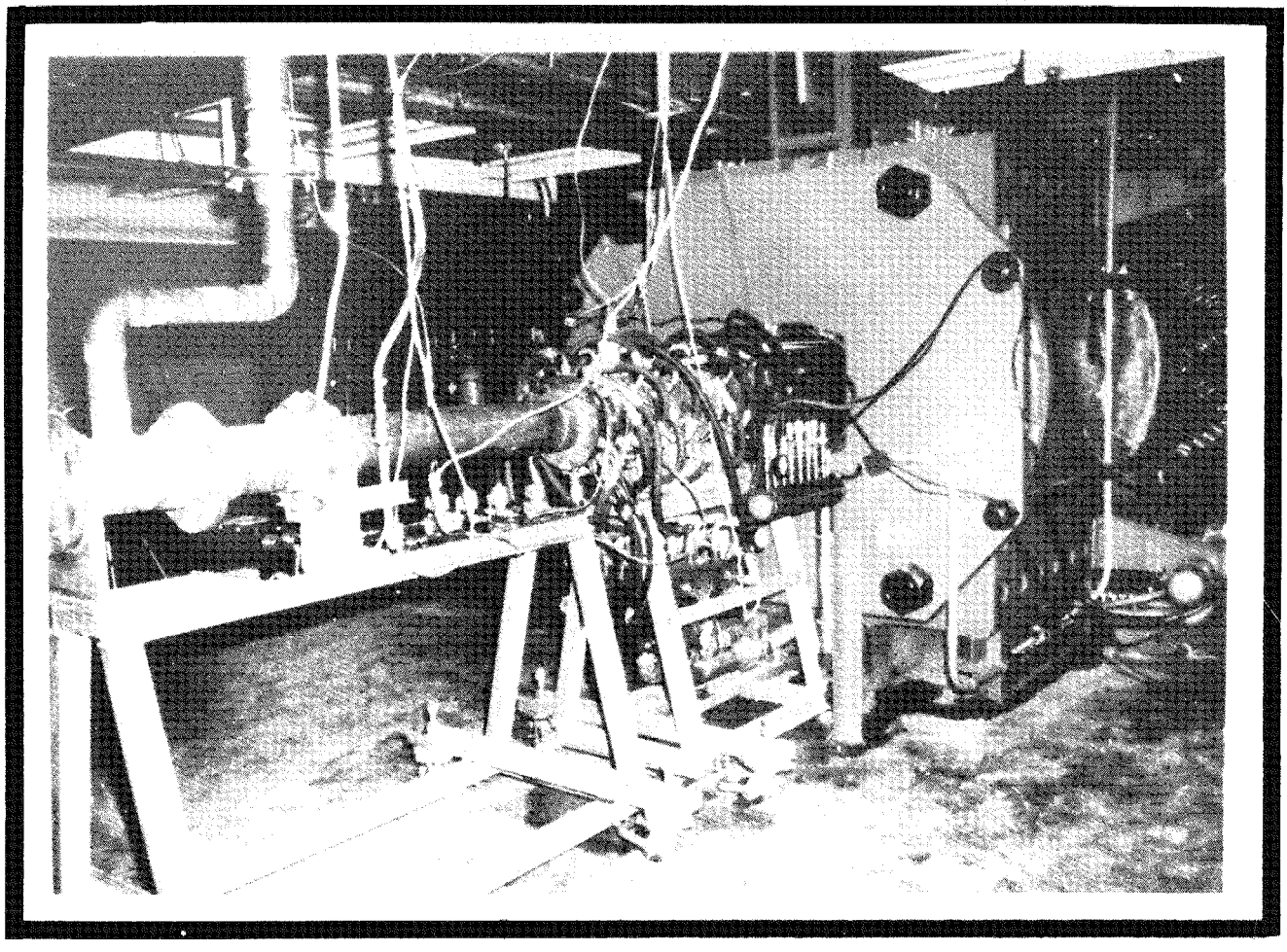

Fig. 6 Combustor Attached to MHD Channel which is Installed in the Magnet Bore

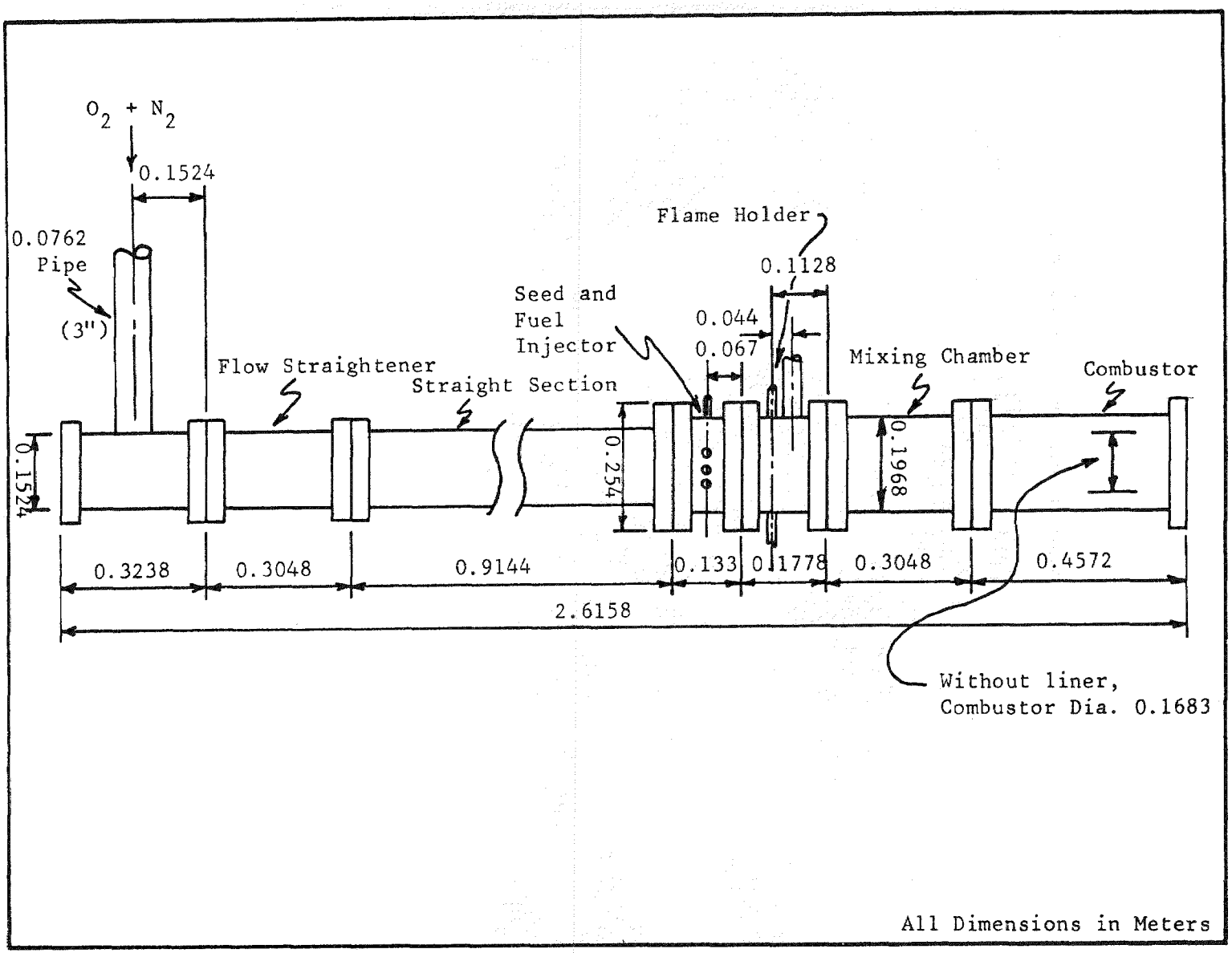

Fig. 7 Schematic Diagram of the Combustor

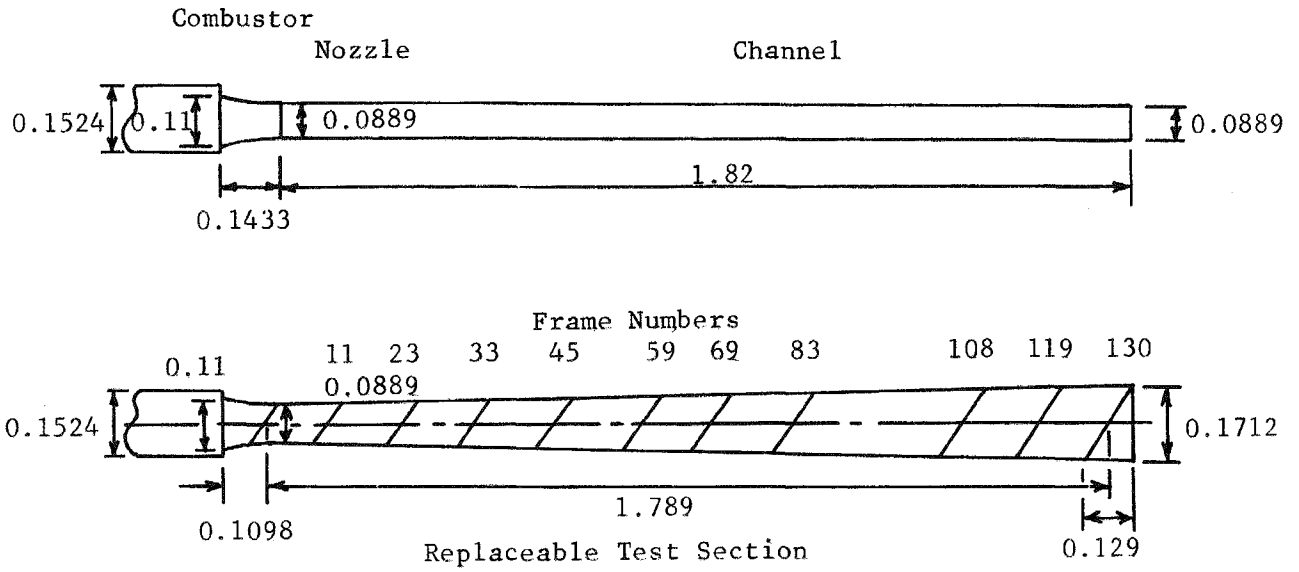

Fig. 8 Schematic of the Nozzle and Channel
(All Dimensions are in Meters)

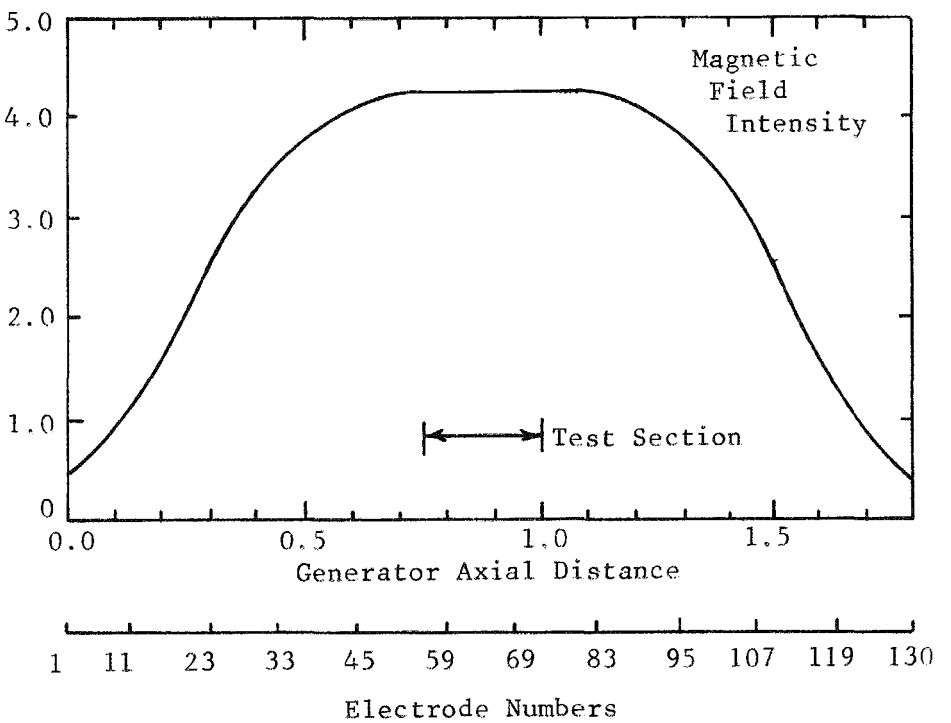

Fig. 9 Magnetic Field as a Function of Axial Distance
for a Current of 9600 Amperes

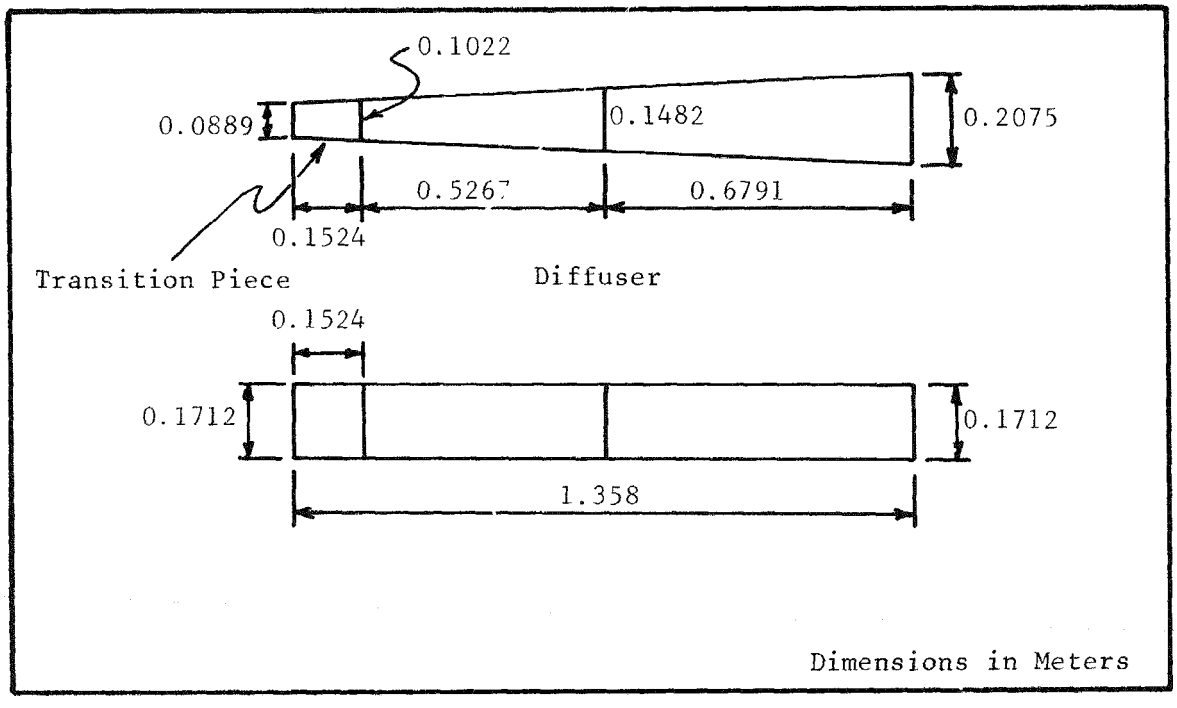

Fig. 10 Schematic Diagram of the Diffuser and Transition Piece

previously been successfully operated at these levels during early 1976. After several months had been spent on installing larger size hoses to the magnet, chemically and mechanically cleaning the magnet flow passage and the magnet system heat exchangers, etc., it was determined that when the magnet was reconditioned following the explosion, the magnet manufacturer had supplied the wrong thermal switches.

3.1.2.2 Combustor Problems

During this period, it was also determined that the combustion system was not performing properly. The first clue came in an analysis of the axial voltage measured along the channel during open circuit which is shown in Fig. 11. The upper curve in Fig. 11 is the theoretical distribution of the generator axial voltage for the condition of B = 4 Tesla, a mass flow of 1.1 kg/sec, and a current of 93 amperes to the external load. The lower curve presents the measured experimental axial voltage profile for open circuit conditions with a magnetic field of 3.5 Tesla and mass flow of 0.89 kg/sec. It is seen that the experimental voltages are an order of magnitude below the predicted values, and that the voltage in the generator goes negative in the front part of the channel, in contradiction to the theoretical prediction. During these runs, it was also noticed that the high temperature paint on the large diameter pipe which goes from the quench ring at the exit of the diffuser to the scrubber was burning off. In one test, the paint on the cyclone which is in front of the scrubber showed heat damage. During another test, the pipe between the diffuser and the scrubber got so hot that it set fire to the cellulose insulation which had been applied to the inside of the walls of the generator test building to reduce the environmental heating and cooling loads. From these observations, it became obvious that combustion was not complete in the combustor, but was also occurring in the channel, in the diffuser, in the pipe between the diffuser and cyclone, and, in some cases, in the cyclone at the entrance to the scrubber. Therefore, it was concluded that the combustor did not provide adequate volume for the complete combustion of the mixture and for the potassium seed ionization. Hence, there was very low electrical conductivity in the plasma flowing through the front part of the generator. This could have been the major reason for the negative voltages in the front part of the channel shown in Fig. 11.

To analyze the magnitude of the problem, gas samples were drawn from three stations starting at the exit of the combustor, at the exit to the channel, and in the pipe between the quench ring and the scrubber. A water-cooled gas sampling probe was fabricated and used to obtain the gas samples at the exit to the combustor, while at the other stations the samples were drawn from the sidewalls. Figure 12 shows typical gas composition data from a run where diesel fuel with stoichiometric amounts of oxygen was burned. The mass flow was 0.83 kg/sec and O_2/N_2 ratio was unity. The concentration of the various non-condensible gases, i.e., O_2, N_2, CO, CO_2, etc., was determined by gas chromatographic analysis, and is shown as a function of distance along the combustion product flow path. It is seen that at the exit to the combustor, free O_2 is present and the levels of CO and CO_2 are low. As the mixture flows along the channel, the O_2 level falls while the CO_2 level increases. The CO level is low and constant. These data confirm the fact that the combustion was incomplete at the exit of the combustor and that the mixture continued to burn as it flowed through the channel and the remainder

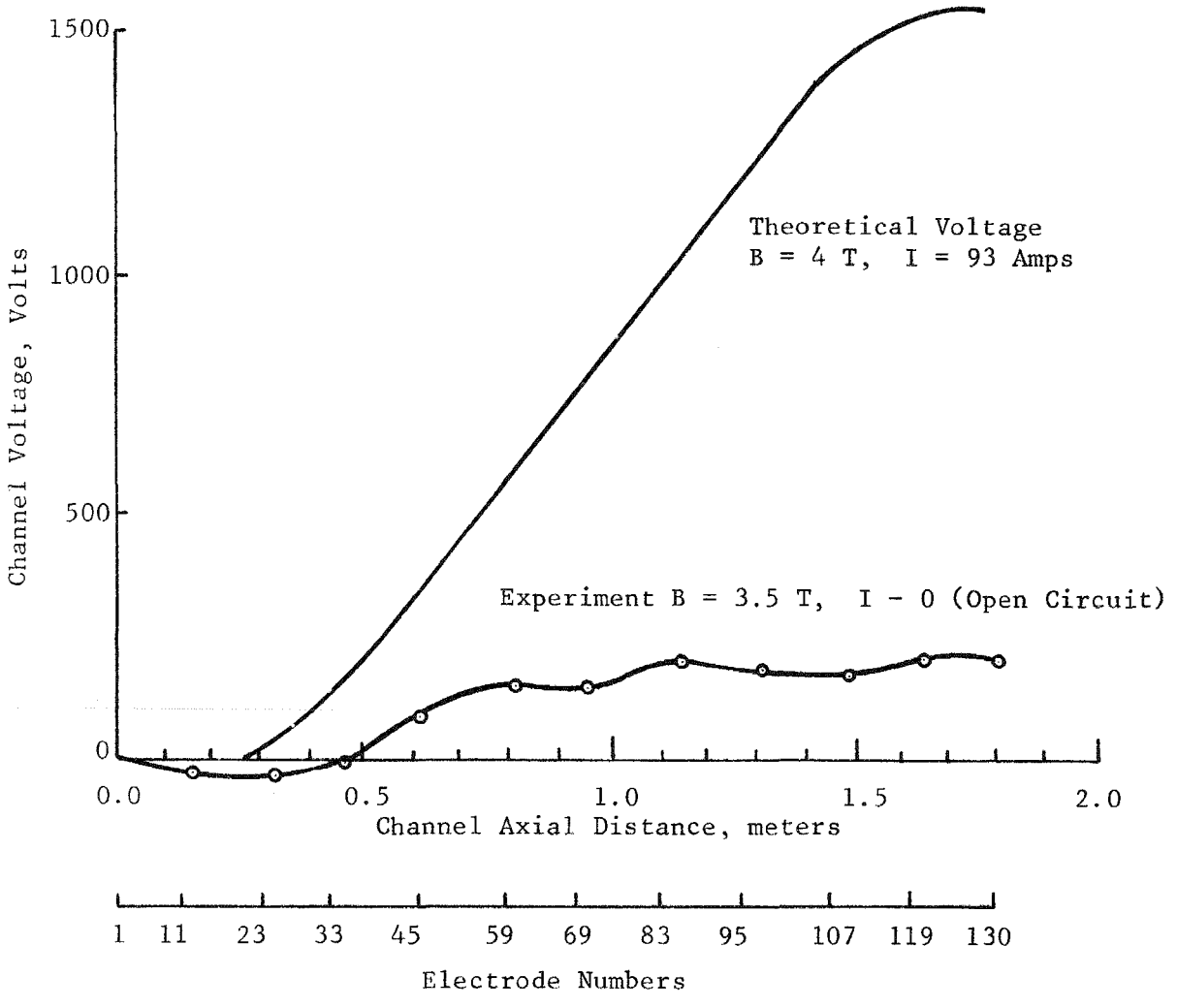

Fig. 11 Comparison of Channel Axial Voltage Distribution

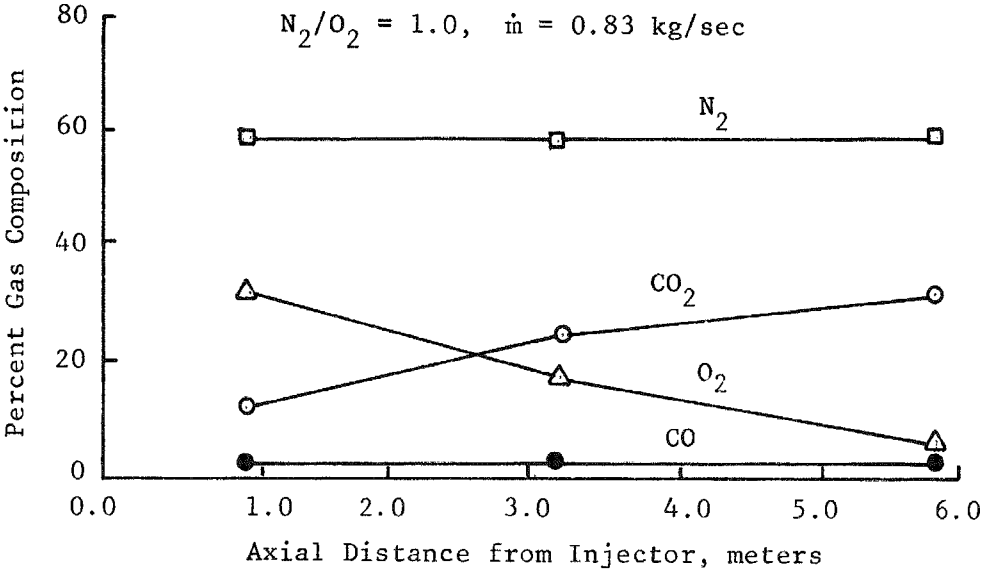

Fig. 12 Variation of Gas Composition Along the Flow

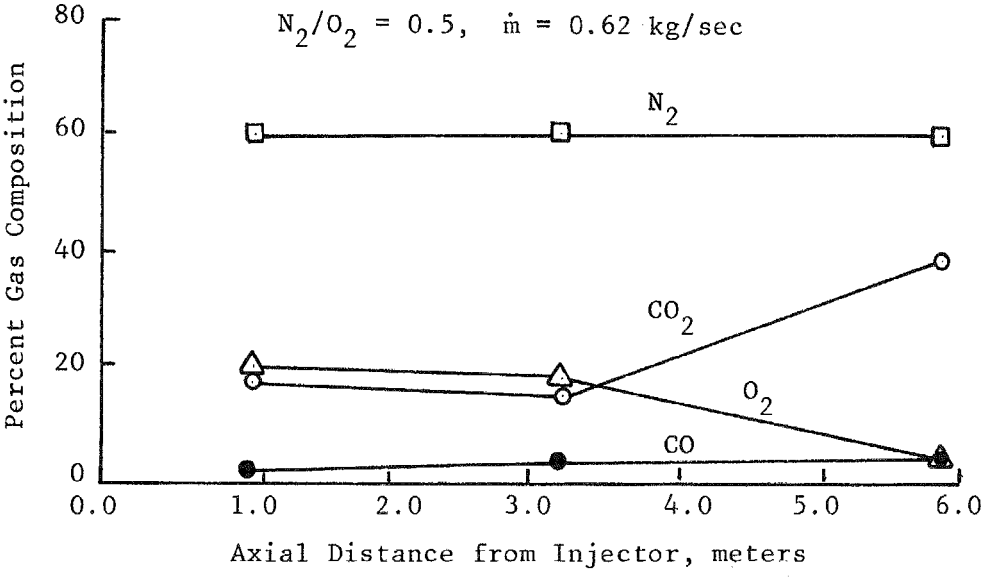

Fig. 13 Variation of Gas Composition Along the Flow

of the flow stream. Figure 13 shows the same type of gas analysis results from a test where the fuel and oxygen flows were maintained at the same levels shown in Fig. 12, but the nitrogen flow was reduced by one-half so that the mass flow was only 0.62 kg/sec. It is seen that the CO_2 level at the exit of the combustor has practically doubled, indicating more combustion in the combustion chamber.

Figure 14 is a plot which presents data from a number of runs. Here the residual oxygen concentration at the exit of the combustor is plotted as a function of the combustor mass flow rate. The data points numbers refer to equal steps in the fuel mass flow rate where Step 16 is taken to be at the combustor design flow. It is seen that when the mass flow is greater than about 0.15 kg/sec, there is unreacted oxygen present at the exit of the combustor. This strongly implies that the combustor volume is inadequate by about a factor of 6 or 7 for the designed flow of 1.1 kg/sec at a nitrogen-to-oxidizer (N_2/O_2) ratio of unity. The residence time, τ, of the gases in the combustor can be estimated from the relation:

$$\tau = \text{volume/volume flow rate} = \left(\frac{P_{cc}}{R\,T_{cc}}\right) \cdot \frac{V_{cc}}{\dot{m}}$$

where, P_{cc} is the combustion chamber absolute pressure, R is the gas constant (equal to 28 for the combustion products), T_{cc} is the combustion chamber temperature, V_{cc} is the combustion chamber volume, and $\dot{m}$ is the mass flow. For the design condition of these experiments, i.e., $T_{cc} = 2900^{\circ}K$, $P_{cc} = 2.2286 \times 10^4$ kg/m^2, $V_{cc} = 0.063$ m^3, and a mass flow, $\dot{m}$, of 1.1 kg/sec, the residence time would be only 4.1 msec. Normally, 20 to 24 msec residence time[3] is required for this type of combustor.

Because the dynamics of burning a liquid fuel are determined by the rate of evaporation of the fuel at the particle surface, it was decided to substitute propane, which has a boiling point of $-42.17^{\circ}C$, for diesel fuel, which has a boiling point of over $600^{\circ}C$, as one method of speeding up this critical process in the combustion of the fuel. It was found that by using propane, and by reducing the N_2/O_2 ratio so that the total mass flow was reduced for a given amount of heat release, thereby increasing the combustor gas residence time, a more complete combustion could be achieved in the combustor. Among the factors involved in switching to propane was the fact that because of its low density, 0.59, compared to diesel fuel, 0.819, it was necessary to have higher volume fuel flow rate through the spray nozzles, which required higher pressures in order to obtain the same heat release in the combustor. The higher pressure drop in the spray nozzle results in smaller sized droplets which have more surface area and burn faster.

To measure the conductivity of the plasma under these conditions, the voltage of an external power supply was applied between Electrodes 1 and 5 and Electrodes 125 and 129 of the DCW channel without a magnetic field. The split plate frames, which like all other electrodes are isolated from each other, were connected to high-impedance voltmeters as shown in Fig. 15 and used as floating potential probes. The potential distribution measured, as shown in Fig. 16, is nearly linear over the middle portion of the channel.

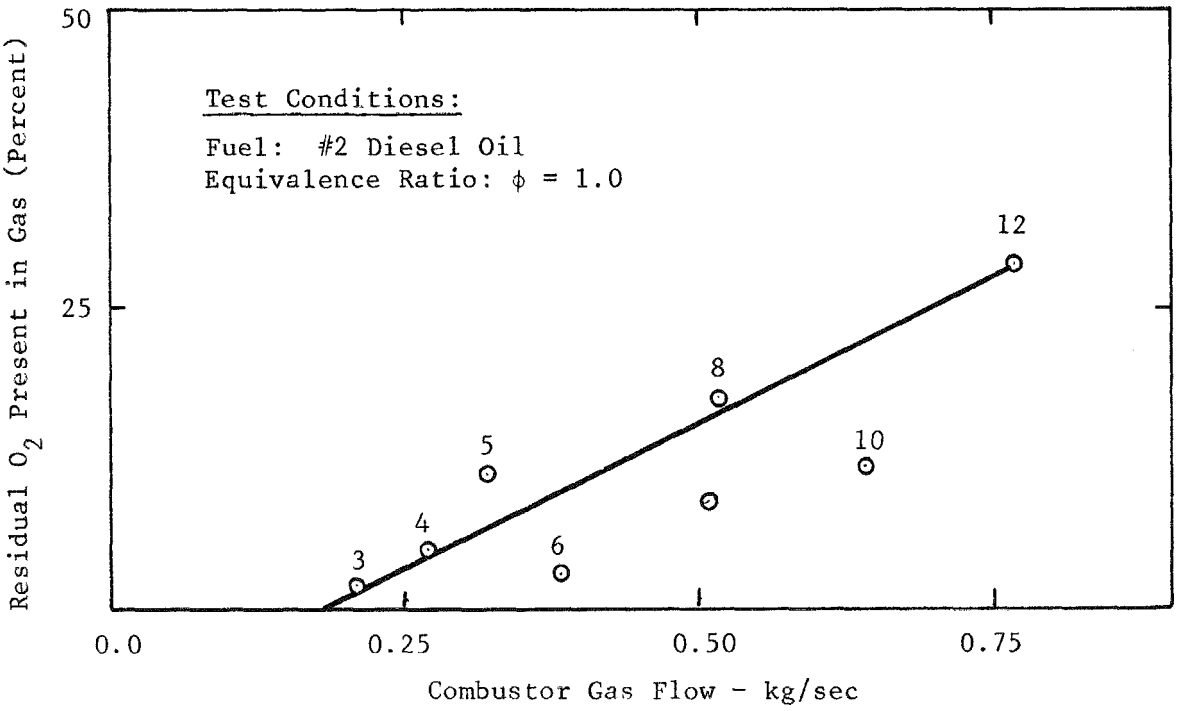

Fig. 14 Variation of Residual Oxygen at Combustor Exit with Gas Flow Rate

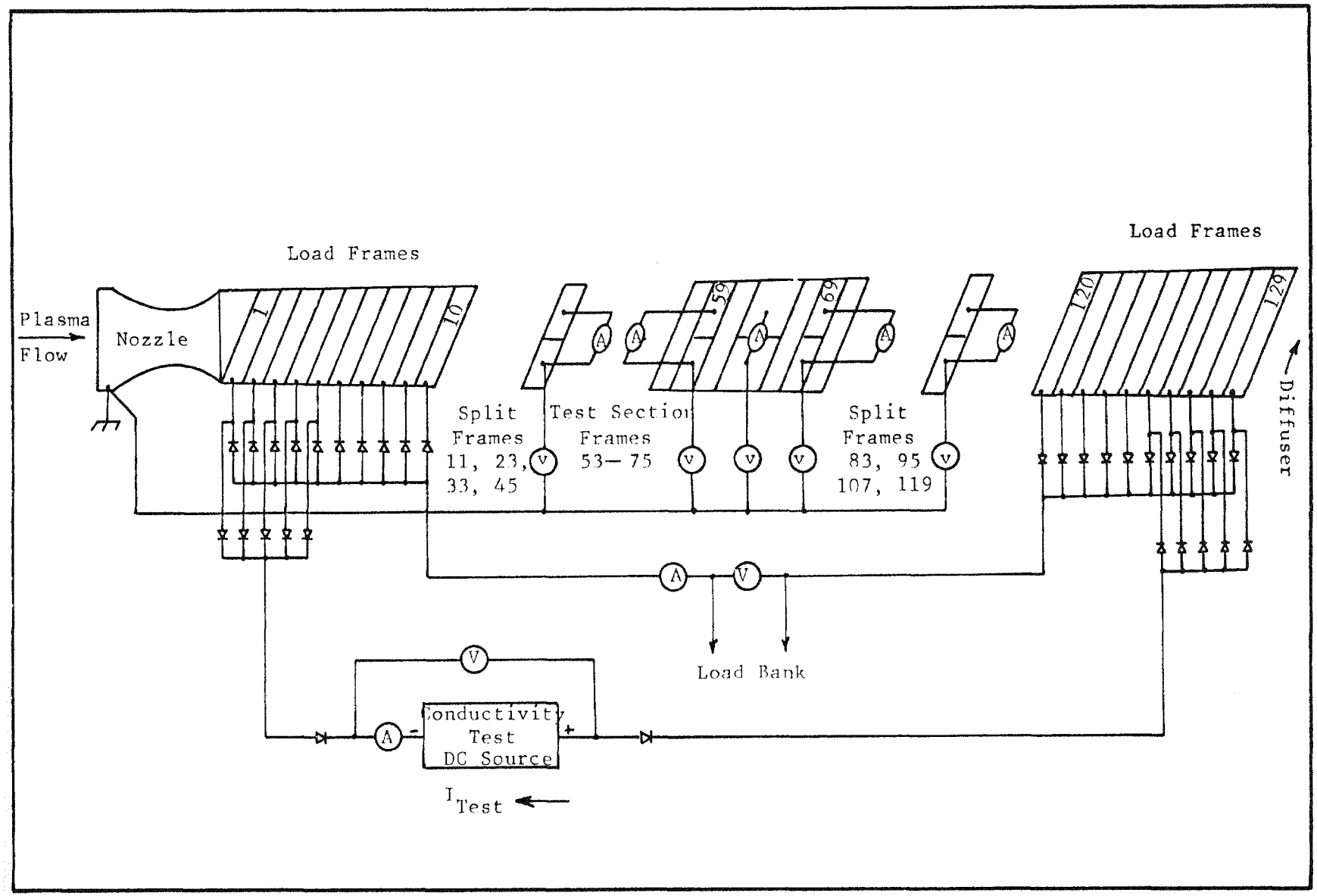

Fig. 15 MHD Channel Test Setup for Conductivity Measurements

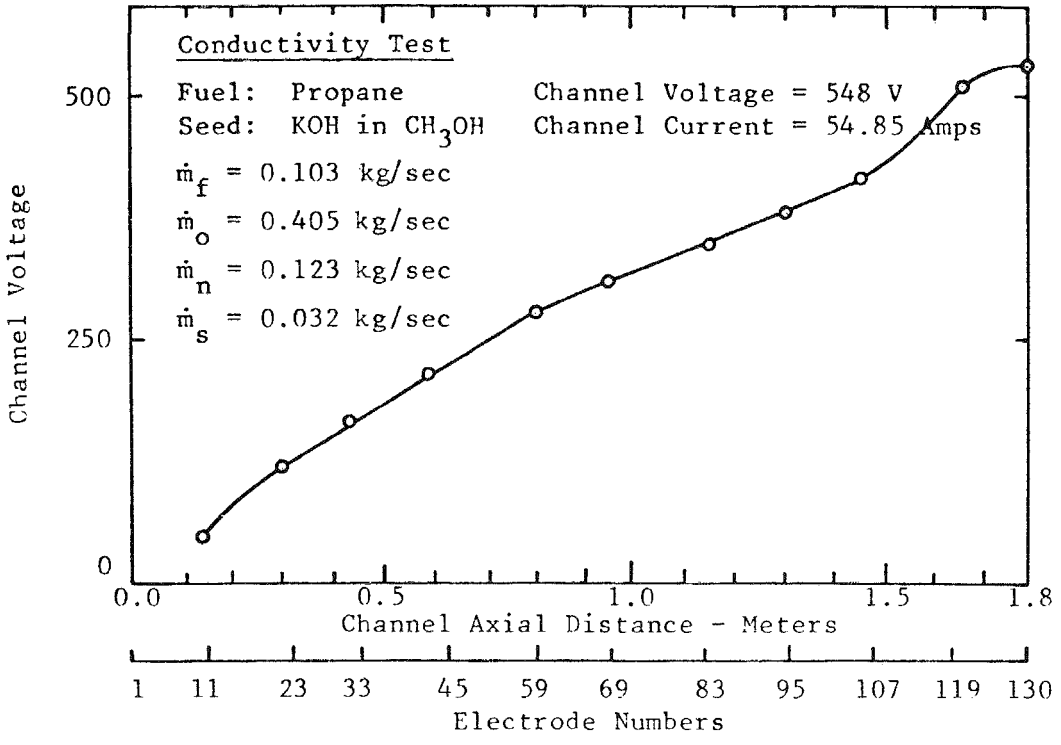

Fig. 16 Voltage Profile for Conductivity Test

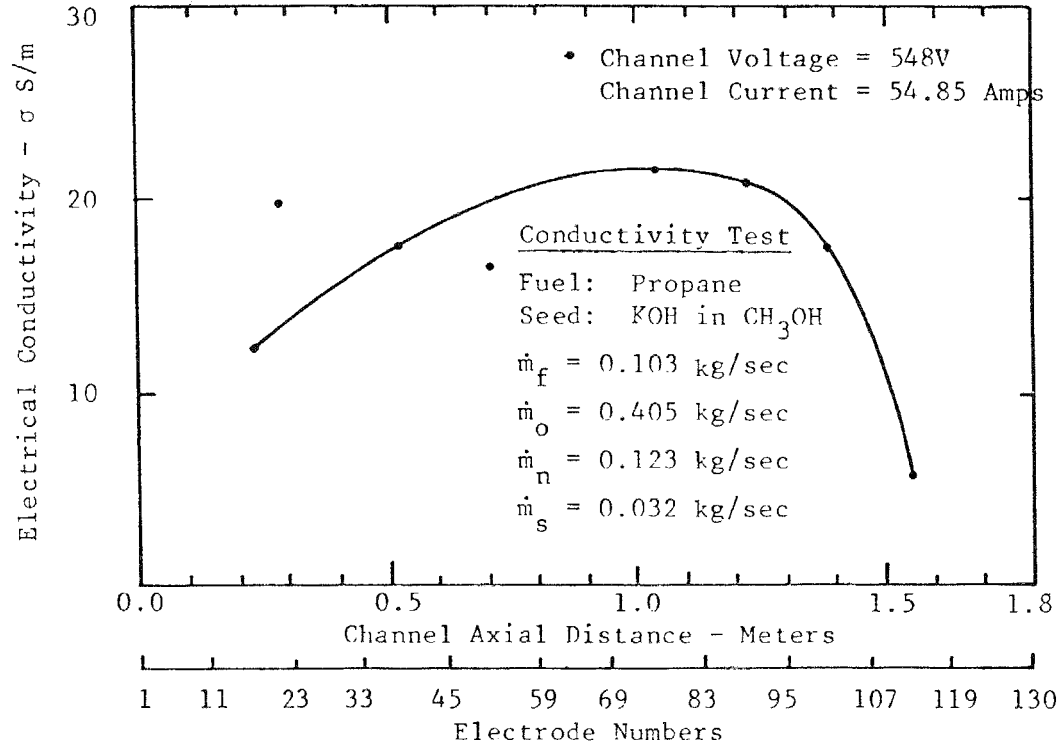

Fig. 17 Conductivity Profile Along the Channel

Conductivity calculations were based on the differences in potential, V, between adjacent split frame electrodes, spaced at a dixtance X apart, where the potential distribution was linear. With the measured total current, I, the potential field along the channel, E ($E \equiv \Delta V/\Delta X$), and the mean current flow area A(X) between X and X + ΔX, the conductivity of the plasma can be determined from Ohm's law by the relation:

$$\sigma\ (X) = \frac{j(X)}{E(X)} = \frac{I\ \Delta X(X)}{\Delta V(X)\ A(X)}$$

The variation of the conductivities calculated by this method is shown in Fig. 17 as a function of distance along the channel. It is seen that the conductivities are about 10 to 14 S/m at the front end of the channel increasing to about 22 S/m at the middle part of the channel. For these measurements, the N_2/O_2 ratio was 0.30, the fuel was propane, and the total mass flow rate was 0.66 kg/sec. The seed was potassium hydroxide dissolved in methanol. Since the chromatographic analysis of the gas suggests that combustion must have been substantially complete, it may be concluded that the dynamics of seed ionization are now controlling the plasma conductivity.

One interesting sidelight to these experiments was that as the combustion process was made more complete in the combustor, the heat released to the combustor walls increased so that the temperature rise of the combustor cooling water served as a calorimetric measure of the combustor system.

When flowing propane, it was found that the positive displacement gear pump used for diesel fuel would not pump the low viscosity propane. Therefore, in the initial tests with propane the fuel was fed by pressurizing the propane tank to its rated pressure of 14.6 Atm (200 psig) with nitrogen. As cited above, the use of propane required a higher volumetric flow than was required with diesel fuel so that the early propane experiments were limited in thermal input to combustor to about 60% of the design value. A special turbine pump for propane was subsequently installed which allowed operation at nozzle pressures of up to 23.1 Atm (325 psig).

The essential result of these combustor studies was that under certain conditions it is possible to produce a plasma which has reasonable conductivity in the region of the arc gaseous electrode test section, and that the portion of the generator downstream from the gaseous electrode test section would act like an operating MHD channel so that any changes to the flow which were the result of the operation of the arc gaseous electrode could potentially be observed as changes to the generator output characteristics. While these were not the best conditions, i.e., the MHD generator was still not producing its design output, it did provide the MHD channel flow conditions to evaluate the effect of using the arc gaseous electrode.

3.2 MHD Channel Characterization

In order to evaluate what effect the arc gaseous electrode has on the performance of the MHD channel, it was important to establish a performance baseline which determined how well the MHD generator was working, and how its performance agreed with theoretical predictions. For this purpose, some channel characterization runs were made. The key variable observed was the channel static pressure profile.

Figure 18 shows the static pressure distribution along the channel for various mass flow rates. The channel was designed for subsonic operation with a magnetic induction of 4 Tesla and a plasma conductivity of about 10 S/m. For the experiment where there is no seed and no field, a shock structure appears to exist in the channel when the mass flow was increased beyond 0.6 kg/sec. It is seen that the shock structure moves downstream as the mass flow is increased. For the design flow rate of 1.1 kg/sec, the shock structure appears to be in the vicinity of the channel exit.

The pressure data shown in Fig. 19 corresponds to two representative runs with a mass flow of 0.67 kg/sec, or at 60% of design flow. It can be seen that the static pressure all along the channel increased due to the J x B interaction when the magnetic field was applied. Further, the burner chamber pressure, which is approximately equal to the channel stagnation pressure, also increased as the magnetic field was increased. The increase in burner chamber pressure was about 9%. The static pressure distribution at higher field and mass flow is shown in Fig. 20. The effect of adding seed to the flow is also indicated in the figure. With the addition of seed material, the static pressure all along the channel increases slightly and there is slight upstream movement of the shock position due to the increased interaction. When the magnetic field is applied, the pressure field increases. It is seen that short circuiting the generator moves the shock upstream, due to the increased interaction effect. It is concluded, therefore, that there is not enough MHD interaction in the high L/D channel under present conditions to force the shock wave upstream to the nozzle throat so that subsonic flow can be obtained at the design mass flow.

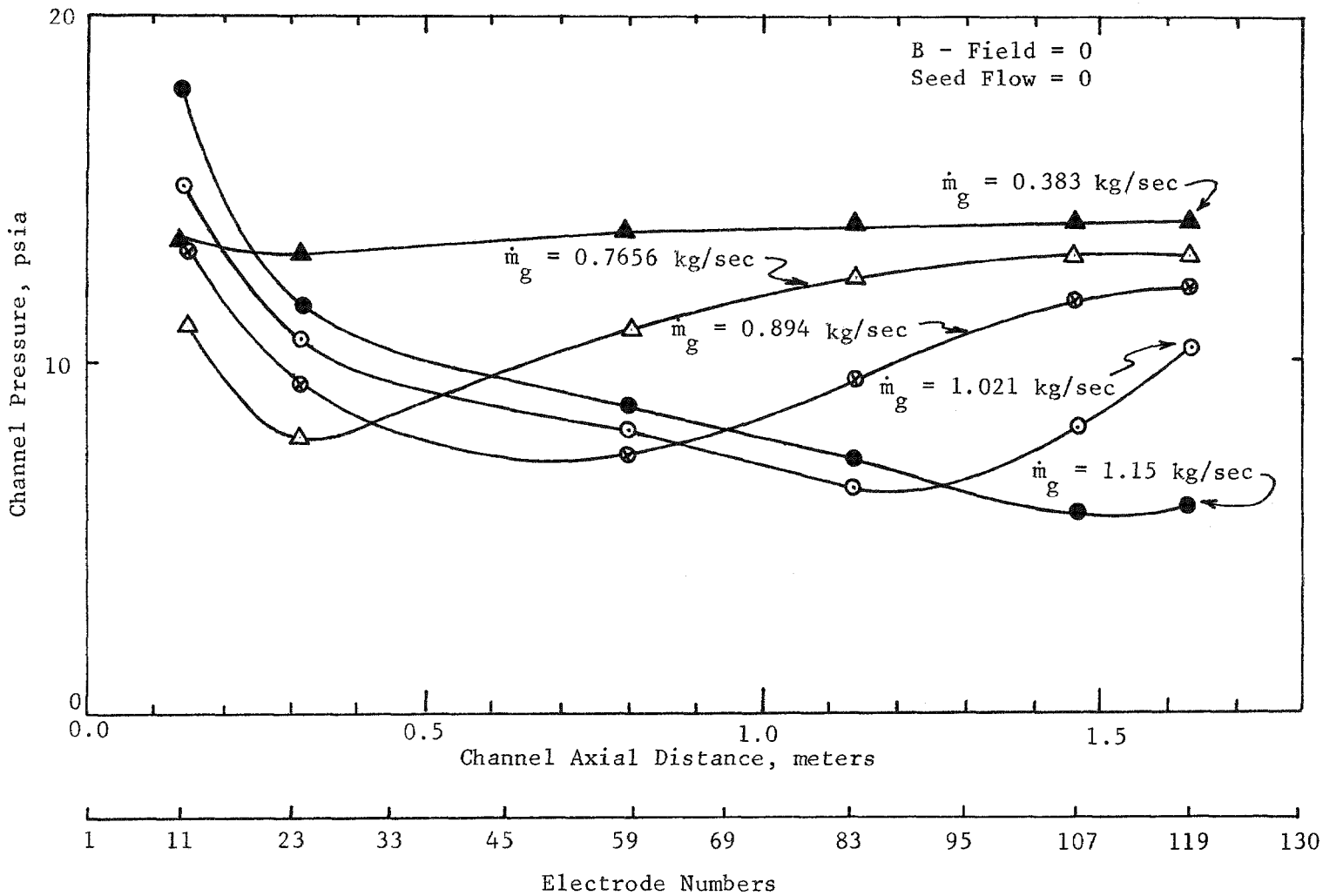

Fig. 18 Pressure Distribution in the Channel for Different Mass Flow Rates

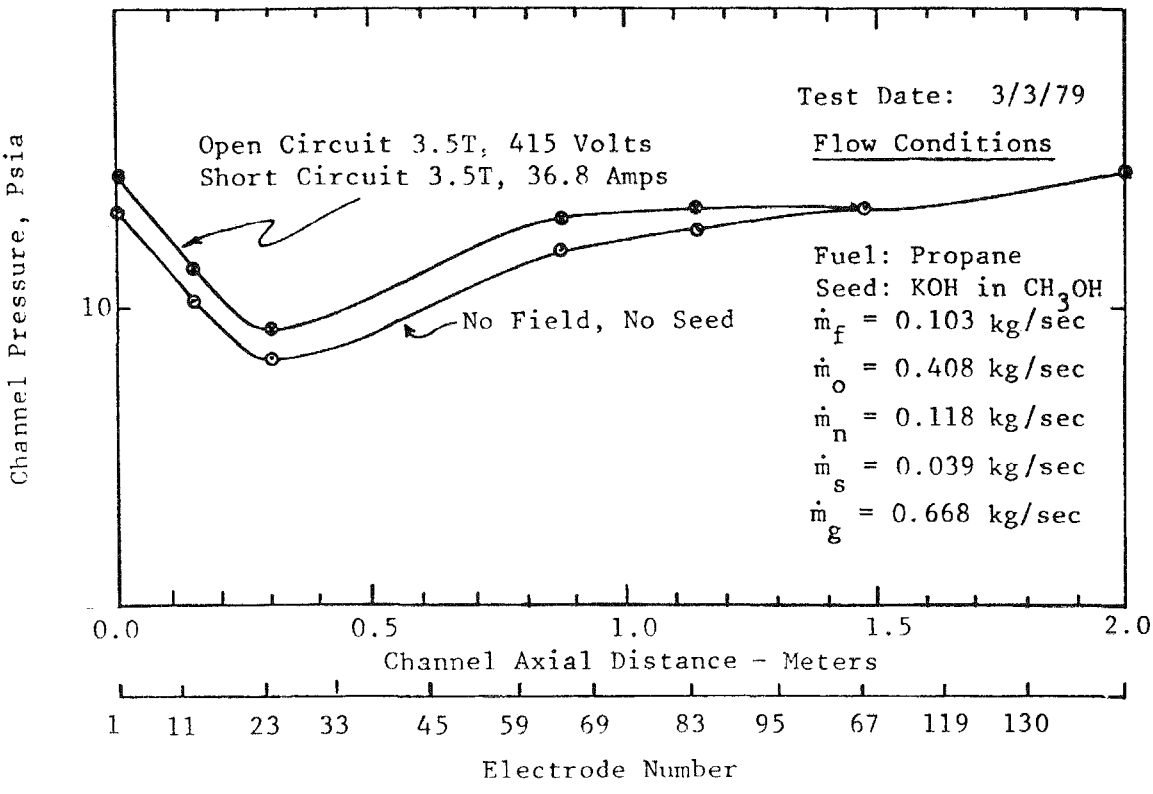

Fig. 19 Static Pressure Distribution in the Channel

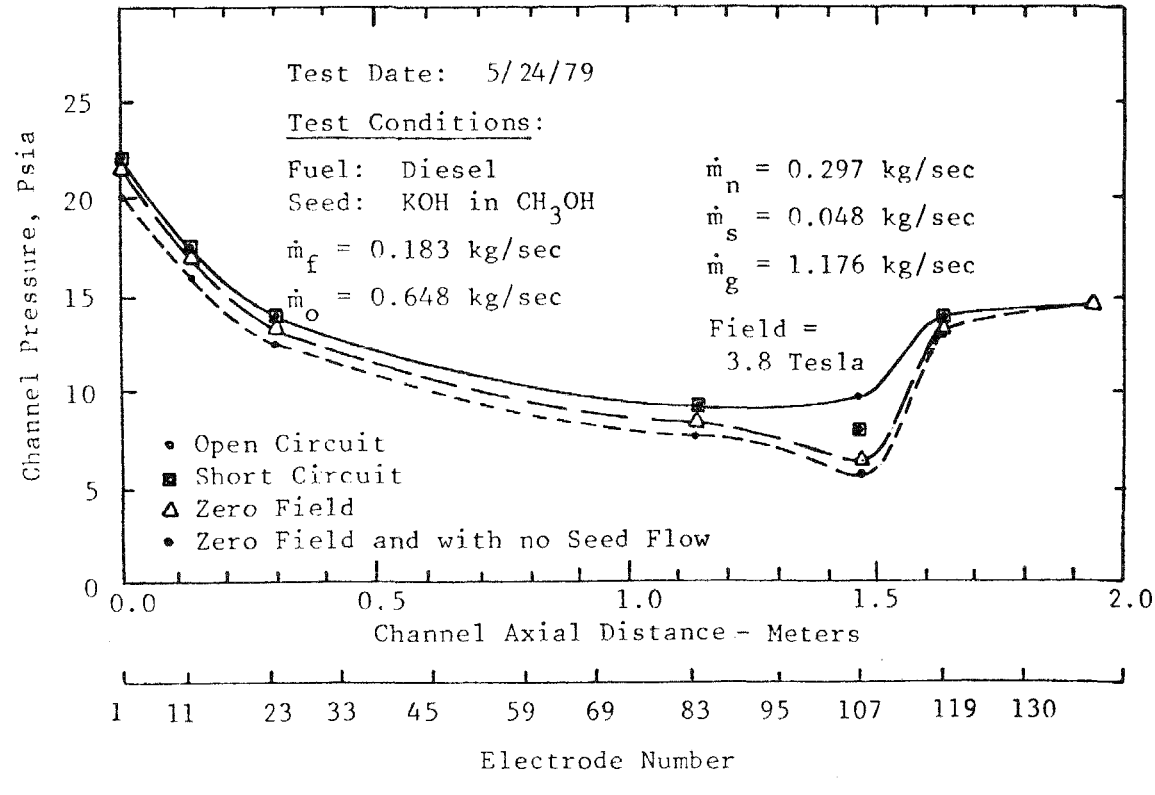

Fig. 20 Static Pressure Distribution in the Channel

4.0 OPERATION OF THE ARC GASEOUS ELECTRODE IN MHD CHANNEL - M. S. Jones, Jr., K. Sathyanarayana, E. P. Scannell

There are two key issues in the development of the arc gaseous electrode. The first is the development and operation of an arc plasma source which can operate reliably for reasonably long periods of time, as discussed in Section 3.0, and the second is the requirement that the gaseous electrode should improve the performance of the MHD channel by reducing the electrode voltage drops (and in turn, current concentrations which cause electrode damage). In this section, we will discuss experiments where the arc gaseous electrode was operated in the MHD channel under a variety of flow conditions to determine if such effects were present.

4.1 Tests of the Arc Gaseous Electrode with One-Eighth Inch Cathode

Work on the arc gaseous electrode in the Electrode Development Facility had disclosed that the arc plasma source functioned best when the arc cavity was operated at an angle to the magnetic field. For this reason, a special test section was fabricated which transitioned the plane of the electrode frames from parallel to the magnetic field to a yaw angle of 25° with respect to the magnetic field, and then back to being parallel. This allowed a special electrode frame with the arc gaseous electrode in it to be installed in the middle of the transition section, where the electrode was at an angle of 25° to the magnetic field. This test section replaced 23 of the standard frames in the 37° diagonal conducting wall channel.

The first arc gaseous electrode window frame constructed had a 1/8" diameter cathode in the annular region, with a 1/16" slot connecting the plasma generator with the MHD channel flow stream. The details of this electrode frame, shown in Fig. 3, are given in Fig. 21. This electrode was being cold-flow tested in the GTF immediately prior to the accident on October 29, 1976.

The first tests in the operating MHD generator were conducted in May 1978 after the MHD facility had been rebuilt.

One of the central questions to be answered was what would be the effect on the arc gaseous electrode of the high velocity flow field in the MHD channel. Flow tests of the arc gaseous electrode in the channel showed that a flow of about one kg/sec of oxygen and nitrogen ($N_2/O_2 = 1$) at room temperature, which produced a velocity of approximately M = 0.1, did not adversely affect the operation of the arc in the gaseous electrode. After the facility was restored, hot flow and MHD power generation tests were conducted on May 12, 1978, where the combustor was operated at a mass flow of about 0.7 kg/sec (as outlined in Section 4, the design mass flow is 1.1 kg/sec with a release of 7 MW of thermal energy). The arc gaseous electrode continued to operate with the seeded combustion products flowing in the channel past its exit. During this test, where the gaseous electrode configuration had a 1/8" tungsten cathode, it was determined that the arc gaseous electrode could be shut off, and that it would restart itself at fields up to 3.0 Tesla when the power supply voltage was turned on. This occurred without the aid of the radio frequency starter that is normally required for operation in the bench scale experiments. Channel pressure measurements on later runs without the gaseous electrode being in

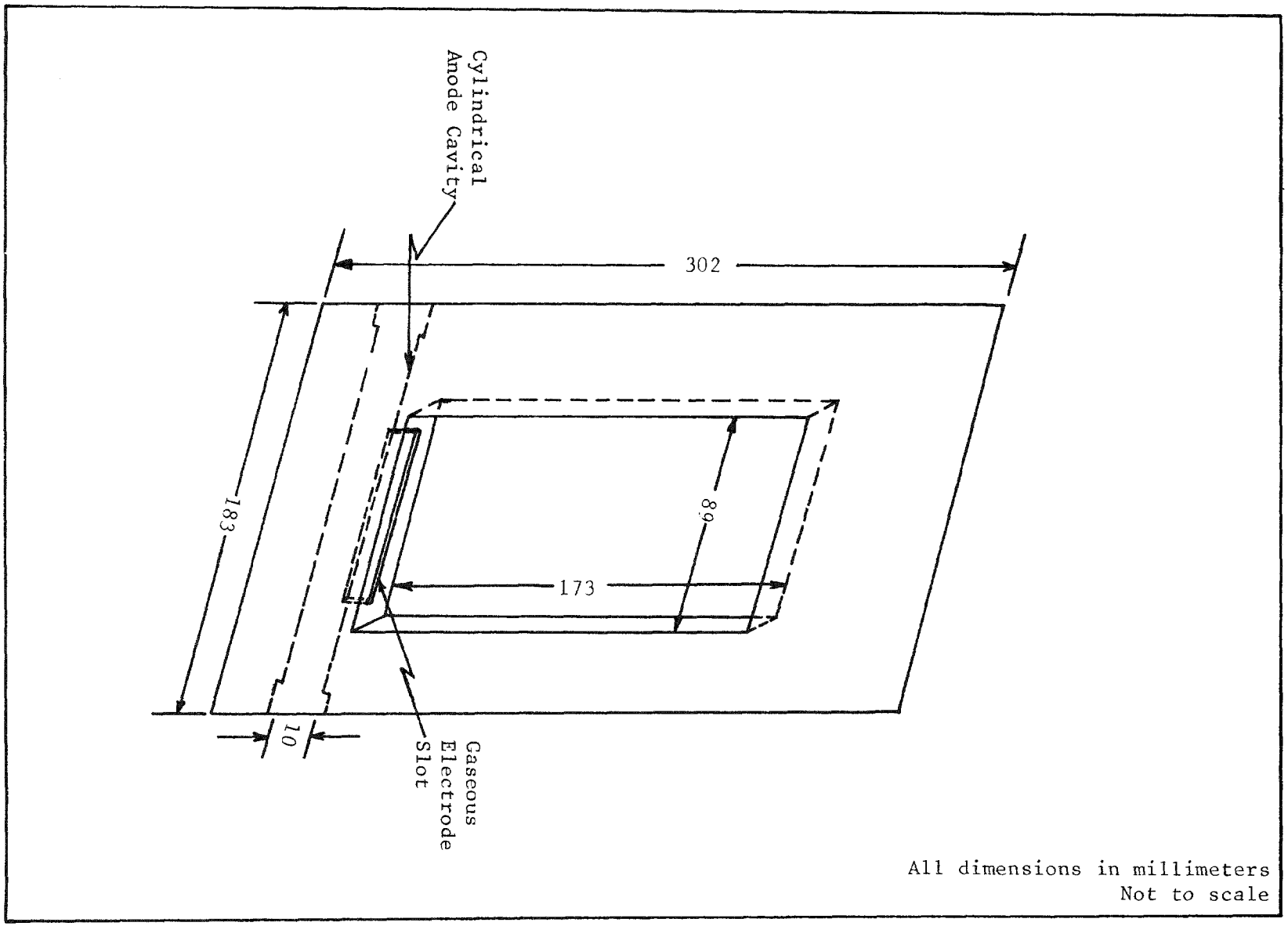

Fig. 21 Arc Gaseous Electrode Window Frame with One-Eighth Inch Cathode

place, and discussed in Section 4.2, disclosed that for this experiment the flow in the channel at the gaseous electrode location (X = 0.8 m) would be about M = 1.1 to M = 1.2 for the measured mass flow. The arc was operated for a period of about two hours, drawing a current which averaged about 55 amperes, although for short periods (1 min.) it was run at currents of about 90 amperes. Because of isolation problems between the arc power supply and the MHD load circuit, the MHD current from the arc to the MHD plasma could only be estimated as less than a few amperes.

4.2 Tests of the Arc Gaseous Electrode with One-Fourth Inch Cathode

Based on the successful test of the arc gaseous electrode with a 1/8" tungsten cathode, a new electrode frame was constructed which incorporated a 1/4" cathode. The bench scale experiments described in Section 3.0 indicated that an annular arc electrode with this larger diameter should run better at an angle of 25° to the magnetic field. This new electrode frame, which is shown in Fig. 22, incorporated several diagnostic features which, in addition to being a split frame so that the electron current from the MHD anode to the MHD cathode could be measured, included fiber optic arc motion monitoring channels for the determination of translational and rotational frequencies, and a coherent 4 mm x 4 mm fiber optic bundle (with an associated lens imaging system) which allowed visual observation of the interior of the MHD flow channel and the arc gaseous electrode efflux. Figure 23 shows a view of the arc gaseous electrode incorporated in the cathode of the frame shown in Fig. 22 when seen through the fiber optic cable system. These images can be viewed either with a TV video camera and shown on a TV monitor, or recorded photographically with a high speed Fastax camera.

This arc plasma source electrode frame, shown in Fig. 22, incorporated tangential arc gas injection in the central region, spiral gas injection at the ends, and an expanding radial contour to provide space for arc extinguishment at the ends.

Starting on May 1, 1979, a series of experiments were run incorporating this arc gaseous electrode frame in the MHD channel. Appendix C provides a summary of these runs, the test objectives, the test conditions, i.e., magnetic induction, fuel flow, oxidizer flow, seed flow, and the MHD generator output parameters such as current and voltage as recorded during selected data scans for each run. Both tungsten and copper cathodes were used. In spite of the improvements incorporated in the arc gaseous electrode configuration on the basis of the bench scale tests, its performance in the MHD channel was spotty. The system would operate with the visible gaseous effluent apparently filling the slot, when observed by the human eyes, at the start of the run. Then, the annular arc would at some time during the experiment start to rotate at one end or the other, usually the extinguishment side, presumably because of irregularities generated in the surface of the electrode by the arc. Fortunately, signals from the fiber optic arc translational motion monitors provided a confirmation of this so that data taken during these periods could be discounted. Fastax camera pictures of the arc gaseous electrode disclosed that the visible arc fflux to the MHD channel occurred about 1000 times per second, but lasting only for about 120 microseconds (the minimum time resolution of the camera) and this efflux randomly occupied only a few mm along the

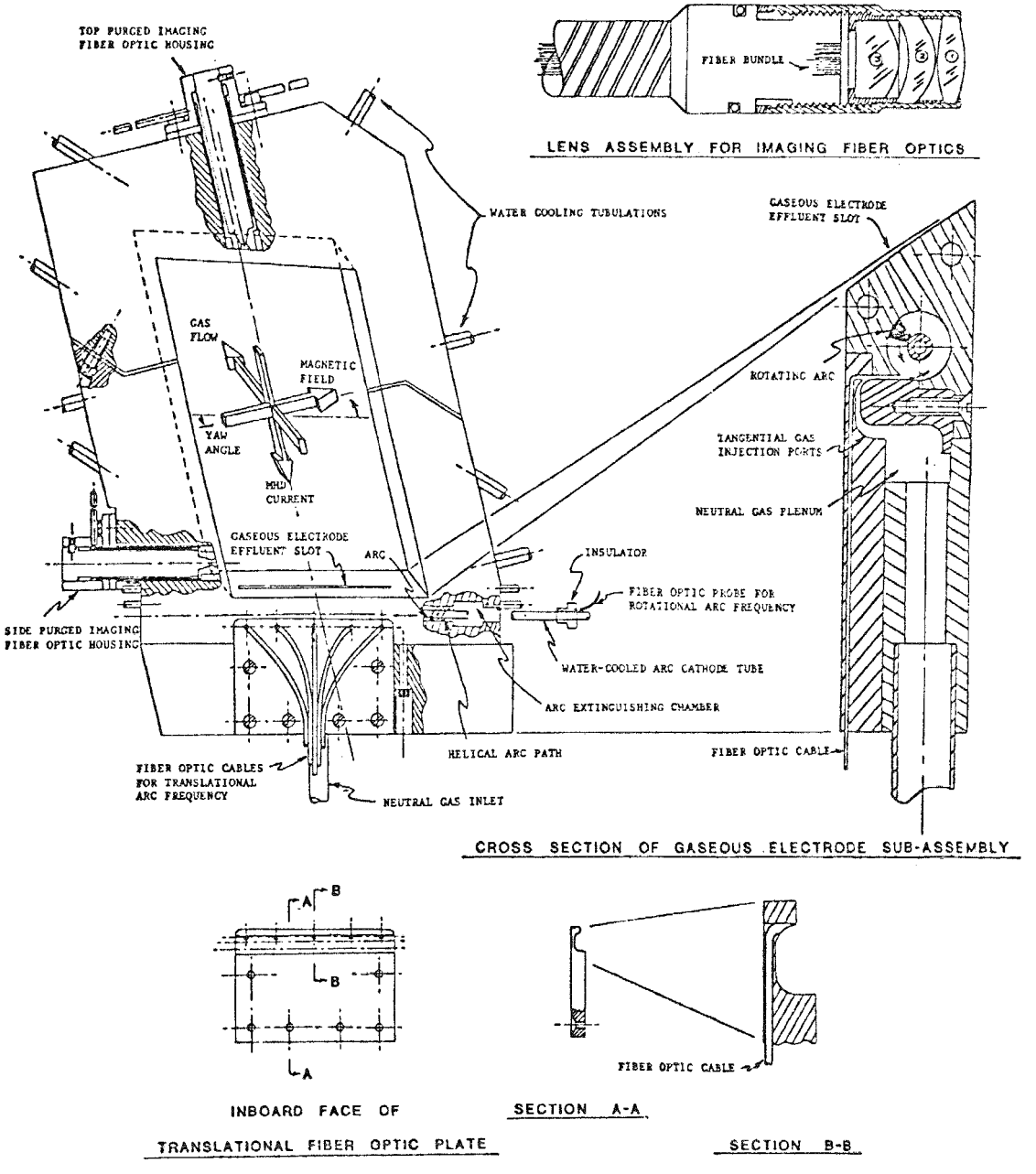

Fig. 22 Arc Gaseous Electrode Window Frame Segment with Fiber Optic Diagnostics

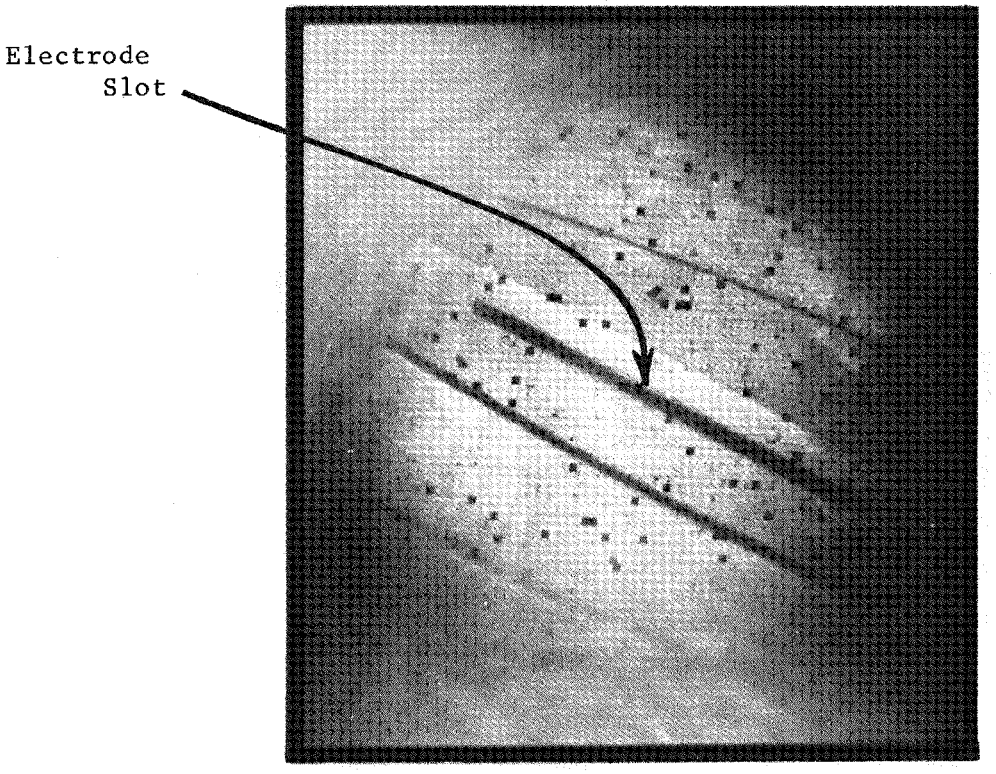

Fig. 23 View of Arc Gaseous Electrode Slot through Coherent Optical Fiber Bundle

discharge slot. At the most, visible plasma was discharged into the channel only 10%, or less, of the time. From this observation, it was clear that the arc gaseous electrode being tested, because of its intermittent nature, could only demonstrate less than one-tenth of the effects (and benefits) to be produced by a continuous plasma source in the same geometry.

Three criteria were developed for evaluating the effectiveness of the arc gaseous electrode in the MHD channel. These were:

1. The effect on the MHD generator characteristics in the immediate vicinity of the arc gaseous electrode when it was operating.

2. The effect of the arc gaseous electrode on the overall performance of the MHD generator.

3. The effect on the arc gaseous electrode of changes in MHD generator operation.

In addition, several experimental observations were made which provide more insight to our understanding of the operation of the arc gaseous electrode and MHD generators. Figure 24 shows the electrical measurement circuits used to evaluate the performance of the MHD channel and the arc gaseous electrode.

4.2.1 Split Plate Currents

One method of examining what is happening in a diagonal conducting wall MHD generator is to measure the currents which are passing from the generator cathode to anode through the conducting walls. This can be done by splitting the plate, as shown in Fig. 25, insulating the two halves from each other, and putting a small resistor (1 mΩ) so as to connect the two halves. By measuring the voltage drop across this resistor, the current flowing between the MHD cathode and anode can be determined. In the MHD generator, this current is a function of the electrode area and the transverse plasma current density which, in turn, is dependent upon the plasma conductivity, magnetic field, plasma velocity, and the plasma voltage drop in the electrode plasma boundary layer.

Figure 26 shows the currents measured through the split plates along the channel as a function of distance for open circuit and short circuit conditions. The low currents at the front of the channel are presumably due to the low level of ionization in that portion of the flow. In the rest of the channel, changing from open circuit to short circuit reduces the current flow to the walls, in general agreement with theory.

For the data shown in Fig. 27, the arc gaseous electrode test section was in place and the split plate current was measured at the arc gaseous electrode frame, which is 0.019 m (3/4") thick whereas the other frames were only 0.0095 m (3/8") thick. Therefore, the net current to this frame, for the same transverse current density, should be a factor of two higher, but the observed current is about 25% higher than this theoretical value. This may be due to aerodynamic

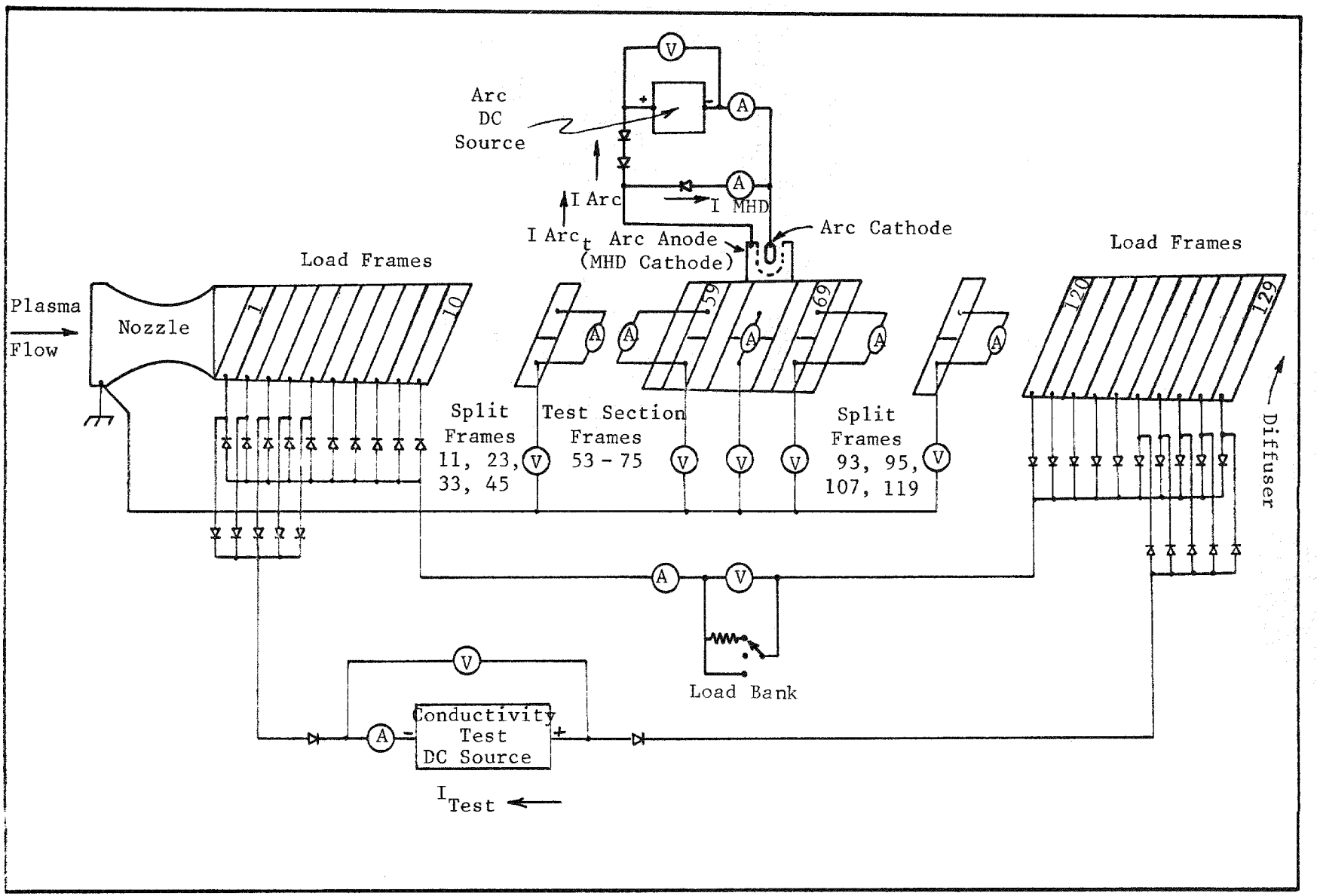

Fig. 24 MHD Channel Arc Gaseous Electrode Test Setup

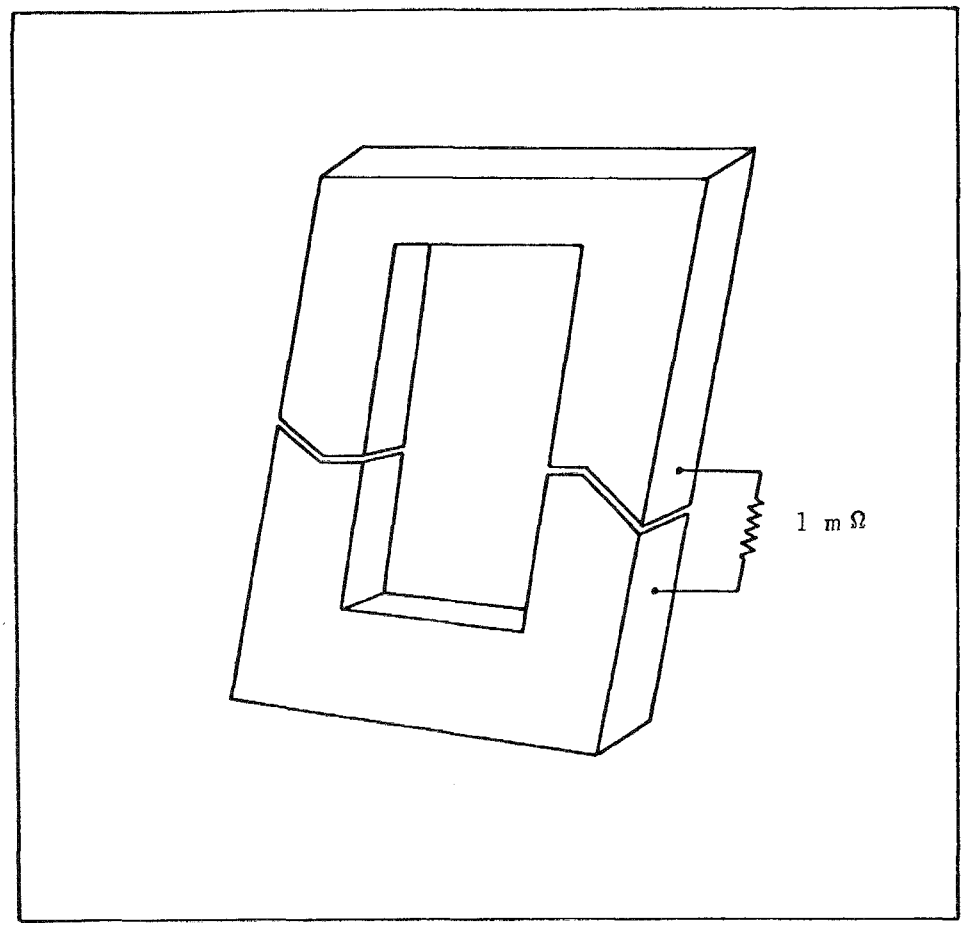

Fig. 25 Split Plate Current Measurement Technique

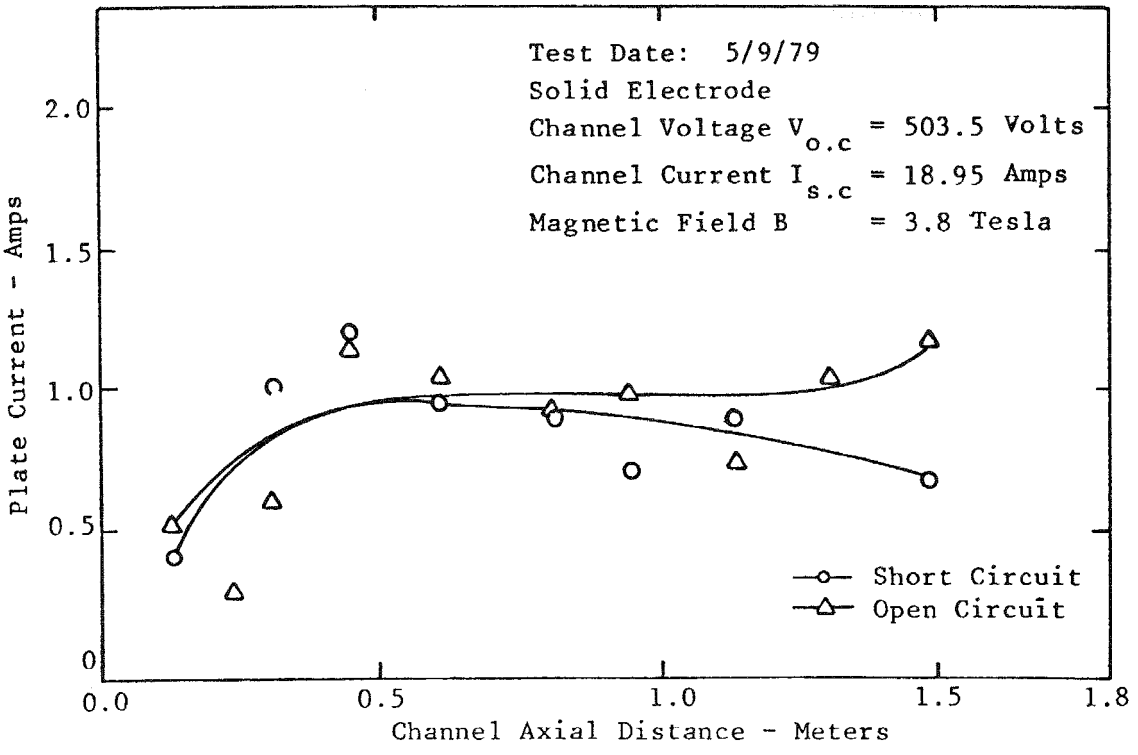

Fig. 26 Current Distribution Along the Channel with Solid Electrode

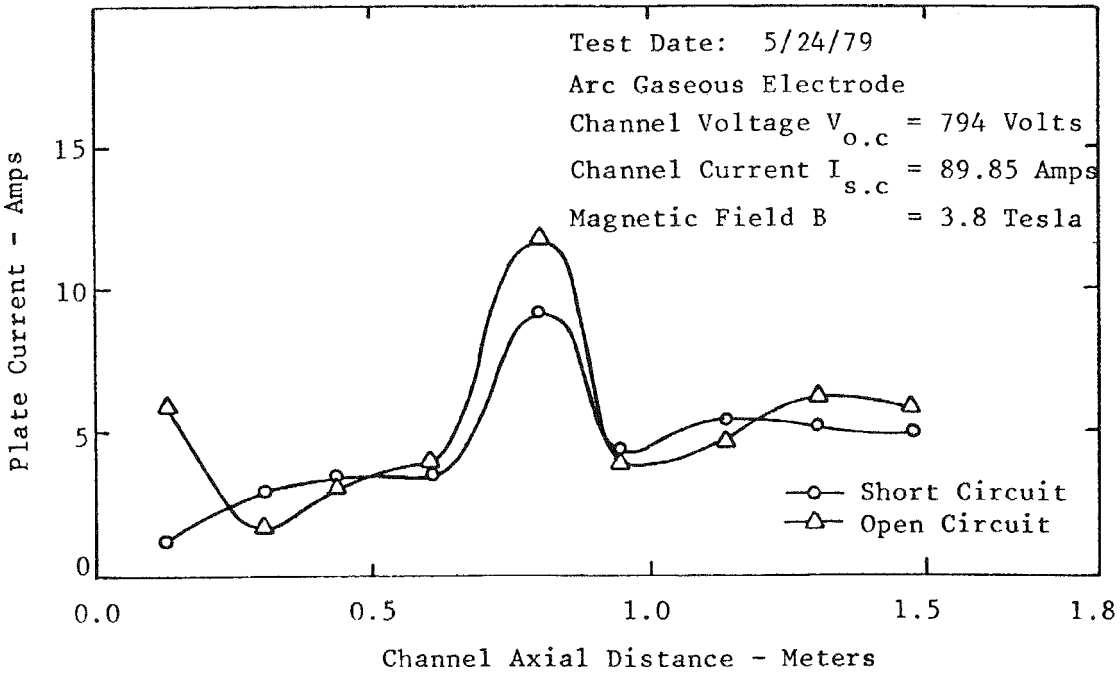

Fig. 27 Current Distribution Along the Channel with Arc Gaseous Electrode

effects because of the efflux through the slot in the electrode face which could cause some mixing in the boundary layers.

In order to examine the performance of the arc gaseous electrode, it is instructive to compare the currents which are measured in the split electrode frame which contains the arc gaseous electrode with the currents which are measured in other split electrode frames along the channel. By looking at the ratio of the currents in the individual frames, the measurements tend to become independent of the plasma conductivity, gas velocity, magnetic field, etc. This leaves the electrode voltage drop as the major cause of the observed current variations.

Because of the variation in gas conductivity which occurs along the channel, as discussed in Section 4.2, it appears appropriate to only compare the arc gaseous electrode frame currents with the currents in the two adjacent split frame currents which are about 0.2 m upstream and downstream from the gaseous electrode frame. Inasmuch as operation of the arc gaseous electrode could cause some variation in the boundary layer properties, which might affect the split frame downstream from the arc gaseous electrode, the most meaningful comparison can be made by comparing the current in the arc gaseous electrode frame with the current in the split frame immediately upstream. As mentioned earlier, the electrode frame with the arc gaseous electrode is 0.019 m thick while the other split frames are only 0.0095 m thick; therefore, if the transverse plasma current densities are the same, the ratio, R, between these two currents should be 2.0.

Table 1 shows data from the run on May 24, 1979, and gives the time of the data scan; the magnetic induction in Tesla; the current in split frame 45; the current in split frame 69 (which contained the arc gaseous electrode); the ratio of the two currents, R; the MHD generator output voltage, V_{gen}; the MHD generator output current, I_{gen}; and the current being carried by the annular arc in the gaseous electrode frame, I_{arc}. If we exclude the one reading taken at 10:53:18, we find that the average value for R is 3.1 ± 0.77 when the arc gaseous electrode is on, while the average value for those measurements which were taken when the arc gaseous electrode source was off, i.e., $I_{arc} = 0$, is 2.59 ± 0.33, rather than the theoretical value of 2.0. The difference between the measured and the theoretical value may be due to an increase in electrical conductivity, as discussed in Section 4.2, which would increase the transverse plasma current at the downstream (arc gaseous electrode) frame.

One conclusion which may be drawn from this measurement is that operation of the arc gaseous electrode may have resulted in an increase of current to the electrode frame of $3.11/2.59 = 1.20$ or 20%; however, such a variation may be within the statistical variation of the sample. It must be concluded from the above data that there is no strong evidence that the arc gaseous electrode is capable of reducing the electrode boundary layer voltage drop in the vicinity of the electrode which contains the arc gaseous electrode.

4.2.2 Voltage Profile Measurements

The evaluation of the performance of the arc gaseous electrode is to determine what effect its operation has on the generator voltage profile.

TABLE 1.

MHD TEST DATA, MAY 24, 1979

Data Scan Time	Magnetic Field	I_{45}	I_{69}	$R=I_{69}/I_{45}$	V_{gen}	I_{gen}	I_{arc}
	Tesla	Amps	Amps		Volts	Amps	Amps
10:23:33	3.0	.45	2.2	4.9	287.5	0	59.2
10:26:39	3.0	3.6	11.1	3.1	680	0	62.4
10:27:27	3.0	3.3	7.85	2.4	0	73.5	59.4
10:28:19	3.0	3.9	11.95	3.06	794	0	57.6
10:29:08	3.0	3.55	9.35	2.63	0	89.9	58.4
10:29:56	3.0	3.0	8.15	2.72	20	81.2	58.8
10:41:37	3.83	3.65	10.95	3.0	749	0	57.7
10:43:20	3.83	2.9	8.8	3.03	670	0	55.5
10:53:18	3.83	0.15	1.3	8.67	862.5	0	0
10:54:11	3.83	5.4	11.65	2.16	0	>100	0
10:55:05	3.83	5.6	14.05	2.51	826	0	0
10:55:53	3.06	4.85	13.35	2.86	759	0	0
10:56:41	3.06	3.65	10.3	2.82	0	89.5	0

Run conditions: $\dot{m}$ = 1.18 Kg/sec; N_2/O_2 = 0.46; seed = 1% K

Electrode voltage drops in MHD channels with water cooled walls may be of the order of 70 to 100 volts. Therefore, if the arc gaseous electrode were to short out the voltage drop at this particular electrode, then it is expected that the channel voltage profile would see a discontinuity of the magnitude of the voltage drop at that location, and that there would be a general increase in voltage for all stations downstream of the arc gaseous electrode.

During the run on May 24, 1979, voltage profile data were taken during the scans at 10:41:37 when the arc gaseous electrode was on, and at 10:53:18 and again at 10:55:35 when the arc gaseous electrode was off. These axial voltage profiles, shown in Fig. 28, are for open circuit conditions.

These data show that the channel voltage with respect to ground at the location of the arc gaseous electrode (0.8 m) was different for the two data scans when the arc gaseous electrode was off. However, we may note that there is no sudden jump in the voltage profile at that location when the arc gaseous electrode is operating. This indicates that the arc gaseous electrode has not shown any reduction in the electrode boundary layer voltage drop. This effect may be due to the poor performance of the arc gaseous electrode, as explained earlier, in MHD channel flow conditions.

4.2.3 Interaction of the MHD Flow with the Arc Gaseous Electrode Current

In the original concept, it was postulated[1] that the annular arc would carry part of the MHD current. Therefore, there should be a change in the arc current when the transverse current in the channel flow is changed. This can be accomplished by loading and unloading the generator.

As may be seen by examining the data in Table 1, going from open circuit to short circuit did not produce any significant effect on the annular arc current, I_{arc}. It is known from the split plate measurements that the total transverse current (I_{69}) is of the order of 10 amperes. It must therefore be concluded that the arc gaseous electrode does not carry a significant fraction, if any, of the electrode current. These data confirm the observations made during tests with the 1/8" tungsten cathode reported in Section 5.1. Since most of the time AGE did not work in the channel, no conclusion can be drawn as to whether it is capable of carrying any current.

4.2.4 Time-Resolved Current Measurements

High speed (8000 frame/sec) motion pictures of the inside of the MHD channel at the gaseous electrode frame through the coherent fiber optic cable bundle disclosed that there were occasional very bright spots which appeared on the cathode surface. These spots only showed up on one frame of the film, and then disappeared. This indicates that the lifetime of the event photographed was less than about 120 microseconds.

To investigate the matter further, time-resolved measurements were made of the voltage appearing across a one milliohm shunt which connected the two halves of the split plate diagonal wall electrode, as shown in Fig. 25. The purpose of the shunt is to measure the current flowing in the frame sidewall.

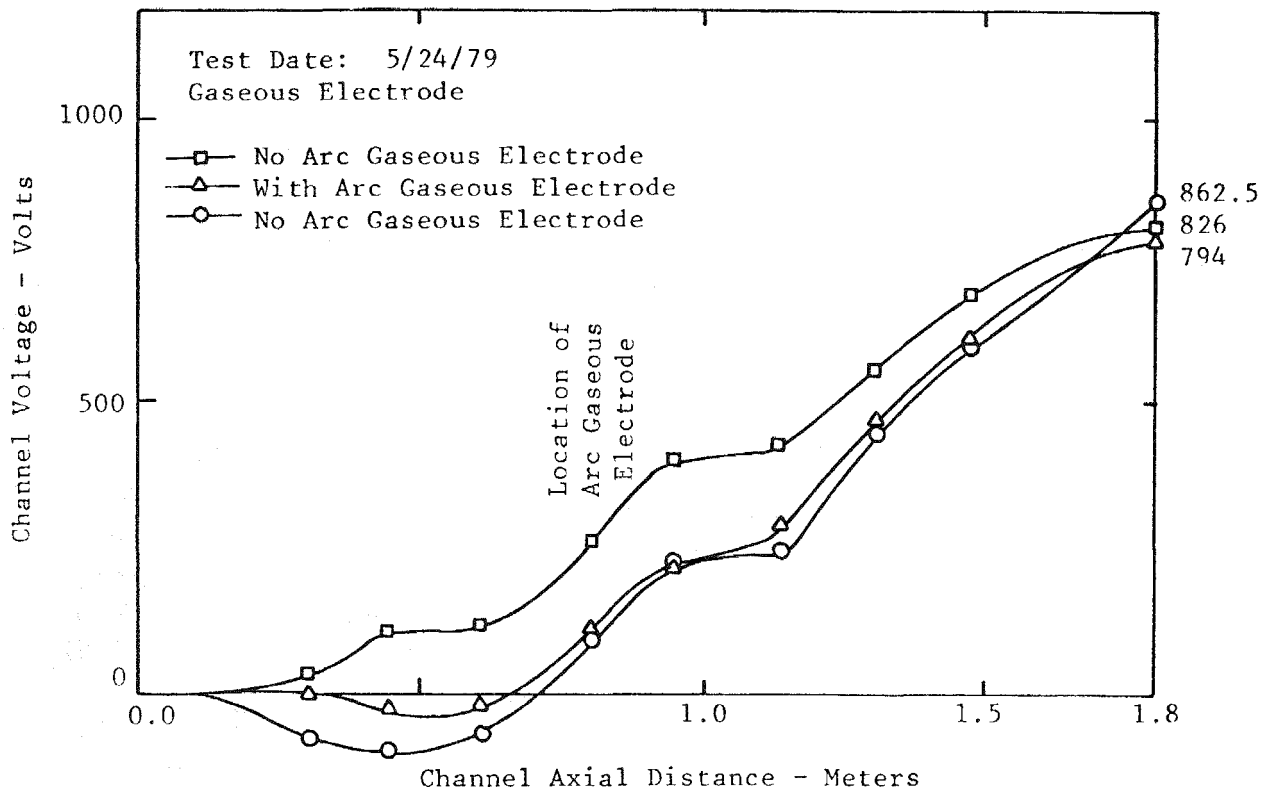

Fig. 28 Channel Voltage Variation Along the Channel with and without Arc Gaseous Electrode

Figure 29 shows oscilloscope traces recorded with a time base of one millisecond per cm for the horizontal axis. The vertical axis is the split plate current. One cm vertical deflection is equal to 67 amperes. For the upper trace, the arc gaseous electrode was operating, while for the lower trace it was off. It is seen that the current is very irregular and appears as a series of short spikes, the duration of which are 100 microseconds or less. During the period when these oscillographs were taken, the current passing through the shunt, when measured by a time averaging meter, was 6 amperes.

Figure 10 is a histogram of the current pulse heights for the two traces. It may be noted that the median pulse height is about 13 amperes, and if the pulses are 100 microseconds in length, they account for about half of the time, 4.5 msec out of the 10 msec period. This implies that there must be extended periods when the current through the electrode frame is very low. There is essentially no difference in the pulse height distributions whether the arc gaseous electrode is on or off. Therefore, we must conclude that the arc gaseous electrode is not effective in eliminating these high amperage pulses which apparently are the major cause of electrode damage. Further evaluation of this phenomenon may lead to a better understanding of electrode wear mechanisms in MHD channels.

4.2.5 MHD Power Generation

One of the best methods of judging the output of the MHD generator is to measure the voltage-current characteristics. This is accomplished by changing load resistance, R_L, from infinity (open circuit) to zero (short circuit), passing through intermediate values of load resistance. From these measurements, the generator internal resistance, R_I, can be determined. When the external load R_L equals R_I, then the maximum amount of power will be transferred from the generator to the external load.

Typical current-voltage characteristic data for the 37° diagonal conducting wall channel are shown in Fig. 31 where the voltage and current for the three conditions are plotted. These are: (1) open circuit, (2) R_L = 10.46 ohms, and (3) short circuit. The average open-circuit voltage is 825 $\pm$ 30.5 V while the average short-circuit current was 43.5 $\pm$ 2.83 amperes. Under load, the generator produced 11.125 $\pm$ 1.1 kw, roughly 33 amperes of output at 340 volts.

For future tests, additional load resistors at about 20 ohms and 5 ohms, and the combinations which can be achieved by placing the various resistances in parallel, will allow more details of the load characteristic curve to be examined.

4.2.6 Experimental Conclusions

From the Fastax pictures of the arc gaseous electrode, it is clear that visible plasma was being injected into the MHD channel electrode boundary layer only a small percentage of the time, probably much less than 10%. Also during this short time, the arc was observed to be located at one or the other end of the slot. Therefore, it is concluded that the effect of the arc on MHD current transfer is negligible as observed before through the histogram of current

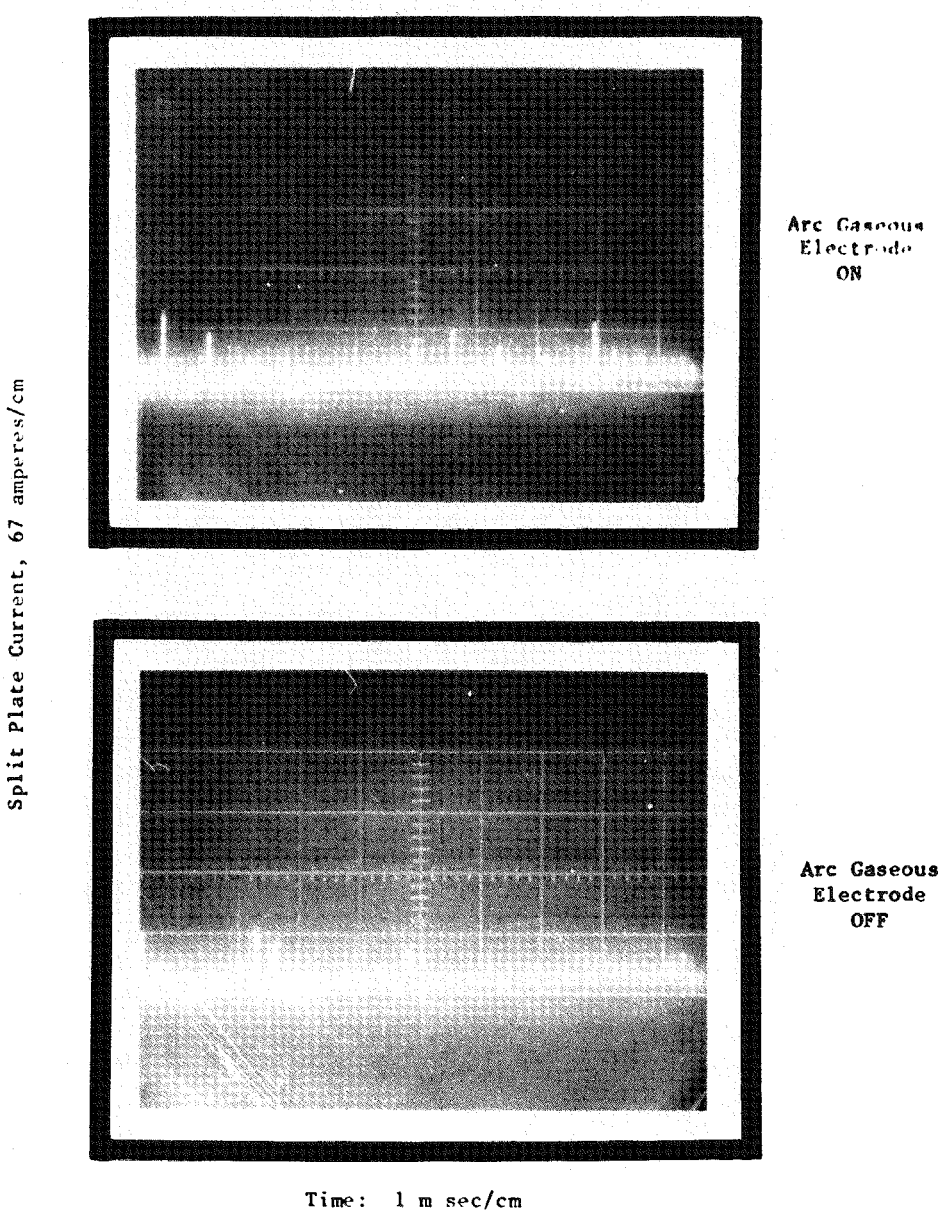

Fig. 29 Diagonal Conducting Wall Split Plate Current

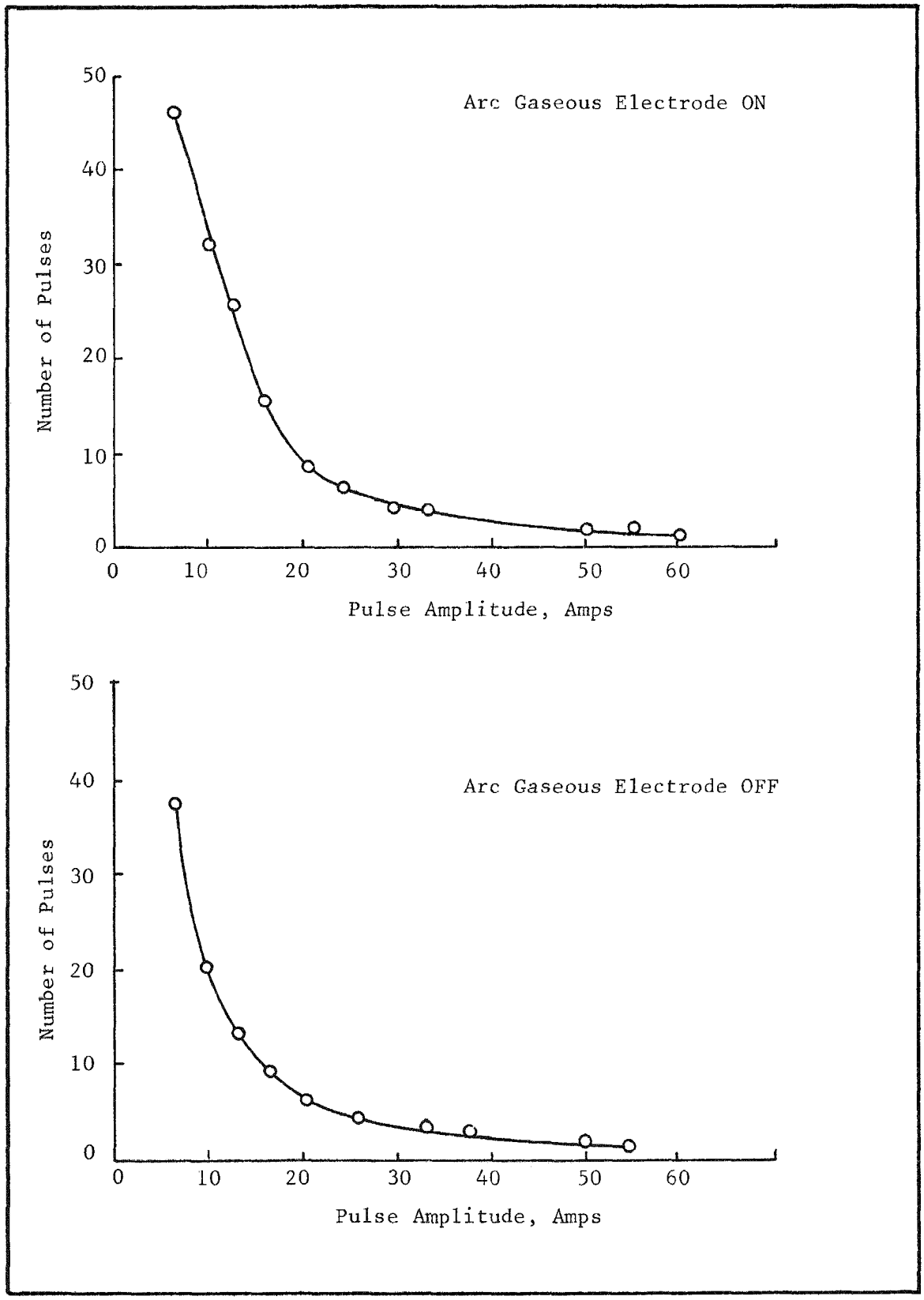

Fig. 30 Histogram of Current Pulses

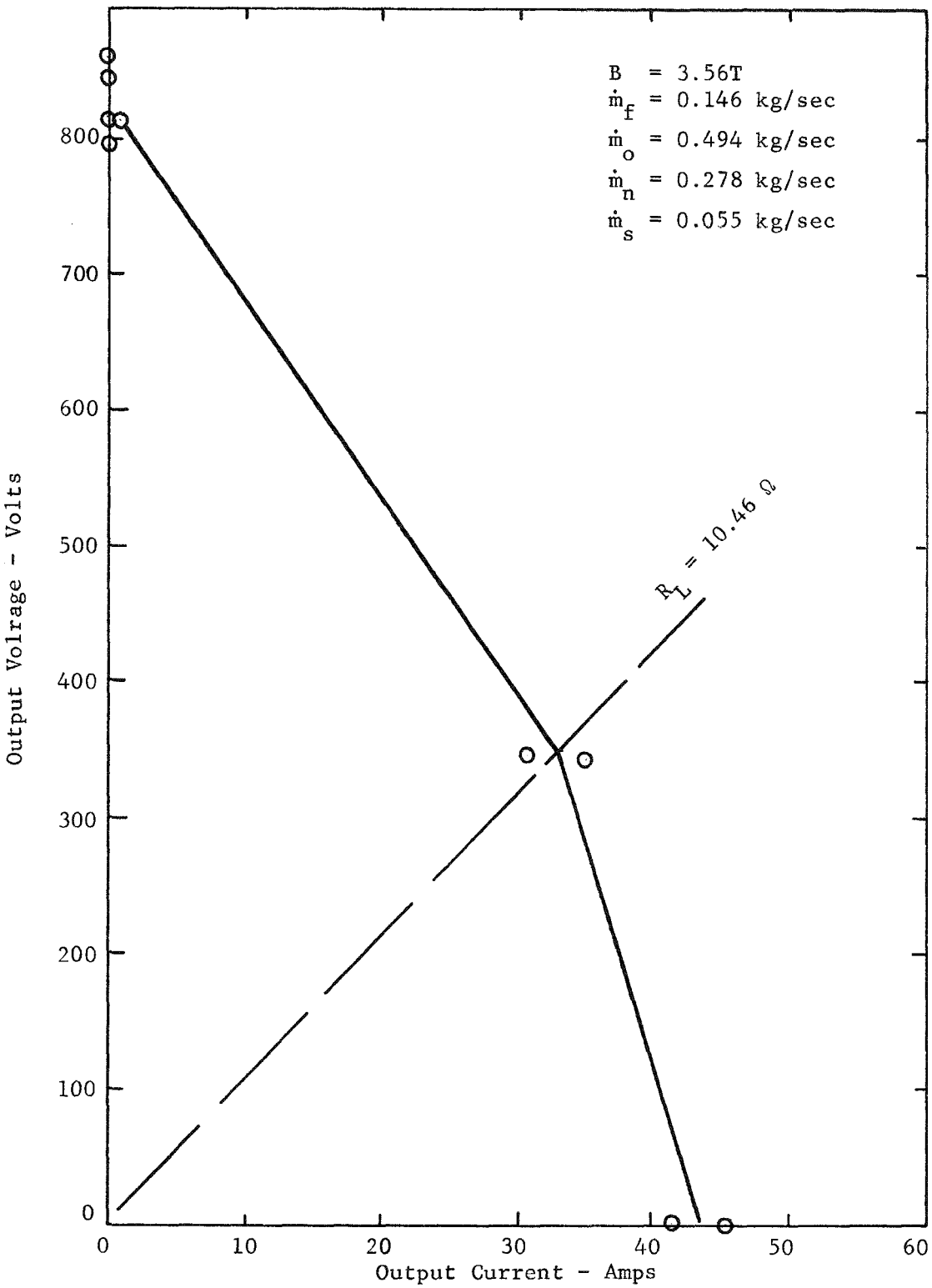

Fig. 31 37° Diagonal Conducting Wall Generator
Experimental Output Characteristics

pulses (Fig. 30). If the plasma from the arc source is to be used as a conductor between the MHD plasma and the arc source cathode, as described in Reference (1), then the arc in the gaseous electrode slot should be uniform and continuous.

Following the same reasoning, but only requiring that the ejected plasma "short out" the boundary layer voltage, i.e., predicting that the plasma operates as a boundary layer modification technique allowing the current to flow to the surface of the electrode frame in a diffuse discharge and that the generator electrode surfaces are not required explicitly to take part in the current transfer, one would expect that the effect on the time-averaged value of the boundary layer electrode voltage drop would also be small.

If the current carrying properties of the arc plasma are discounted, there may be some advantage to introducing plasma into the electrode boundary layer to increase the ionization of the potassium seed. However, the optical data tells us that the plasma injection from the arc gaseous electrode would occur only over a small region (a few mm wide) and that it would occur about 1000 times per second. However, we may note that the combustion product plasma is passing the arc gaseous electrode at a velocity of about 1000 m/sec. Therefore, the volumes of the boundary layer flow that have had their properties modified by the plasma injection should be about a meter apart. Under these conditions, we would again not expect to see a very large physical effect.

Against the above background, it is not surprising that operation of the arc gaseous electrode did not change the MHD channel axial voltage profile, and did not change the open-circuit voltage or short-circuit current. These results may be interpreted that the arc gaseous electrode plasma was not in contact with the MHD plasma for enough of the time to have had any effect. The same reasoning may be applied to the fact that changing the plasma transverse current density did not change the current in the gaseous electrode plasma arc.

Basically, the optical data predicts that any of the electrical effects resulting from the arc gaseous electrode will be very small, and this was confirmed by the measurements of the generator characteristics.

The apparent increase in the current through the electrode frame which contained the arc gaseous electrode may be due to the effect of having hot argon injected into the electrode boundary layer when the arc is on. This effect would not require that the hot argon be able to conduct current, as is required if the annular arc surfaces are to be part of the circulating current system, but only that the hot argon injected into the boundary layer increases the ionization of the potassium seed already in the MHD boundary layer flow and hence increases the local conductivity in the boundary layer. It is the reduced conductivity in the cold boundary layer which leads to the arcs that damage the electrodes. Therefore, we may have evidence that the efflux from the arc gaseous electrode is acting as a boundary layer modification technique. Boundary layer modification experiments by Fushimi[4] have shown that a significant reduction in electrode drops, from 120 to 25 volts, could be achieved by injecting plasma (from a thermal source) equivalent to a small percentage of the total flow at the electrode surface. Reduction in electrode

voltage drops should reduce electrode erosion and should result in longer generator operating lifetimes.

Because of the intermittent nature of the plasma discharge from the arc gaseous electrode, it does not appear to be suited for use in boundary layer modification applications. Sources which can supply plasma continuously such as thermal sources, radiofrequency discharges, or microwave discharges appear to be very useful for the development of the gaseous electrode concept.

In summary, the present program has resulted in the development of an arc plasma source which can fit in an MHD generator frame. Based on the bench scale tests, it has shown promise for extended periods of operation in the MHD generator environment. However, the arc plasma did not produce a continuous efflux when operated in an MHD channel. Therefore, until such time as boundary layer modification in MHD channels is well understood and it is clear that the periodicity in the output of the arc plasma generator might be tolerated so that it could be used as a plasma source for boundary layer modification, it is recommended that no further work be done on the arc gaseous electrode.

5.0 MHD CHANNEL FLUID FLOW ANALYSIS - K. Sathyanarayana, M. S. Jones, Jr.

5.1 Analytical Model

The analytical model is based on a coupled core flow - boundary layer concept. The flow through the central core of the generator is treated as a quasi-one-dimensional channel flow. The boundary layer development on the insulator (B-) and electrode (E-) walls is calculated using the integral form of the boundary layer equations. These two flows are coupled through the boundary layer displacement thickness effect on the core flow development and by the boundary layer shorting effect on the electric field.

5.2 Governing Equations

The quasi-one-dimensional model for the diagonal conducting wall MHD channel (Fig. 32) is developed for the calculation of generator performance and assumes, as shown in Fig. 33, that an inviscid core exists for the entire length of the channel and viscous effects are confined to the immediate neighborhood of walls. Thus the analysis of the flow is divided into two parts: the inviscid core flow with MHD body forces and energy transfer, and the boundary layers which may be treated as a flat plate with velocity gradients imposed both by the static pressure gradient and the MHD force.

The inviscid core flow in an MHD generator is essentially one-dimensional (Ref. 4) and is governed by the equations of momentum:

$$\rho_c u_c \frac{du_c}{dx} = - \frac{dp_c}{dx} + j_{yc} B_z \tag{1}$$

energy:
$$\rho_c u_c \frac{dH_c}{dx} = \rho_c u_c \left(\frac{dh_c}{dx} + u_c \frac{du_c}{dx}\right) = j_{xc} E_x + j_{yc} E_y \tag{2}$$

continuity:
$$\dot{m} = \rho_c u_c A_c \tag{3}$$

and state:
$$\rho_c = \rho_c (p_c, T_c) \ . \tag{4}$$

In the inviscid core, the Equation (1) represents the conservation of momentum for the fluid along a streamline. The term $j_{yc} B_z$ in Equation (1) is the so-called MHD body force. The conservation of energy for the core flow along a streamline is represented by Equation (2). The terms on the right hand side of the equation result from the interaction of the fluid and the electric field. The energy loss due to radiation has been assumed negligible. The continuity equation, in a global sense, is represented by Equation (3) and it is through this equation that the channel geometry and viscous boundary layer effects are included. Here, ρ_c, u_c, and A_c are the density, velocity, and area of the core flow. The core area is defined as the physical cross-sectional area of the channel minus the "blocked" area resulting from the viscous flow

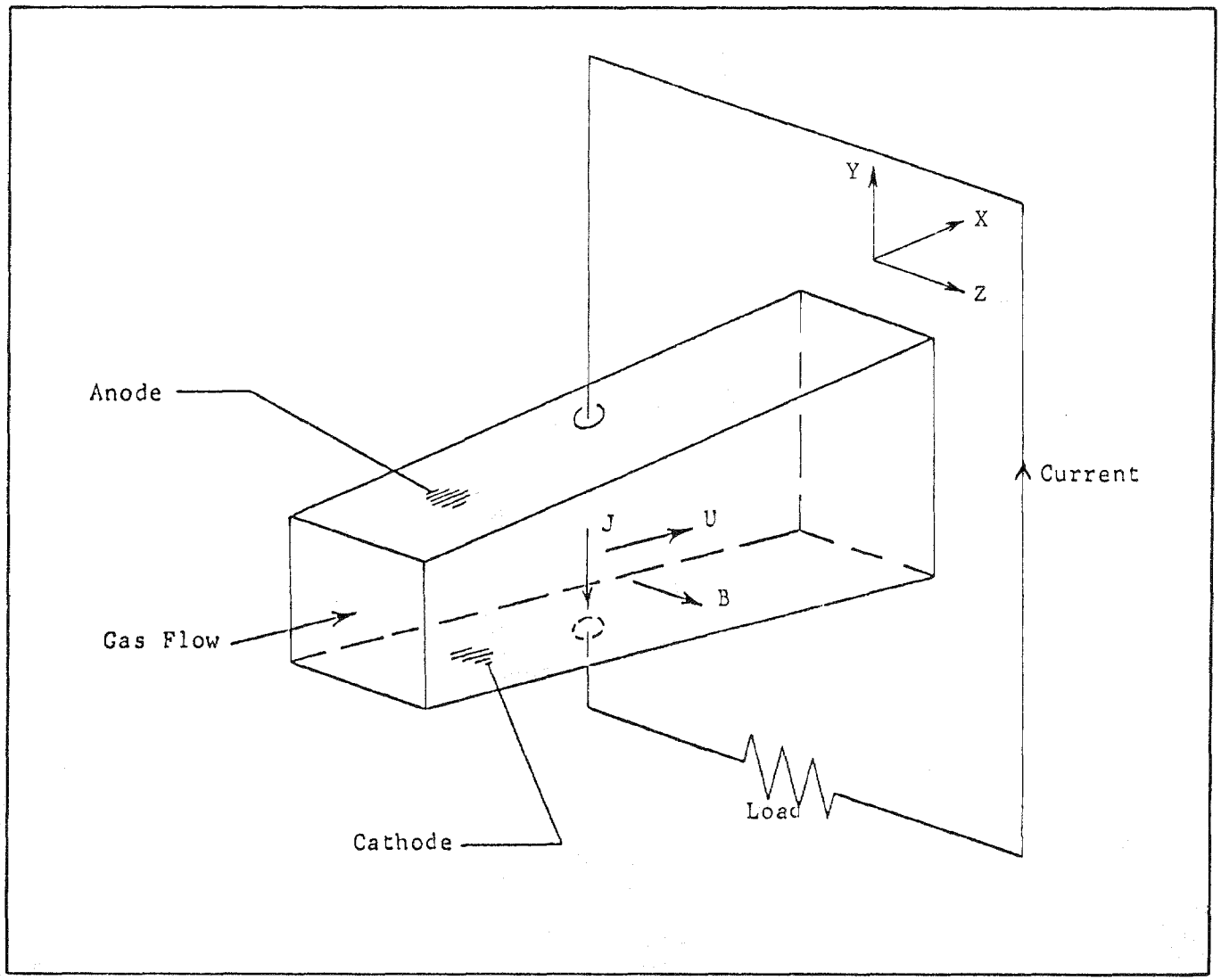

Fig. 32 Schematic Diagram of MHD Generator and Coordinate System

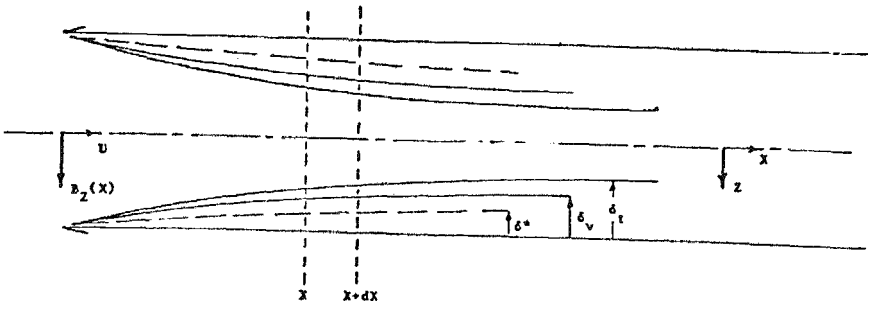

Fig. 33a Schematic of Magnetic Field Wall Boundary Layer

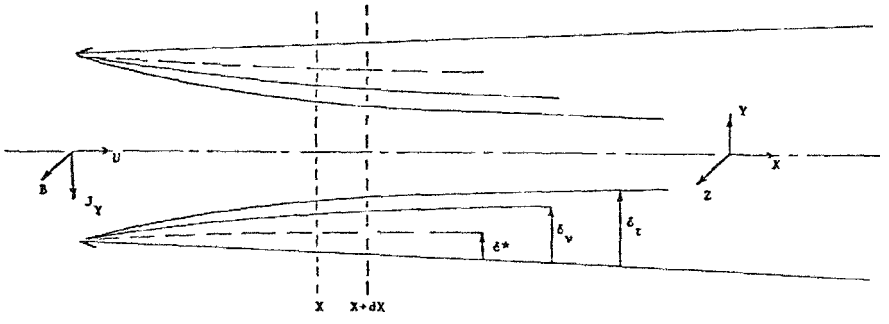

Fig. 33b Schematic of Electrode Wall Boundary Layer

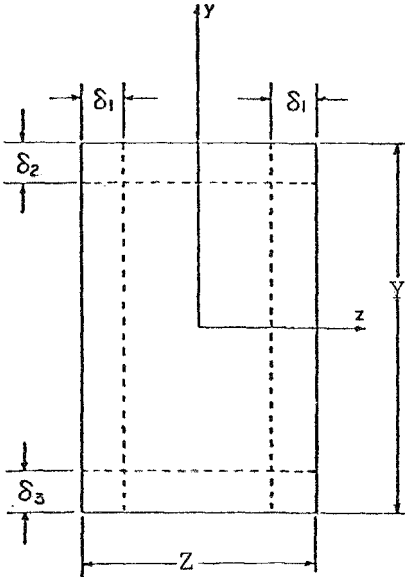

Fig. 33c Schematic representation of cross-section of the channel identifying dimensions used in calculation of the core area.

regions adjacent to the wall. The thermal equation of state is defined by the Equation (4) where the function $\rho_c(p_c, T_c)$ is obtained by using a second-degree surface fitting interpolation procedure (Ref. 5).

Modified Form of Core Flow Equations:

A more convenient form, particularly for real gas calculations, can be obtained by solving Equations (1) - (4) explicitly for the pressure and temperature gradients dp_c/dx and dT_c/dx. This leads to the following equations for the core flow development (Ref. 6).

i.e.,

$$\frac{dp_c}{dx} = - \frac{u_c^2 \left(\frac{\partial \rho}{\partial T}\right)_p \left[j_{xc} E_x + j_{yc}(E_y - u_c B_z)\right]}{\rho_c u_c C_p (M_c^2 - 1)} - \frac{\rho_c u_c C_p \left[j_{yc} B_z + \frac{\rho_c u_c^2}{A_c} \frac{dA_c}{dx}\right]}{\rho_c u_c C_p (M_c^2 - 1)} \tag{5}$$

and,

$$\frac{dT_c}{dx} = \frac{\left[u_c^2 \left(\frac{\partial \rho}{\partial p}\right)_T - 1\right] \left[j_{xc} E_x + j_{yc}(E_y - u_c B_z)\right]}{\rho_c u_c C_p (M_c^2 - 1)} + \frac{\frac{T_c}{\rho_c}\left(\frac{\partial \rho}{\partial T}\right)_p \left[j_{yc} u_c B_z + \frac{\rho_c u_c^3}{A_c} \frac{dA_c}{dx}\right]}{\rho_c u_c C_p (M_c^2 - 1)} \tag{6}$$

These equations are better suited for coupled solutions with the boundary layer equations.

Boundary Layer Equations for the Magnetic Field Wall

The integral form of the boundary layer equations is achieved by integrating the differential momentum and energy equations in the Z direction at constant streamwise location, X. For example, the momentum equation for the B-wall boundary layer is

$$\rho u \frac{\partial u}{\partial x} + \rho w \frac{\partial u}{\partial z} = - \frac{\partial p}{\partial x} + \frac{\partial \tau_{xz}}{\partial z} + j_y B_z \tag{7}$$

Integral Form

A formal integration of Equation (7) with respect to Z, between the limits of Z = 0 and Z = δ, together with the substitution of Equation (1) to eliminate the core flow pressure gradient leads to

$$\frac{d\theta}{dx} + \theta\left[\frac{(\delta^*/\theta) + 2}{u_c}\frac{du_c}{dx} + \frac{1}{\rho_c}\frac{d\rho_c}{dx}\right] = \frac{C_f}{2} + \frac{j_{yc}B_z}{\rho_c u_c^2}\delta^*_{JB} \tag{8}$$

Energy Equation

The energy equation for the B-wall boundary layer is

$$\rho u\frac{\partial H}{\partial x} + \rho W\frac{\partial H}{\partial z} = -\frac{\partial q}{\partial z} + \frac{\partial}{\partial z}(u\tau_{xz}) + j_x E_x + j_y E_y \tag{9}$$

Integral Form

A similar integration of the Equation (9) leads to

$$\frac{d\phi}{dx} + \phi\left[\frac{1}{\rho_c}\frac{d\rho_c}{dx} + \frac{1}{u_c}\frac{du_c}{dx} + \frac{1}{(H_c - H_w)}\frac{d(H_c - H_w)}{dx}\right] =$$

$$C_H + \frac{j_{xc}E_x + j_{yc}E_y}{\rho_c u_c (H_c - H_w)}(\delta^*_{JE} - \delta^*) \tag{10}$$

where,

$$C_f = \left(\frac{\tau_w}{\frac{1}{2}\rho_c u_c^2}\right)$$

is the skin friction coefficient,

$$C_H = -\frac{\dot{q}_w}{\rho_c u_c (H_c - H_w)}$$

the Stanton number,

$$\theta = \int_0^\delta \left(1 - \frac{u}{u_c}\right)\frac{\rho u}{\rho_c u_c}\,dz$$

the momentum thickness,

$$\delta^* = \int_0^\delta \left(1 - \frac{\rho u}{\rho_c u_c}\right)dz$$

the displacement thickness,

$$\phi = \int_0^{\delta} \left(1 - \frac{H - H_w}{H_c - H_w}\right) \frac{\rho u}{\rho_c u_c} \, dz$$

the enthalpy deficit thickness,

$$\delta^*_{JB} = \int_0^{\delta_t} \left(1 - \frac{j_y}{j_{yc}}\right) dz$$

the current density displacement thickness, and

$$\delta^*_{JE} = \int_0^{\delta_t} \left(1 - \frac{j_x E_x + j_y E_y}{j_{xc} E_x + j_{yc} E_y}\right) dz \qquad (11)$$

the power density displacement thickness.

Equation (8) can be recognized as a form of the Von Karman integral momentum equation (Ref. 8) with an additional term representing the contribution to the momentum deficit thickness produced by the MHD body force. The current density displacement thickness parameter, δ^*_{JB}, represents the deficit in the current flux through the boundary layer compared to the current flux that would exist in an equivalent thickness of core flow. In this context, the term is analogous to the displacement thickness which represents the relative deficit of the mass flux through the boundary layer compared to the mass flux through an equivalent thickness of core flow.

Similarly, the Equation (10) is the energy integral where the last term represents the MHD effects. The parameter, δ^*_{JE}, corresponds to the MHD current displacement thickness parameter appearing in the momentum integral equation, and represents the relative deficit of the integrated power density in the boundary layer compared to the power density in an equivalent thickness of core flow.

Electrode Wall Boundary Layer

A similar integration of the momentum and energy equation for the electrode wall boundary layer leads to the Equations (12) and (13).

$$\frac{d\theta}{dx} + \theta\left[\frac{(\delta^*/\theta) + 2}{u_c}\frac{du_c}{dx} + \frac{1}{\rho_c}\frac{d\rho_c}{dx}\right] = \frac{C_f}{2} \qquad (12)$$

$$\frac{d\phi}{dx} + \phi\left[\frac{1}{\rho_c}\frac{d\rho_c}{dx} + \frac{1}{u_c}\frac{du_c}{dx} + \frac{1}{(H_c - H_w)}\frac{d(H_c - H_w)}{dx}\right] = C_H \qquad (13)$$

where,

$$\delta^* = \int_0^{\delta} \left(1 - \frac{\rho u}{\rho_c u_c}\right) dy$$

$$\theta = \int_0^{\delta} \left(1 - \frac{u}{u_c}\right) \frac{\rho u}{\rho_c u_c} \, dy$$

$$\phi = \int_0^{\delta} \left(1 - \frac{H - H_w}{H_c - H_w}\right) \frac{\rho u}{\rho_c u_c} \, dy \qquad (14)$$

The Equations (12) and (13) are similar to the B-wall integral Equations (8) and (10) with the exception that $\delta^*_{JB} = 0$ in the momentum integral Equation (12) and $\delta^*_{JE} = \delta^*$ in the energy integral Equation (13) as a result of the constraint of constant current through the E-wall layer.

Coupling

The coupling of the core flow equations and the boundary layer equations is achieved by defining an effective core area as

Core area = geometric area - area blocked by viscous effects
Area = width x height = ZY

$$\text{Core area} = A_c = (Z - 2\delta^*_B)(Y - \delta^*_A - \delta^*_C) \qquad (15)$$

where, δ^*_B - B-wall displacement thickness

δ^*_A - Anode wall displacement thickness

δ^*_C - Cathode wall displacement thickness

This method of coupling satisfies the continuity equation for the entire channel while accounting for the viscous effects through the boundary layer parameters. This coupling provides the primary feedback mechanism for adjusting the core flow solution by the boundary layer growth and for the boundary layer growth through the presence of certain core flow gradients in the boundary layer equations.

In the present procedure, the coupling is implemented numerically by first solving the core flow equations with the assumed boundary layer thickness. The best values correspond to the previous step values. Using the calculated core flow gradients, a first estimate of the boundary layer growth is obtained by integrating the boundary layer equations.

The change in core area is then calculated and compared with the initial guessed value. The procedure is repeated until a prescribed convergence is achieved.

Electromagnetic Field Relations

The applied magnetic field variation can be measured experimentally and therefore its specification is quite straightforward. The electric field components appearing in fluid conservation equations, neglecting the effects of pressure diffusion and electron inertia, are obtained from Ohm's law (Ref. 9) which can be expressed as:

$$j_x = \sigma_t \left[E_x - \beta(E_y - u_c B_z) \right] \tag{16}$$

$$j_y = \sigma_t \left[E_y - u_c B_z + \beta E_x \right] \tag{17}$$

The DCW generator may be connected either by discrete leads, as in Faraday generators, or by two-terminal connection, as in the case of Hall generators. With the assumption of infinitely fine segmented electrodes, the two-terminal connection implies a constant load current. The load current, I, flowing through the generator is given by the following expression:

$$I = \int_A \vec{j} \cdot d\vec{A} = A_{cs}(j_x + \phi j_y) = \text{const.} \tag{18}$$

with,
$$\phi = - \tan\theta = E_y/E_x \tag{19}$$

where A is the area of the plane which is slanted to the Y-Z plane by an angle θ and A_{cs} is the cross-sectional area at a given streamwise location.

By including an experimentally determined electrode drop, the simple theory predictions agree extremely well with the experiment (Ref. 10). Using Equations (16) to (19), the axial and transverse field relations can be written in the following form.

$$E_x = \frac{1}{(1 + \phi_w^2)} (u_c B_z - E_s) (\phi_w - \beta) - \frac{1}{\sigma_t} \frac{I_{xL}}{A_0} \tag{20}$$

$$E_y = (\phi_w E_x + E_s)$$

where,
$$\phi_w = - \text{Tan } \theta_w$$

$$\sigma_t = \frac{\sigma}{(1 + \beta^2)}$$

θ_w = Angle of inclination of the electrode frame

$E_s = V_s u_c B_z$ (electrode voltage drop)

$V_s = 0.25$

σ = Electrical conductivity

β = Hall parameter

B_z = Magnetic field strength

Here, u_c is the core flow velocity, B is the magnetic field strength, and σ and β are the electrical conductivity and Hall parameter, respectively. V_s is the non-dimensional electrode drop.

Relations for Skin Friction and Heat Transfer Coefficients

The specification of the friction coefficient for a smooth wall and the heat transfer coefficient are taken (Ref. 11) to be of the form

$$C_f = 0.0246 \left(\frac{\rho u \theta}{\mu}\right)^{-\frac{1}{4}}$$

$$C_H = \frac{(C_f/2)}{1 + 5\sqrt{\frac{C_f}{2}}\left[(Pr - 1) + \ell n \left(\frac{5Pr + 1}{6}\right)\right]} \qquad (21)$$

Since the appropriate empirical relations for turbulent compressible MHD flows are not available, the above relations are assumed to provide reasonable results. Also, in many practical applications of MHD channels, the wall temperature is maintained low enough by wall cooling. This will effectively reduce the electrical conductivity of the plasma near the wall with the result, the velocity and temperature profiles are predominately determined by ordinary gas dynamic turbulent phenomena.

Thermodynamic and Transport Property Data

The real gas effects are included in the channel flow calculations using a simple, second-degree surface-fitting interpolation procedure (Ref. 6). Using the AEDC COMB program, the equilibrium composition and thermodynamic properties of the mixture are determined for a specified pressure and temperature. The results of a series of such calculations have been incorporated into the procedure. Any of the required thermodynamic property is defined as a function of pressure and temperature by the following equation.

$$Zi = C_1T^2 + C_2pT^2 + C_3p^2T^2 + C_4T + C_5pT$$

$$+ C_6p^2T + C_7p^2 + C_8p + C_9 \qquad (22)$$

Using Equation (22) and the known values of the property and the coordinates (pressure and temperature) at nine points, nine simultaneous algebraic equations are formed in terms of the nine unknown coefficients, C_1 to C_9. The simultaneous equations are solved for the coefficients C_1 to C_9 by Gauss-Jordon complete elimination method using the maximum pivot strategy. Then, the required derivatives such as $\partial\rho/\partial p$ and $\partial\rho/\partial T$ are determined using the following analytical expressions.

$$\left.\frac{\partial\rho}{\partial T}\right|_p = 2(C_1T + C_2pT + C_3p^2T) + C_4 + C_5p + C_6p^2 \qquad (23)$$

and,
$$\left.\frac{\partial\rho}{\partial p}\right|_T = C_2T^2 + 2C_3pT^2 + C_5T + 2C_6pT + 2C_7p + C_8 \qquad (24)$$

where, p is in N/m^2 and T is in degrees K.

Also, when the temperature needs to be computed for given pressure and enthalpy, the following equation is used.

$$T = C_1h^2 + C_2ph^2 + C_3p^2h^2 + C_4h + C_5ph + C_6p^2h + C_7p^2 + C_8p + C_9 \qquad (25)$$

The coefficients C_1 to C_9 in the above equation are determined as described above. Since all of the thermodynamic properties vary slowly with pressure and temperature, it is possible to fit the data on a second-degree surface for a wide range of pressures and temperatures[6].

However, in the present MHD channel performance calculations, the transport properties are evaluated using the following emperical relations.

Electrical conductivity: $\sigma = \sigma_0\left(\frac{T}{T_0}\right)^{19.525}\left(\frac{p_c}{p}\right)^{-1.27}$ (26) (Ref. 12)

Hall parameter: $\beta = \beta_0\left(\frac{B_z}{B_0}\right)\left(\frac{\rho_0}{\rho}\right)^{-0.8323}\left(\frac{T}{2719}\right)^{-1.943}$ (27) (Ref. 12)

Viscosity: $\eta = \eta_0 T^m$ (28) (Ref. 13)

Prandtl number: $Pr = \frac{\gamma(p,T)}{1.94\gamma(p,T) - 0.74}$ (29) (Ref. 14)

where, $\sigma_0 = 13.19$ mhos/meter

$\beta_0 = 1.755$

$B_0 = B_{max}$, Tesla

$m = 0.771$

$\eta_0 = 1.919 \times 10^{-7}$ kg/ms

$T_0 = 2766°K$

$p_0 = 1.3 \times 10^5$ N/m^2

and, $\rho_0 = 0.1444$ kg/m^3

Boundary Layer Profiles

The accuracy of the momentum integral technique depends upon the choice of boundary layer profiles chosen. In the absence of reliable data for MHD conditons, one-seventh power law profiles are assumed.

$$\left(\frac{u}{u_c}\right) = \left(\frac{z}{\delta}\right)^{1/7} = \left(\frac{y}{\delta}\right)^{1/7} \quad (30)$$

$$\left(\frac{H - H_w}{H_c - H_w}\right) = \left(\frac{z}{\delta}\right)^{1/7} = \left(\frac{y}{\delta}\right)^{1/7} \quad (31)$$

Performance Parameters

The following performance parameters are obtained using Simpson's 1/3-rule of integration.

a. Integrated axial voltage

$$V_x = -\int_0^L E_x dx \quad (32)$$

b. Integrated transverse current

$$I_y = \int_0^L \int_{-\frac{Z}{2}}^{\frac{Z}{2}} (j_x E_x + j_y E_y)\, dz dx \tag{33}$$

c. Integrated power

$$p = \int_0^L \int_{-\frac{Z}{2}}^{\frac{Z}{2}} (j_x E_x + j_y E_y)\, dz dx \tag{34}$$

d. Wall heat transfer rate

$$\dot{Q}_w = \int_0^L \dot{q}_w\, Y\, dx + \int_0^L \dot{q}_w\, Z\, dx \tag{35}$$

5.3 Solution Procedure

With the specified initial and boundary conditions and assumed boundary layer thickness, first the core flow equations are solved. Then, a first estimate of the boundary layer growth is obtained by integrating the boundary layer equations. The change in core area can then be calculated and compared with the initial guess. Iterations are made to obtain a converged solution.

The magnetic field is taken to be normal to the X-Y plane, and assumed to be uniform at any X-constant plane in accordance with the simplifying assumption of one-dimensional analysis. The variation of magnetic field strength along the channel axis is taken as shown in Fig. 34. The electrical calculation is done by assuming infinite segmentation and solving Ohm's law in the three regions, core, electrode wall boundary layer, and insulator wall boundary layer, and coupling them to the proper connection such as diagonal, Faraday, etc., equations.

The integration of the core flow and boundary layer equations is accomplished by a fourth-order Runge-Kutta algorithm. The method is quite rapid, even when employing the interpolation for the real gas thermodynamic and transport property data. Typical run times are of the order of 30 to 40 seconds, thus making the program convenient for making parametric studies with a large number of design variables.

5.4 Results and Discussions

The channel geometry along with the design parameters is shown in Fig. 35. The channel measures 9 cm by 9 cm at the inlet and 9 cm by 17 cm at the exit. There are 130 diagonal frames with 37° angle of inclination to the normal. The channel is connected to a single load.

Two sets of calculations were performed for the channel: one with the assumption of perfect gas, and the other using the real gas properties. Figures 36 through 39 provide complete description of the fluid dynamic and electrodynamic characteristics of the channel for the case of perfect gas assumption. Figures 40 through 46 provide the channel performance predictions using the real gas properties. Figure 36 shows the predicted variation of velocity, pressure,

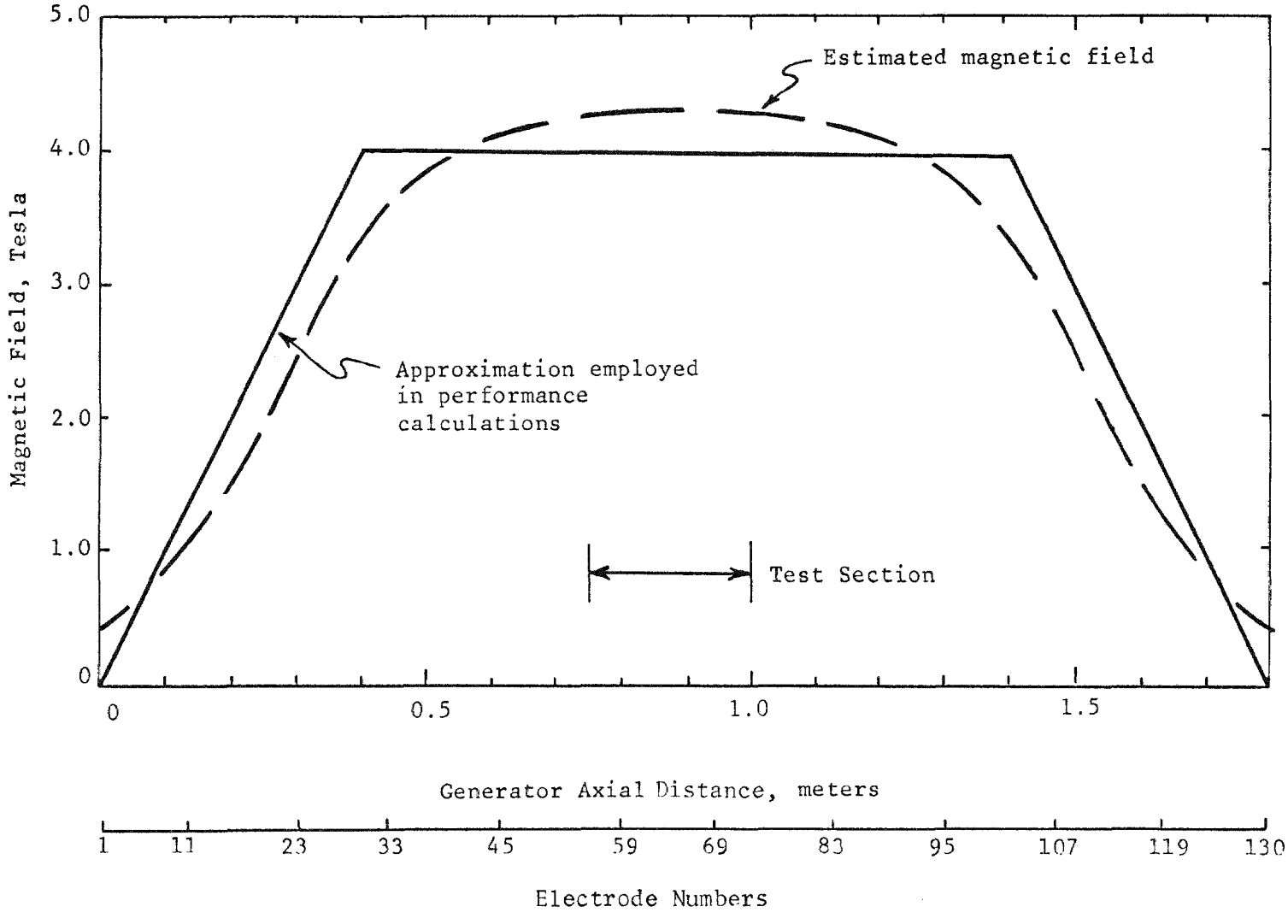

Fig. 34 Variation ot Magnetic Field Along the Channel

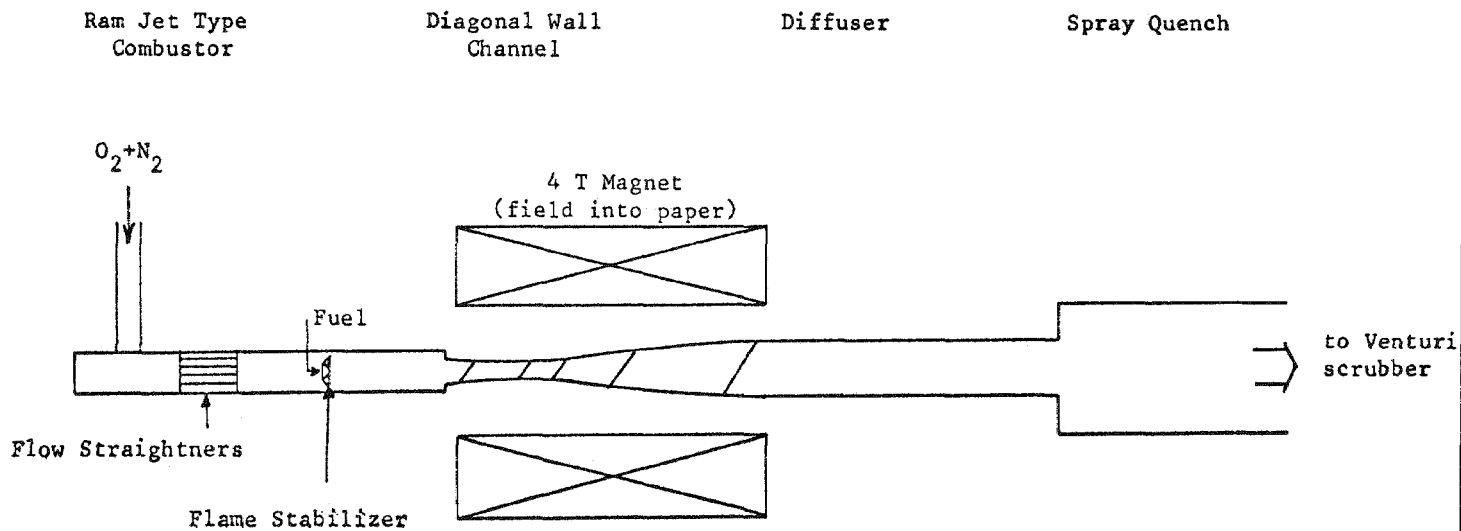

Combustor Design Parameters	
Total flow rate	1.1 kgm/sec
O_2 flow rate	0.5 kgm/sec
N_2/O_2	~ 1.0 by volume
Fuel flow	0.148 kgm/sec
Percent seed	1.5%

Channel Design Parameters	
Inlet dimensions	9 x 9 cm (3.5 x 3.5 in)
Exit dimensions	9 x 17.1 cm (3.5 x 6.74 in)
Area ratio	1.92
Length	1.79 m
No. of segments	130
Segment angle	37°
End to end voltage	1532 volts
Current	93 amps
Power	143 kw

Fig. 35 Schematic of MHD Generator System

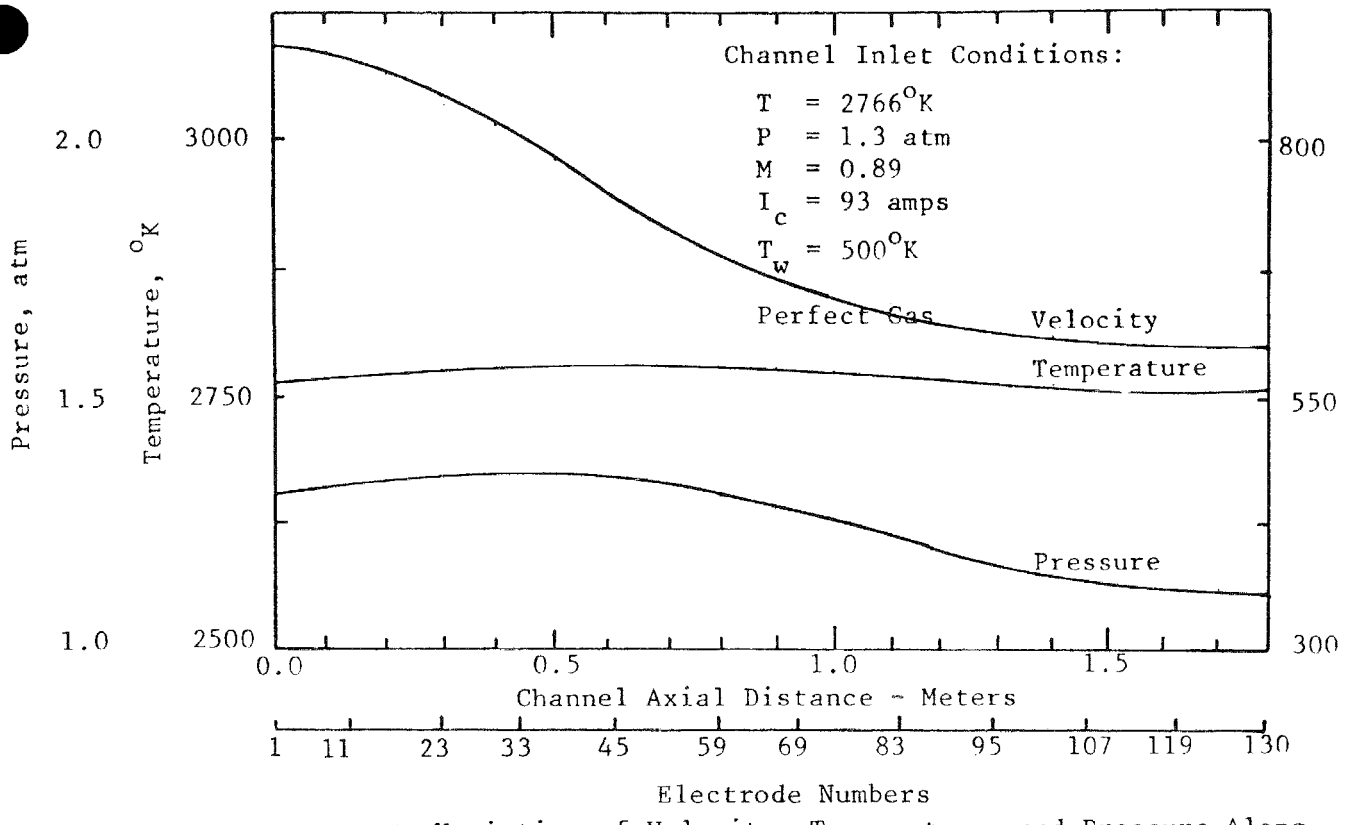

Fig. 36 Variation of Velocity, Temperature, and Pressure Along the Channel

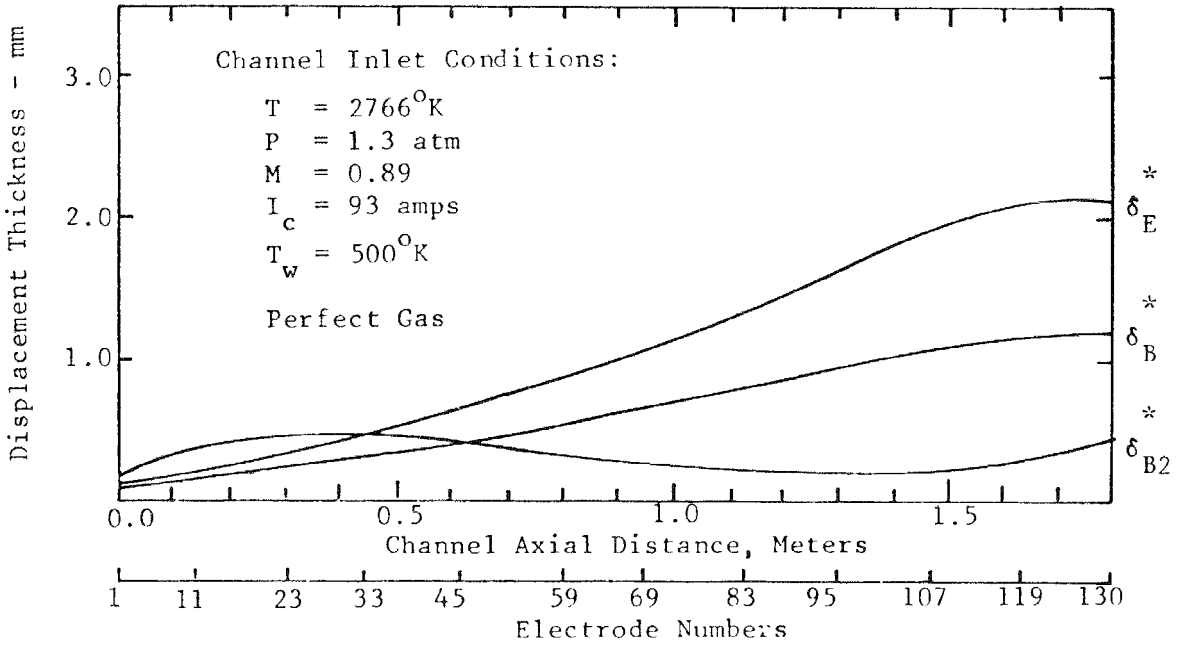

Fig. 37 Boundary Layer Displacement Thickness Distribution Along the Channel

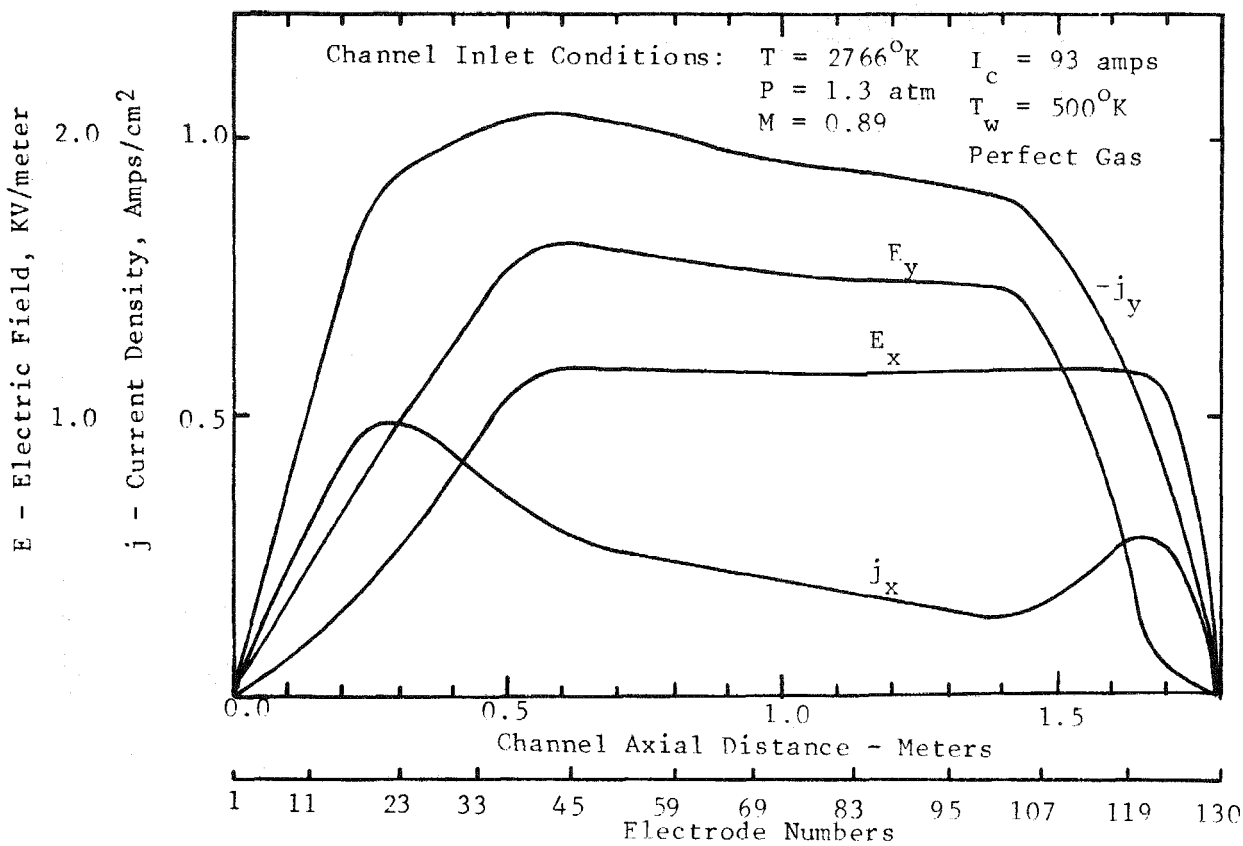

Fig. 38 Variation of Electrical Parameters Along the Channel

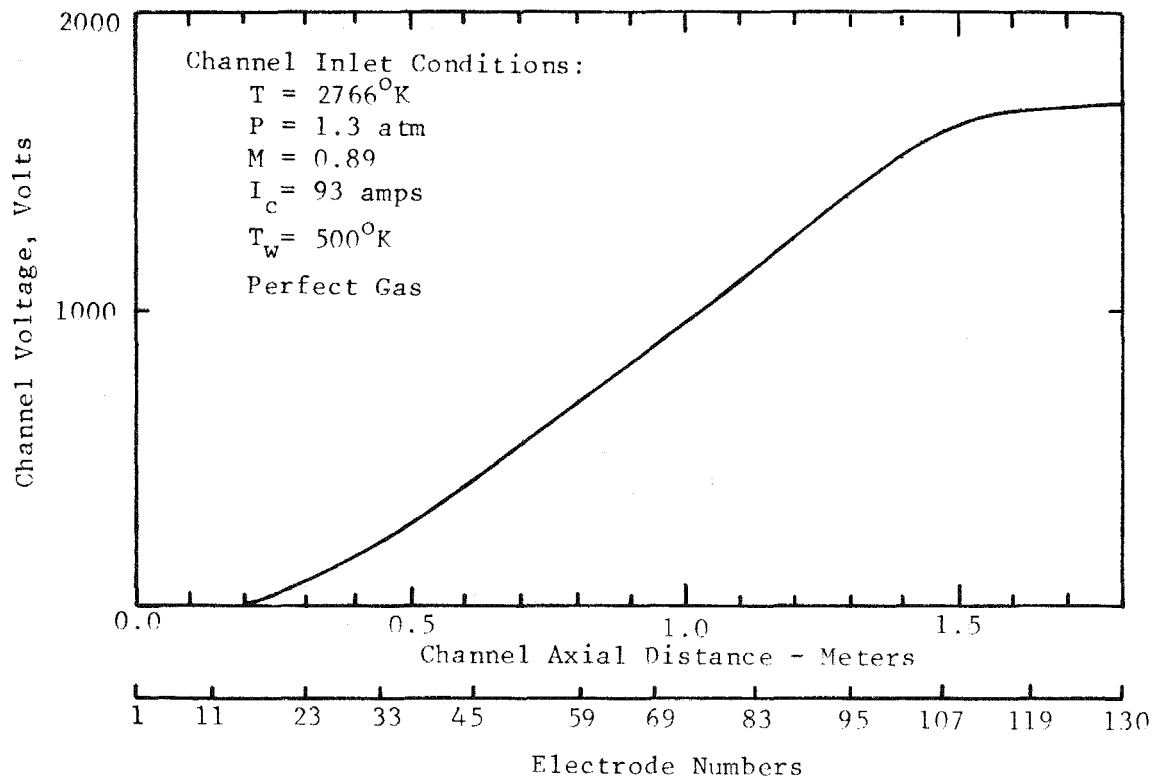

Fig. 39 Voltage Distribution Along the Channel

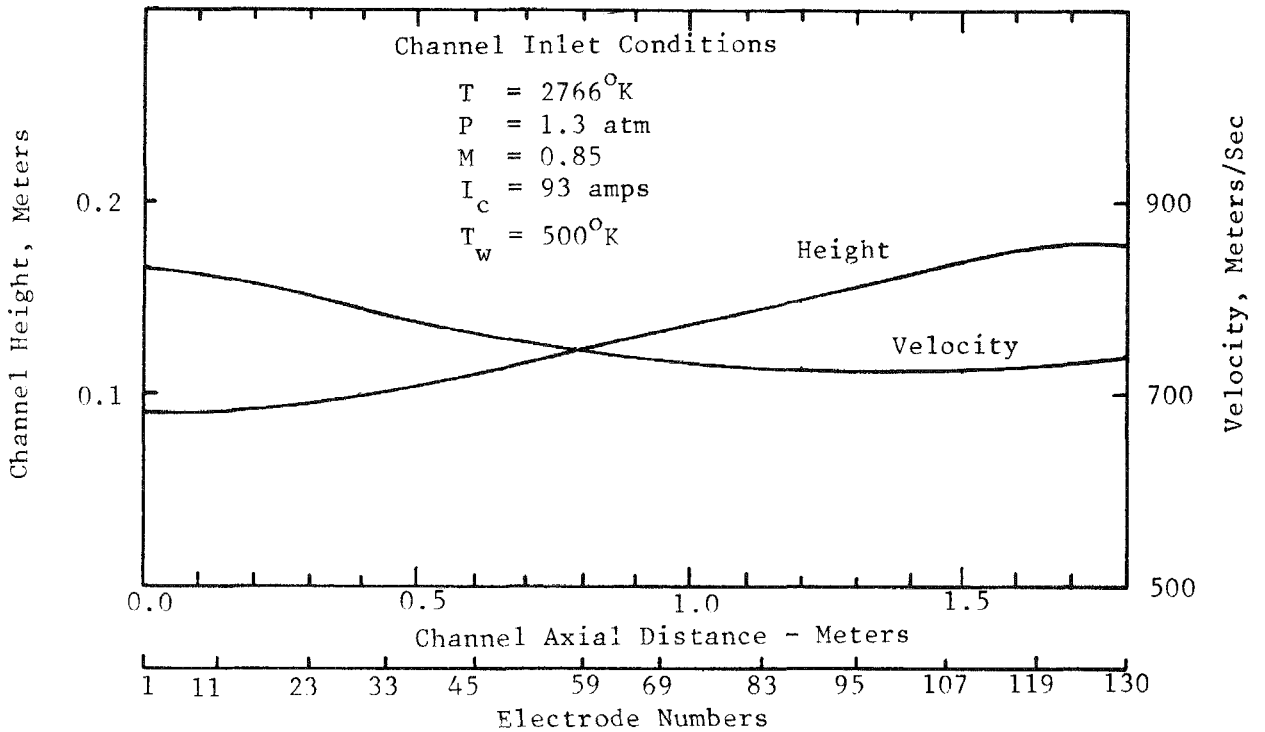

Fig. 40 Variation of Channel Height and Flow Velocity Along the Channel

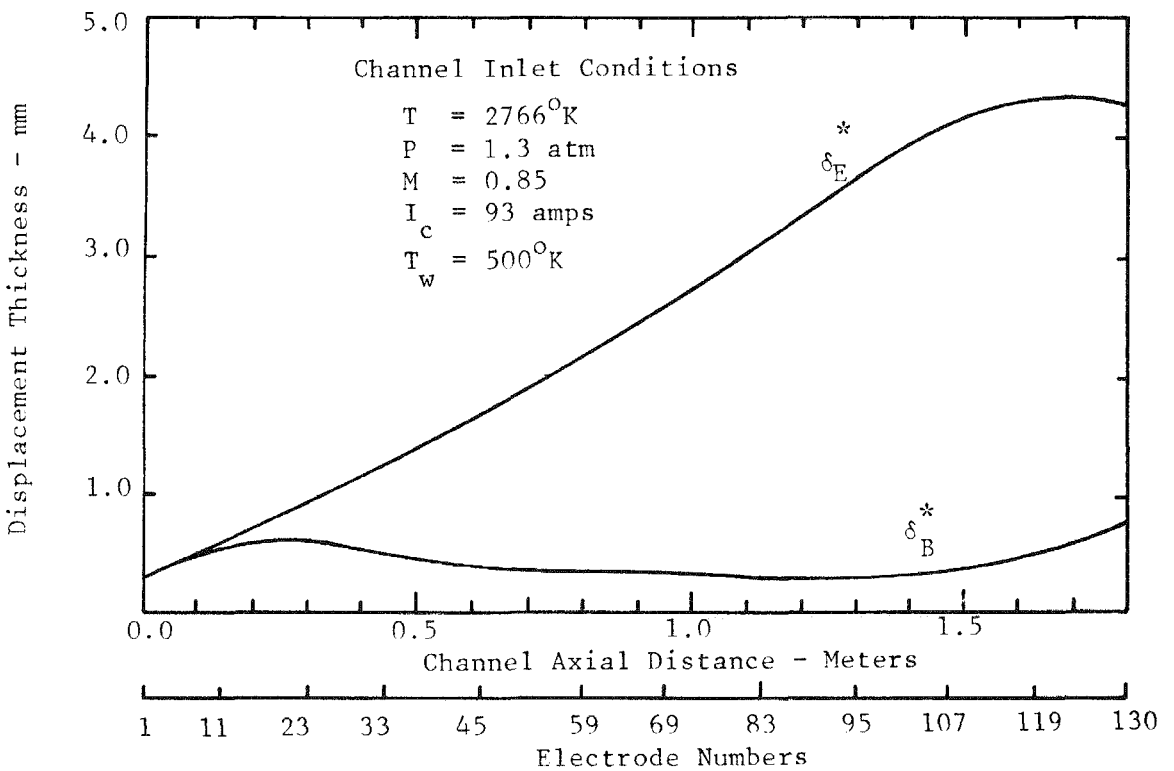

Fig. 41 Growth of Boundary Layer Displacement Thickness Along the Channel

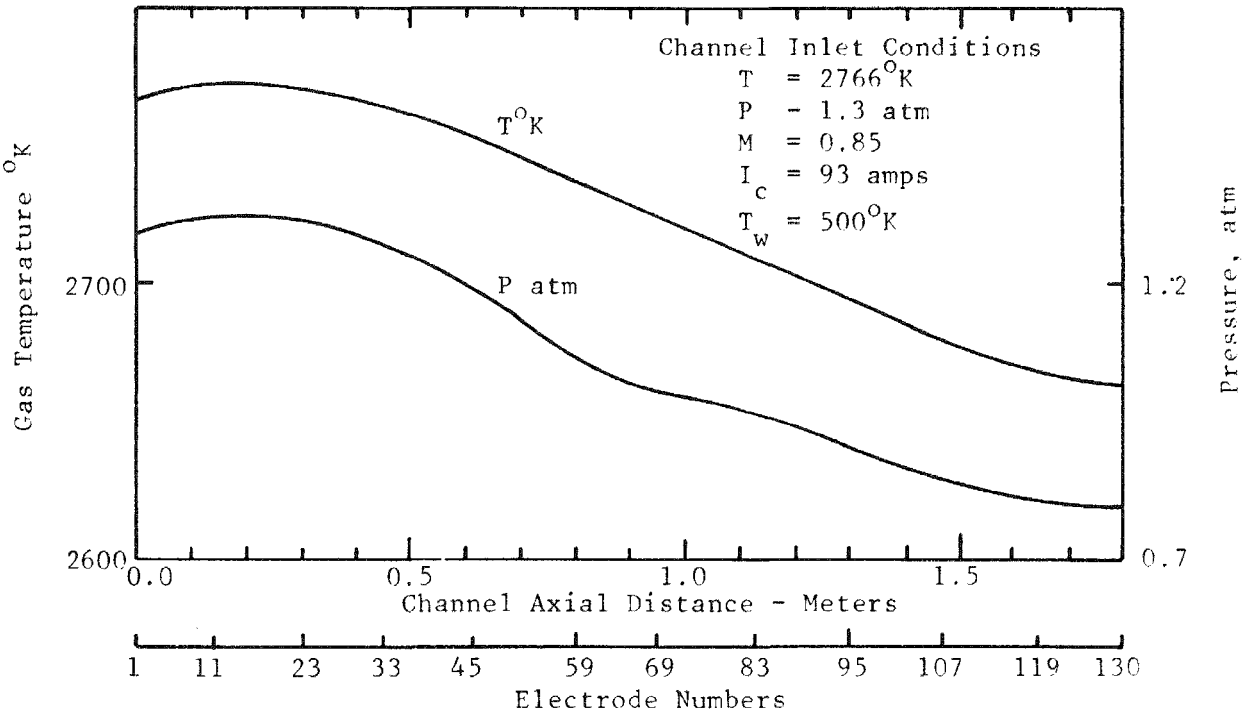

Fig. 42 Temperature and Pressure Distribution in the Channel

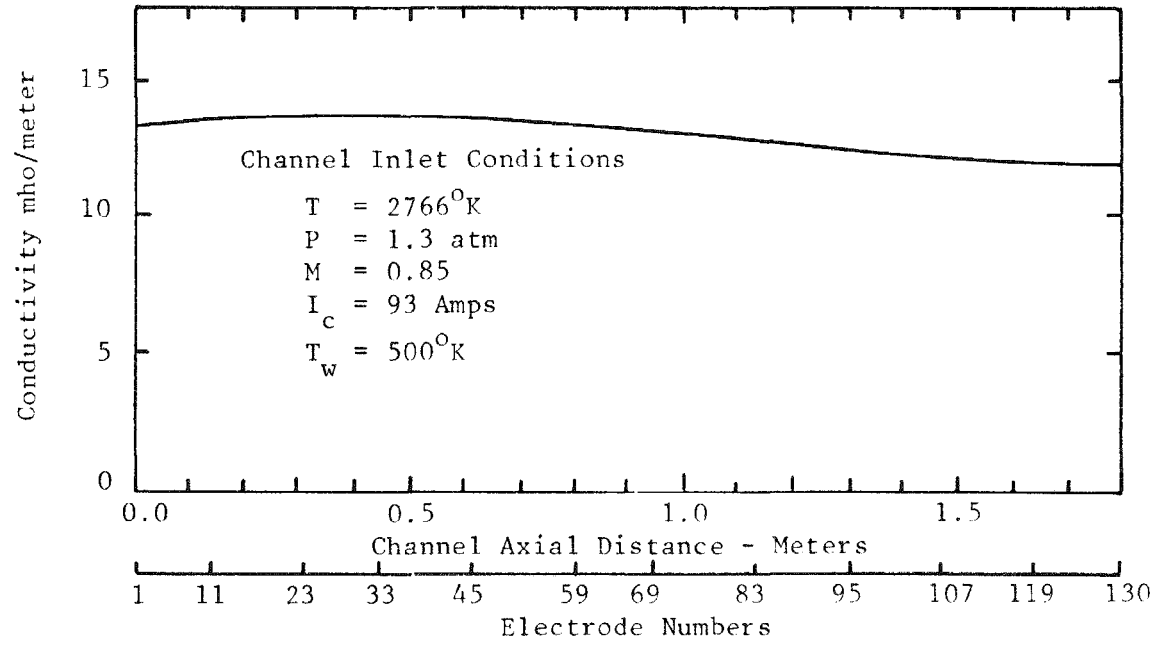

Fig. 43 Variation of Electrical Conductivity Along the Channel

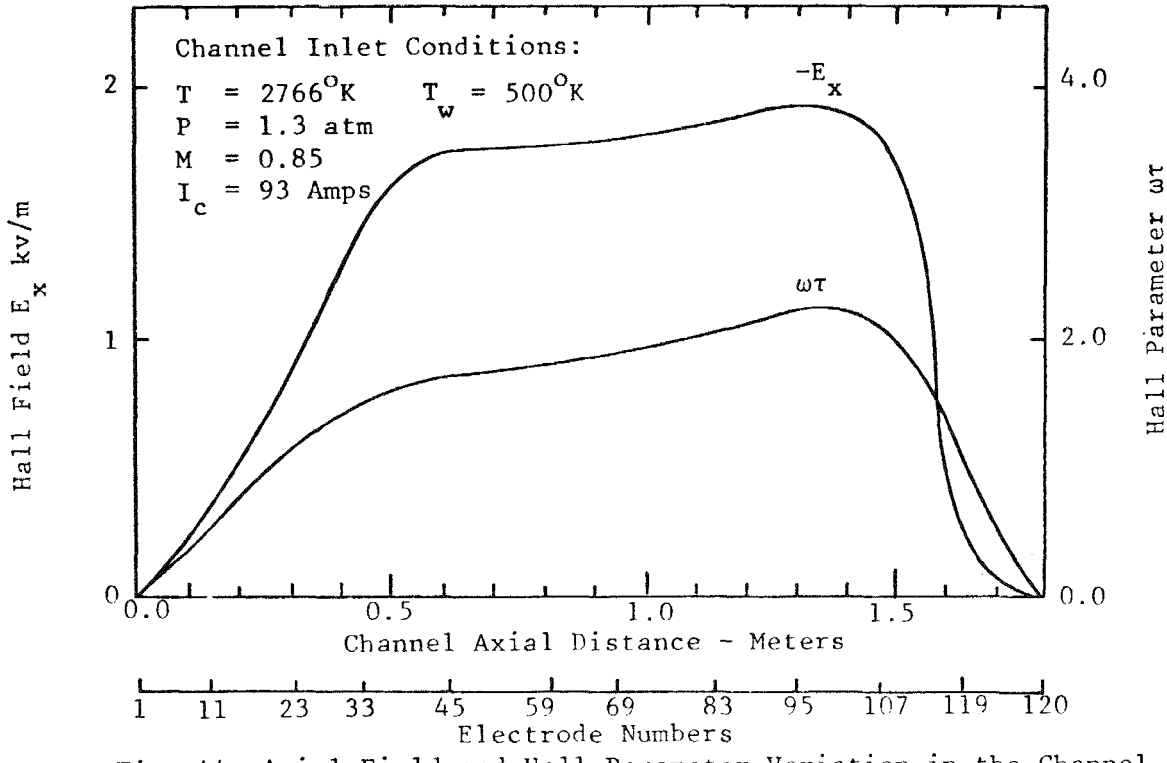

Fig. 44 Axial Field and Hall Parameter Variation in the Channel

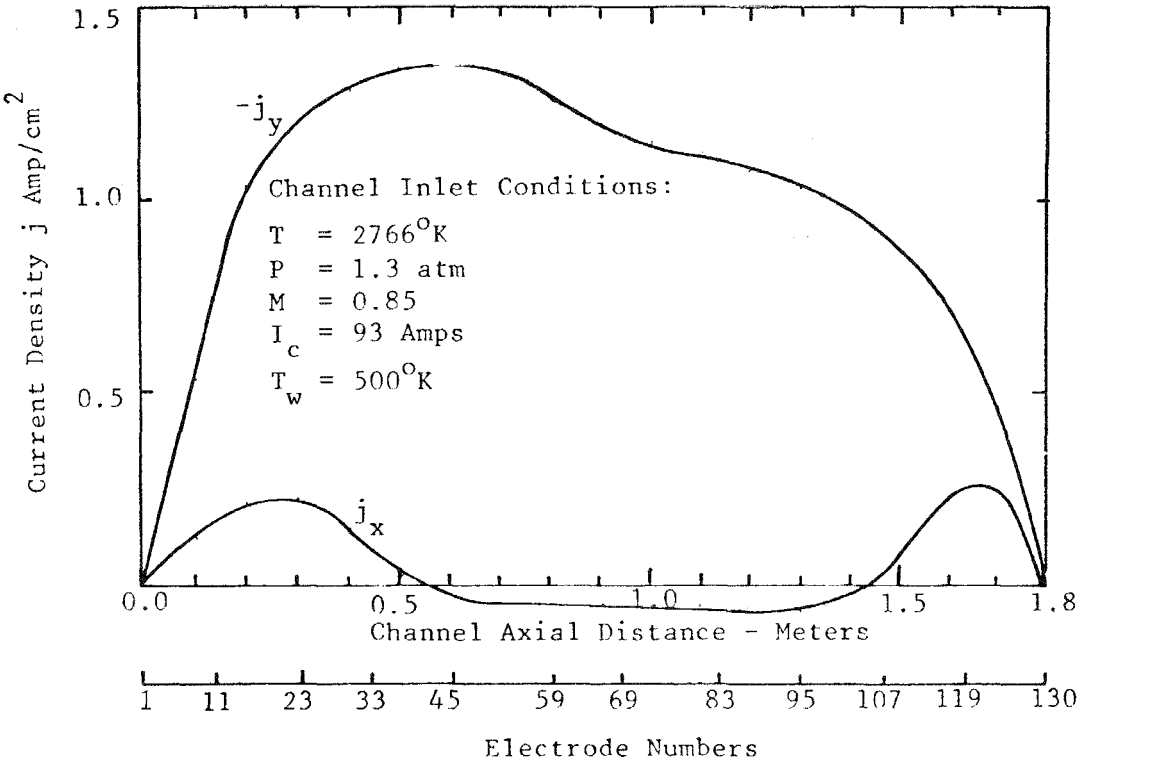

Fig. 45 Axial and Transverse Current Density Distribution in the Channel

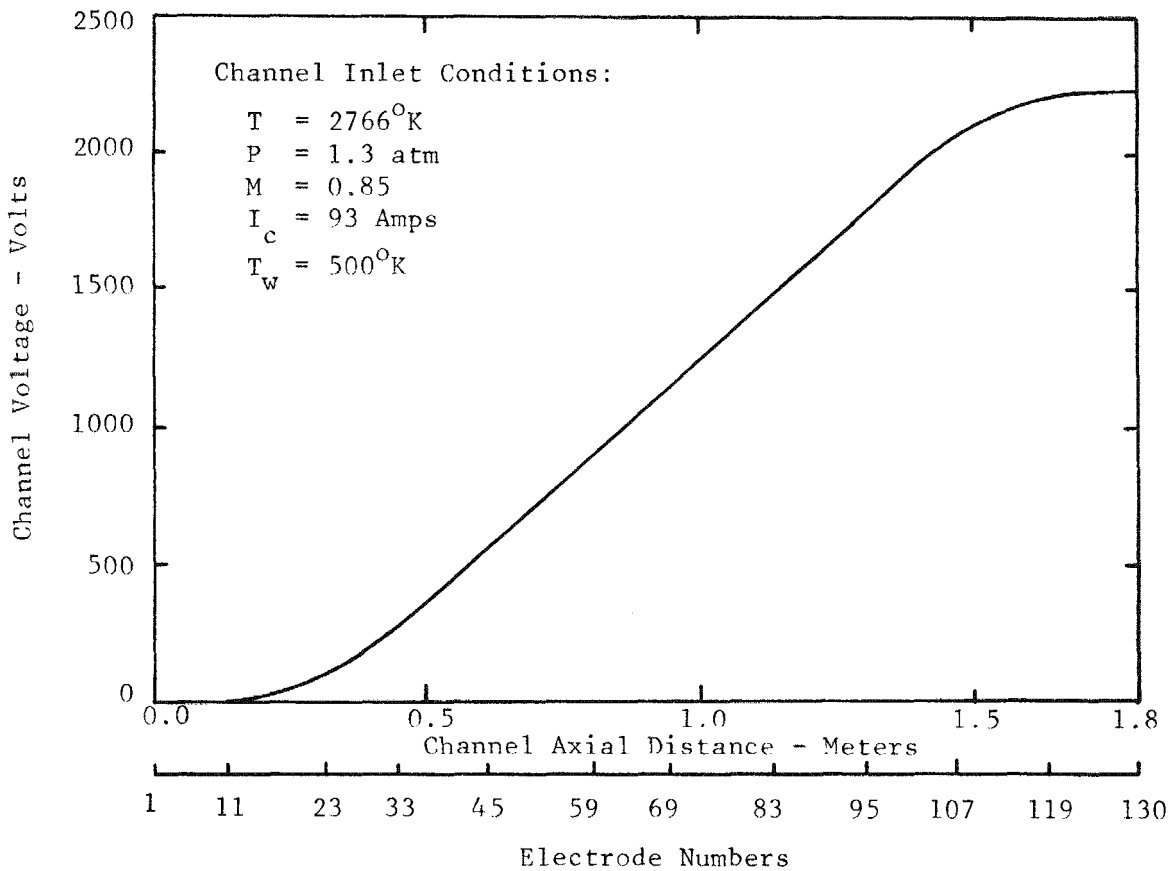

Fig. 46 Voltage Distribution in the Channel

and temperature. The flow decelerates as it flows through the MHD channel. With such a decelerating flow, the conversion of kinetic energy to electric power improves, but it may promote flow separation. In Fig. 37, the variation of displacement thickness, δ^*, along the channel is shown for both the electrode wall (δ^*_E) and the insulator wall (δ^*_B). Also shown in the figure is the effect of considering the current density non-uniformity term on the growth of the displacement thickness (δ^*_{B2}) for the insulator wall along the channel.

Figure 38 presents the calculated distribution of the electric field components along the channel. The electrode voltage drop is taken proportional to the induced field (uB). The maximum axial field is about 1.0 kv/meter and the maximum transverse current density is 1.0 amp/cm^2. It is generally accepted from experimental observations that at current densities higher than 1.0 amp/cm^2, arcing and severe erosion problems may occur. Finally, the resulting voltage distribution is shown in Fig. 39 which shows a terminal voltage of 1720 volts. Similarly, the results obtained for the channel using the real gas properties are shown in Figs. 40 through 46. Figures 40 through 42 describe the fluid dyanmic characteristics of the channel. As in the perfect gas case, the flow decelerates in the channel. The results show that the pressure as well as the temperature decrease in the channel. In Fig. 43, the variation of electrical conductivity along the axis of the channel is shown. The conductivity value remains almost constant. Its value is calculated using Equation (26).

The variation of the Hall field and the Hall parameter is shown in Fig. 44. The maximum value of the Hall field obtained is 2.0 kv/m and the Hall parameter is about 2.0. Figure 45 shows the distribution of the axial and transverse current densities along the channel. The maximum value of current density calculated is about 1.4 amp/cm^2 which is much higher than the design value of 1.0 amp/cm^2. Finally, in Fig. 46, the voltage distribution is shown indicating a terminal voltage of 2250 volts.

.0 REFERENCES

1. Dooley, M. T., "Gaseous Electrode for MHD Generator," U. S. Patent Application Serial No. 643,946, Dec. 24, 1975; U. S. Patent No. 3,927,337, Dec. 16, 1975; and U. S. Patent No. 3,940,641, Feb. 24, 1976.

2. Scannell, E. P., et al., "Gaseous Electrode Development at RMC," *Proc. of the 16th Symp. on Eng. Aspects of MHD*, U. Pittsburgh, Pittsburgh, Penn., 1977.

3. Petrick, M. and Shumyatsky, B. Y., *Open-Cycle Magnetohydrodynamic Electrical Power Generation*, A Joint U.S.-U.S.S.R. Publication, ANL, Illinois, 1978.

4. Fushimi, K., et al., "Development of a Long Duration MHD Channel," Vol. I, *Open Cycle MHD Systems, Fifth International Conference on MHD Electrical Power Generation*, 1971, pp. 371-392.

5. Sutton, G. W. and Sherman, A., *Engineering Magnetohydrodynamics*, McGraw-Hill Book Company, New York, 1965.

6. Sathyanarayana, K., "Calculation of Real Gas Properties," Reynolds Metals Co., Energy Conversion Division Technical Note No. 006-78, 1978.

7. Wilson, D. R., "Analysis of MHD Channel Flows by a Coupled Core Flow-Boundary Layer Model," Ph.D. Dissertation, The University of Texas at Arlington, 1973.

8. Schlichting, Herman, *Boundary Layer Theory*, 6th Ed., McGraw-Hill Book Co., New York, 1968.

9. Rosa, Richard J., *Magnetohydrodynamic Energy Conversion*, McGraw-Hill Book Co., New York, 1968.

10. Dicks, J. R., et al., "Characteristics of a Family of Diagonal Conducting Wall MHD Generators," *Proc. of 8th Symp. on Eng. Aspects of MHD*, p. 46, 1967.

11. Elliot, D. G., Bartz, D. R., and Silver, S., "Calculation of Turbulent Boundary Layer Growth and Heat Transfer in Axi-Symmetric Nozzles," JPL TR 32-387, 1963.

12. Cott, D. W., Private communication.

13. Raedor, J. (ed.), *MHD Power Generation*, Springer-Verlag, New York, 1975.

14. Heywood, J. B. and Womack, G. J., *Open-Cycle MHD Power Generation*, Pergamon Press, 1969.

APPENDIX A

MEASUREMENT OF THE ARC GASEOUS ELECTRODE GAS TEMPERATURE WITH A CALPROBE

R. Mallavarpu

INTRODUCTION

The Calprobe is a water-cooled gas sampling probe that is capable of steady state operation in a gas at 15,000°K and one atmosphere pressure. It directly measures the local gas enthalpy from which the gas temperature may be estimated. These characteristics of the probe make it especially suitable for determining the properties of the effluent gas from the arc gaseous electrode. In addition, this probe can also be used as an electrostatic (Langmuir) probe to determine the electron temperature and the density, n_e, of the ionized species.

EXPERIMENTAL SETUP AND MEASUREMENT TECHNIQUE

The gas temperature measurement was conducted on the arc gaseous electrode in the Electrode Development Facility. The probe was mounted on a stand which enables a precise variation of its position in any of the three directions x, y, z (Fig. A.1). This feature allows probe measurements to be made as a function of penetration into the arc plasma (along z) and axial location (along y).

Operation of the calorimetric probe is fairly straightforward and utilizes what is known as a "tare" measurement. A sample of the gas to be measured is continuously aspirated through the central channel of the inner cooling jacket assembly (Fig. A.2). Measurements are made of the coolant temperature rise, flow rate, steady gas sample temperature and pressure at the probe exit and steady gas sample flow rate which is measured by a calibrated sonic orifice incorporated as part of the probe. A valve in the gas sample line is closed and observations of coolant temperature rise and flow rate are made. The rate of heat removal from the gas sample is then easily evaluated from the difference between the two water coolant rates as follows:

$$h_{T_{g1}} = C_{p_{g1}} T_{g1} = \frac{\dot{w}_c}{\dot{w}_g} C_{p_c} \left[(\Delta T_c)_F - (\Delta T_c)_{Tare} \right] + C_{p_{g2}} T_{g2}$$

where,

$h_{T_{g1}}$ = Specific total enthalpy of free-stream gas at probe entrance

$C_{p_{g1}}$ = Specific heat of gas sample at unknown gas temperature, T_{g1}

$C_{p_{g2}}$ = Specific heat of gas sample at measured temperature, T_{g2} at probe exit

C_{p_c} = Specific heat of coolant water

T_{g1} = Unknown gas temperature at probe entrance

T_{g2} = Measured temperature of gas sample at probe exit

$(\Delta T_c)_F$ = Coolant temperature rise with sample gas shut-off valve open

$(\Delta T_c)_{Tare}$ = Coolant temperature rise with shut-off valve closed

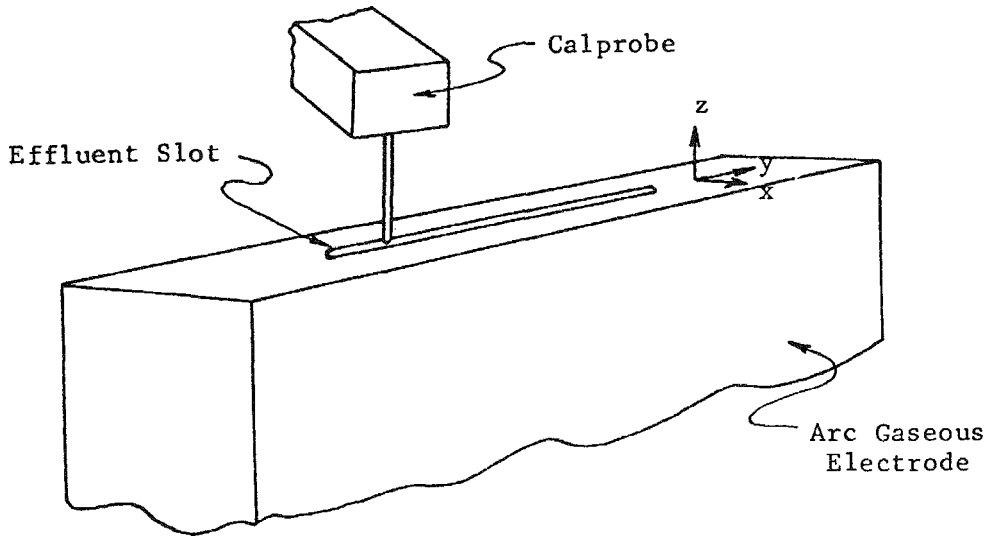

Fig. A.1 Schematic of Calprobe Application for the Gaseous Electrode

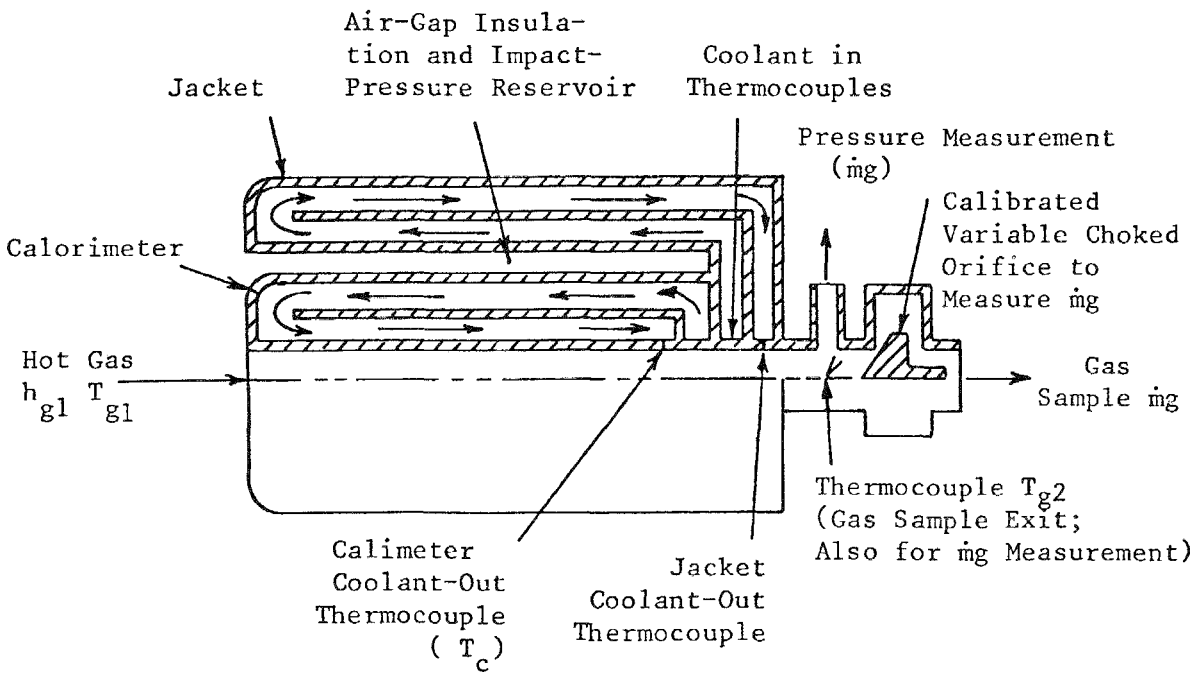

Fig. A.2 Schematic of Calprobe Jacketed Calorimetric Probe

$\dot{w}_g$ = Measured weight flow rate of gas sample

$\dot{w}_c$ = Measured coolant water flow rate.

In one experiment to date that has been performed using the Calprobe (June 1, 1979), the probe was located at y = 1.6 cm from A and the probe tip was in the same plane as the slot face (Fig. A.1). It was believed this location would yield a representative value of the arc gas temperature. The experiment was conducted for a constant applied magnetic field, a constant argon flow rate, and for arc currents in the range 50 - 80 A. The pertinent recorded data and the calculated values of local enthalpy and gas temperature are shown in Table A.1.

A study of the results shows that the estimated gas temperature is around 10,000°K and shows little variation with arc current in the range 50 A - 82 A. This is in contradiction to experiments with plasma jets where the enthalpy (and hence temperature) increases with current when the gas mass flow is held constant.

Since a limited set of data has been recorded, the measured gas temperature should be taken as being representative of the order of magnitude of the gas temperature. Further refinement of the experimental data could be obtained by recalibrating the measurements of gas, coolant flow rates, and the various pressure and temperature measuring devices involved.

REFERENCES

1. Grey, J., Jacobs, P. F., and Sherman, M. P., *Rev. Sci. Inst.*, 33 (7), 738 1962.

2. Grey, J. and Jacobs, P. F., *AIAA Journal*, 5 (1), 84, 1967.

TABLE A.1

CALPROBE ENTHALPY TEST

Cathode: 0.025 in O.D. Copper, Thick Walled
Yaw Angle: 60°
Applied Magnetic Field: 1 Tesla
Gas: Argon
Flow Rate: 35 SCFH

Arc Current I, A	Coolant Flow Rate $\dot{w}_c$, Kg/s x 10^3	Gas Flow Rate $\dot{w}_g$, Kg/s x 10^6	Coolant Temperature Rise $(\Delta T_c)_F$, °K	$(\Delta T_c)_{Tare}$, °K	Gas Temp. at Exit T_{g2}, °K	Calculated Gas Enthalpy h_{Tg1}, $\frac{KJ}{Kg} \times 10^{-3}$	Estimated Gas Temp. T_{g1}, °K
50	1.7663	1.9605	2.7	1.8	305.26	3.555	10,210
59	1.7663	1.9000	3.3	2.0	311.86	5.223	10,715
72	1.7663	1.9431	3.2	2.3	310.76	3.588	10,221
82	1.7663	1.930	2.6	2.2	312.06	1.696	9,305

APPENDIX B

ANALYSIS OF ARC GASEOUS ELECTRODE PLASMA GENERATION

V. Thiagarajan

INTRODUCTION

The purpose of the gaseous electrode is to generate and maintain a supply of hot gas near the electrode walls of electrical conductivity equal to or higher than that of the gas in the core flow of MHD power generating channels. The main advantage of such electrodes is that they may reduce current concentrations by providing paths of lower impedance for charge transport. Consequently, the wear on the electrodes is reduced and the electrode life increased making them suitable for base load MHD power generators.

A schematic of such an electrode is shown in Fig. B.1. An inert gas, say argon, is injected tangentially into a concentric cylindrical annulus, wherein an arc is struck. The electrode is positioned at an angle, ϕ (the 'yaw' angle) to the magnetic field. The Lorentz force on the arc will have components parallel to the axis of the annulus and perpendicular in the azimuthal direction. Hence, the arc will rotate and translate within the annulus heating the surrounding cold gas resulting in a hot plume of gas being ejected into the MHD channel through the slot C-D. The object is to analyze the mechanics and the energetics of the arc in the annulus and to formulate a model to predict the velocity and temperature profiles along the slot C-D.

MECHANICS OF THE ARC

The coordinate system is shown in Fig. B.1. The axis of the electrode is along the x direction. In general, the charge transport will not be purely in the radial direction. Let the magnetic field in a plane perpendicular to the direction of the current be B and let its radial and longitudinal components be B SIN ϕ and B COS ϕ, respectively. As already observed, the arc of mass, m (whose boundaries are not known), translates along x with a frequency f_t and rotates along θ with a frequency f_θ, under the influence of the Lorentz force. The arc rotates with an angular velocity, ω_A (with $\omega_A = 2\pi f_\theta$), and the cold gas swirls with an angular velocity, ω_g, inside the annulus. The following momentum balance equations may be written down for the arc of mass, m, and volume, V_A.

Momentum balance, x direction:

$$V_A \rho_A (T_A) \frac{du}{dt} = \ell I_A B \cos(\phi) - \tfrac{1}{2} C_D \rho_g u^2 A \qquad (1)$$

where, ρ_A = Density of the arc at its temperature, T_A

$\rho_A V_A$ = Mass, m, of the arc

u = Velocity of the arc in the x direction

t = Time

ℓ = Radial interelectrode space

B = Magnetic field (perpendicular to the arc current)

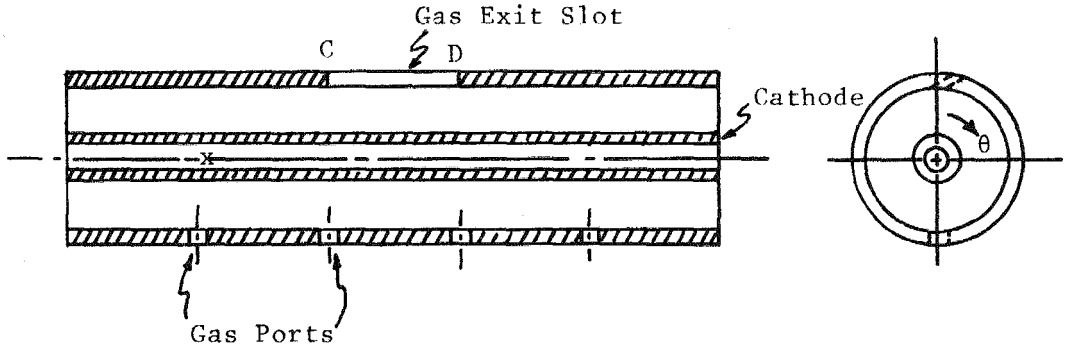

Fig. B.1 Schematic of the Gaseous Electrode

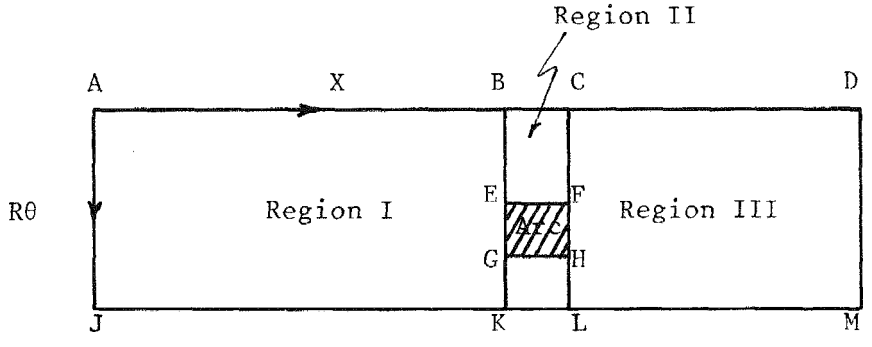

Fig. B.2 Development of the Annulus of the Gaseous Electrode

I_A = Total arc current

C_D = Coefficient of drag

ρ_g = Density of the gas at its temperature, T_g,

A = Projected area of the arc along the x direction.

The arc may be assumed to be a cylindrical spoke of diameter 'd' and length 'ℓ'. Then,

$$\text{the volume of the arc } V_A = \frac{\pi d^2 \ell}{4} \tag{2}$$

and,

$$\text{the projected area } A = d\ell = \left(\frac{4}{\pi} V_A \ell\right)^{\frac{1}{2}} \tag{3}$$

Equation (1) can be rewritten as follows:

$$V_A \rho_A \frac{du}{dt} = \ell I_A B \cos(\phi) - \tfrac{1}{2} C_D \rho_g \left(\frac{4}{\pi} V_A \ell\right)^{\frac{1}{2}} u^2 \tag{4}$$

Momentum balance, θ direction:

$$V_A \rho_A R \frac{d\theta}{dt} = \ell I_A B \sin(\phi) - \tfrac{1}{2} C_D \rho_g (\omega_A - \omega_g)^2 R^2 A =$$

$$\ell I_A B \sin(\phi) - \tfrac{1}{2} C_D \rho_g (\omega_A - \omega_g)^2 R^2 \left(\frac{4}{\pi} V_A \ell\right)^{\frac{1}{2}} \tag{5}$$

where, R is the mean arc radius.

Determination of the Arc Volume

The inertial forces in the x and θ directions may be neglected initially and may be included after trial calculations if they happen to be considerable. The angle, ϕ, may be eliminated between Equations (4) and (5) to obtain the following expression for the arc volume:

$$V_A = \frac{\pi (\ell I_A B)^2}{(C_D \rho_g)^2 \left[(\omega_A - \omega_g)^4 R^4 + (L f_t)^4\right]} \tag{6}$$

where, u has been replaced by $(L f_t)$, L being the length of the electrode.

Sample Calculations with Typical Numbers

Flow rate of argon = 30 Scft/hr
Diameter of inlet holes for argon (15 Nos.) = 0.07"
Swirl velocity of gas ≃ 21 ft/sec
Mean radius of the annulus ≃ 0.004 m
Swirl angular velocity ≃ 1660 radians/sec

$\rho_g \simeq 1.66$ kg/m ; $C_D \simeq 1.0$; $B \simeq 1$ Tesla ;

$\ell \simeq 0.00.58$ m ; $I_A \simeq 50$ amps ; $L \simeq 0.1$;

$f_t = 300$ cps ; $u = L f_t = 30$ m/sec ; $\omega_A \simeq 2000$ Rps = 12600 radians/sec ;

and the volume, $V_A \simeq 1.57$ mm^3 .

The diameter, d, of the spoke is found to be approximately 1 mm. Further, the inertial forces are found to be negligible with these typical numbers.

ENERGETICS OF THE ARC

Characteristic Times

There are five characteristic times as regards the energy transport is concerned.

(1) $\tau_T = 1/f_T$: The time required for the arc to traverse the length of the gaseous electrode once.

(2) $\tau_\theta = 1/f$: The time required for one azimuthal rotation.

(3) τ_p : The time required by the plasma in the MHD channel to traverse the width of the slot.

(4) τ_g : The time reqired for the cold inert gas to traverse the annulus and enter the MHD channel.

(5) τ_d : The time required for the energy in the arc to diffuse by conduction through a distance, y, and is given by the following expression.

$$\tau_d = \frac{(T_A)\ C_p\ (T_A)\ y^2}{\lambda\ (T_A)} \qquad (7)$$

Typically, $\tau_T \simeq 10^{-3}$ sec; $\tau_\theta \simeq 10^{-4}$ sec; $\tau_p \simeq 10^{-5}$ sec; $\tau_g \simeq 10^{-3}$ sec; and $\tau_d \simeq 10^{-4}$ sec (with $\rho = 1.6$, $C_p = 500$, $\lambda = 0.3$, and $y = 10^{-3}$ m).

Model for Energy Transport

The radial spacing, ℓ, in a typical design is 2 mm. The radial variations will be neglected initially. The walls of the electrodes will be cooled and their surface temperature can be prescribed uniform = T_w. The task is to predict the temperature within the annulus, $T(x, \theta, t)$, given the arc temperature, T_A (measured from experiments). Radiative transport can be neglected, since argon is optically thin and the energy transport is primarily due to conduction and convection. The development of the annulus is shown in Fig. B.2. The arc occupies the position EFGH at time, t, as it moves downward with velocity, R , and to the right with velocity, u. Without loss of generality, we can assume that E coincided with A

at t = 0. It is found from the experiments on the gaseous electrode that τ_θ is always an order of magnitude less than τ_T. Physically, this means that the portion BCLK (Region II) in Fig. B.2 acquires energy from the arc much faster than the Regions I and III (ABKJ and CDML). Hence, in a time scale much larger than τ_θ, we can analyze the energy transport in the Regions I, II, and III separately in an approximate fashion; Region II will acquire energy from the arc and Regions I and III will acquire energy by conduction from the surfaces BEGK and CFHL, respectively. In what follows, we will further assume constant thermal conductivity and diffusivity for the sake of simplicity. It is possible to extend this analysis accounting for these variations (Ref. 1).

Analysis in Region II

The arc rotates with an angular velocity, ω_A, and the cold gas swirls with an angular velocity, ω_g, and $\omega_A > \omega_g$. It will be assumed that as the arc moves, the cold gas behind it fills in the region vacated by the arc, immediately. Or, in other words, the cold gas and the arc in Region II will be assumed to rotate like a solid body with an angular velocity, $\omega = (\omega_A - \omega_g)$ and the portions BCFE and GHLK acquire energy from the arc, EFGH, at the contant temperature, T_A. As arrived at earlier from momentum consideration, EF and EG are of the order of a mm. Hence, the variations in the x direction will be neglected in Region II. Let $\theta = 0$ at EF and $\theta = \theta_1$ at GH. θ_1 will be known from the dimensions of the arc and the mean radius of the annulus, R. The following energy conduction equation is valid in Region II in a frame of reference rotating with the arc with an angular velocity, $\omega = (\omega_A - \omega_g)$.

$$\frac{\partial T}{\partial t} = \frac{\alpha}{R^2} \frac{\partial^2 T}{\partial \theta^2} \tag{8}$$

where, $\alpha = \lambda/(\rho\, C_p)$ is the thermal diffusivity.

Or,

$$\frac{\partial T}{\partial t} = \alpha' \frac{\partial^2 T}{\partial \theta^2} \tag{9}$$

where, $\alpha' = \alpha/R^2$.

The boundary conditions for Equation (9) are as follows:

$$T(\theta, 0) = T_g \quad \text{(initial temperature of the cold gas)} \tag{10}$$

$$\left.\begin{aligned} T(0, t) &= T_A \\ T(\theta_1, t) &= T_A \end{aligned}\right\} \text{(temperature of the arc)}$$

We can Laplace transform as follows:

$$L(\theta) = \int_0^\infty T(\theta, t)\, e^{-st}\, dt \tag{11}$$

The following transformed equation results:

$$sL - T_g = \alpha' \frac{d^2L}{d\theta^2} \tag{12}$$

with the following transformed boundary conditions:

$$L(0) = L(\theta_1) = \frac{T_A}{s} \tag{13}$$

The solution of (12) with the b.c.'s (13) is:

$$L(\theta) = \frac{T_g}{s} + \frac{(T_A - T_g)}{s} \text{COSH } (q\theta) +$$

$$\frac{(T_A - T_g)}{s} \frac{\left[1 - \text{COSH } (q\theta_1)\right]}{\text{SINH } (q\theta_1)} \text{SINH } (q\theta) \tag{14}$$

where,

$$q = s/\alpha' \tag{14a}$$

The solution, T (θ, t) can be obtained by inverting (14) as follows:

$$T(\theta, t) = \frac{1}{2\pi i} \int_{\gamma-i\infty}^{\gamma+i\infty} e^{tz} L(\theta)\, dz = L^{-1}\{L(\theta)\} \tag{15}$$

with z replacing s in L(θ).

Inverting L(θ) term by term,

$$L^{-1} \left(\frac{T_g}{s}\right) = T_g \tag{16}$$

$$L^{-1} \left[\frac{(T_A - T_g)}{s} \text{COSH } (q\theta)\right] =$$

$$\frac{1}{2\pi i} \int_{\gamma-i\infty}^{\gamma+i\infty} e^{tz} \frac{(T_A - T_g)}{z} \text{COSH } \{(\frac{z}{\alpha'})^{\frac{1}{2}} \theta\}\, dz \tag{17}$$

The COSH function is even and single valued; the integrand has a simple pole at z = 0. Equation (17) reduces to:

$$e^{tz} (T_A - T_g) \text{COSH } \{(\frac{z}{\alpha'})^{\frac{1}{2}} \theta\}_{z=0} = (T_A - T_g) \tag{18}$$

Result (18) was confirmed by Ref. (2).

Inversion of the third term in Equation (14):

$$\frac{1}{2\pi i}\int_{\gamma-i\infty}^{\gamma+i\infty} e^{tz}\,\frac{(T_A - T_g)}{z}\left[\frac{1 - \text{COSH}\,\{(\frac{z}{\alpha'})^{\frac{1}{2}}\,\theta_1\}}{\text{SINH}\,\{(\frac{z}{\alpha'})^{\frac{1}{2}}\,\theta_1\}}\right] *$$

$$\text{SINH}\,\{(\frac{z}{\alpha'})^{\frac{1}{2}}\,\theta\}\,dz \qquad (19$$

The integrand in (19) is single valued. $z = 0$ is not a pole, since the integrand is finite at $z = 0$. There are infinite number of simple poles describe below:

$$z = -\alpha'\,\mu_n^2$$

and,
$$\mu_n = \frac{(n+1)\pi}{\theta_1} \qquad n = 0, 1, 2 \ldots \infty \qquad (20$$

The residue at $z = -\alpha'\,\mu_n^2$ is (Ref. 1)

$$= \frac{-4\,e^{-(\alpha'\mu_n^2 t)}\,(T_A - T_g)\,\text{SIN}\,(\mu_n\theta)}{\mu_n\,\theta_1} \qquad (21$$

The integral (19) is the sum of all the residues given by (21). After some algebra, the integral (19) is

$$= -\sum_{n=0}^{\infty}\frac{4\,e^{-(\alpha'\mu_n^2 t)}\,(T_A - T_g)\,\text{SIN}\,(\mu_n\theta)}{\mu_n\,\theta_1} \qquad (22$$

with,
$$\mu_n = \frac{(2n+1)\,\pi}{\theta_1} \qquad (22.$$

The difference between (20) and (22a) is due to the fact that the residue is zero at half the number of the poles. The solution $T(\theta,t)$ in Region II is obtained by adding (16), (18), and (22) to yield,

$$T(\theta,t) = T_A - \frac{4}{\theta_1}\,(T_A - T_g)\sum_{n=0}^{\infty}\frac{1}{\mu_n}\,\text{SIN}\,(\mu_n\theta)\,e^{-\alpha'\mu_n^2 t} \qquad (23)$$

with,
$$\mu_n = \frac{(2n+1)\pi}{\theta_1}$$

and,

$$\alpha' = \frac{\lambda}{\rho\ C_P\ R}$$

The solution from $\theta = 0$ to θ_1 is $T = T_A$. Equation (23) is valid for $\theta = \theta_1$ to 2π. It should be noted that (23) is the solution in a frame rotating at an angular velocity, $\omega = \omega_A - \omega_g$.

Solution in Region I

The energy input to this region is by conduction from BEGK at a temperature given by (23). The side, AJ, is at the temperature of the electrode walls, T_w. The cold gas with an initial temperature, T_g, swirls with an angular velocity, ω_g, in this region. The governing equation in this region is as follows:

$$\rho\ C_P\ \left(\frac{\partial T}{\partial t} + \omega_g \frac{\partial T}{\partial \theta}\right) = \lambda \frac{\partial^2 T}{\partial x^2} + \frac{\lambda}{R^2} \frac{\partial^2 T}{\partial \theta^2} \tag{24}$$

In the azimuthal direction, θ, the convective transport described by the second term on the left hand side, is found to dominate conduction described by the second term on the right. Hence, Equation (24) can be further simplified and written as follows:

$$\frac{\partial T}{\partial t} + \omega_g \frac{\partial T}{\partial \theta} = \alpha \frac{\partial^2 T}{\partial x^2} \tag{25}$$

where,

$$\alpha = \frac{\lambda}{\rho\ C_P} \tag{25a}$$

The boundary conditions for (25) are at $x = 0$, $T = T_w$.

$$\text{At } x = ut \ \{\text{surface BK, } T = T_s\ (\theta,\ t)\} \tag{26}$$

where $T_s\ (\theta,\ t)$ is given by (23) reduced to a stationary frame and u is the velocity of the arc in the x direction. Equation (26) with b.c.'s (26) can be solved as follows:

$$\text{Transform x to X with } X = \frac{\pi X}{ut} \tag{27}$$

Then,

$$\frac{\partial T}{\partial t} + \omega_g \frac{\partial T}{\partial \theta} = \frac{\alpha \pi^2}{u^2 t^2} \frac{\partial^2 T}{\partial X^2} \tag{28}$$

Fourier transforms T as follows (Ref. 3).

$$F_n = \int_0^{\pi} T\ \text{SIN}\ (nX)\ dX \qquad n = 1,\ 2,\ \ldots,\ \infty \tag{29}$$

$$\frac{\partial F_n}{\partial t} + \omega_g \frac{\partial F_n}{\partial \theta} = \frac{\alpha \pi^2}{u^2 t^2} - \left[n^2\ F_n\ (\theta, t) + n\{T_w - (-1)^n\ T_s(\theta, t)\}\right] \tag{30}$$

Using the method of characteristics (Ref. 4), Equation (30) can be split into ordinary differential equations as follows:

$$dt = \frac{d\theta}{\omega_g} = \frac{dF_n}{\frac{\alpha\pi^2}{u^2t^2}\left[-n^2 F_n(\theta,t) + n\{T_w - (-1)^n T_s(\theta,t)\}\right]} \tag{31}$$

Equation (31) can be solved numerically by the Runge-Kutta technique, to obtain $F_n(\theta,t)$ for all n's.

T (θ,t) in Region I is obtained by taking the inverse Fourier transform as follows:

$$T(X, \theta, t) = \frac{2}{\pi} \sum_{n=1}^{\infty} F_n(\theta, t) \text{ SIN } (nX) \tag{32}$$

or,
$$T(x, \theta, t) = \frac{2}{\pi} \sum_{n=1}^{\infty} F_n(\theta, t) \text{ SIN } \left(\frac{n\pi x}{ut}\right)$$

Solution in Region III

This solution is similar to that in Region I except that the boundary conditions are different. They are:

$$\begin{aligned} &\text{at } x = ut + d, \quad T = T_s(\theta, t) \\ &\text{at } x = L, \qquad T = T_w \end{aligned} \tag{33}$$

where d is the diameter of the arc and L is the length of the electrode. The governing equation is the same (Equation 25). The solution is similar to that in Region I.

PREDICTION OF THE VELOCITY AND TEMPERATURE PROFILES AT THE SLOT C-D

The temperature profile at the slot C-D is known from the analysis in the previous section. Knowing the equation of state of the gas, a density profile follows from the temperature profile. We can average the density across the slot C-D and get a variation of the average density, $\overline{\rho}$, with time, $\overline{\rho}(t)$. The velocity profile, b (t), follows from mass conservation

$$\overline{\rho}(t)\, v(t)\, A_s = \dot{m} \tag{34}$$

where A_s = the area of the slot and m is the mass flow rate of the gas.

At the end of the reporting period, computations based on the above model were yet to be performed.

REFERENCES

1. Arpaci, V. S., *Conduction Heat Transfer*, Addison-Wesley, Reading, Mass., 1966.

2. Kaufman, H., Department of Mathematics, McGill University, Private Communication, 1979.

3. Churchill, R. V., *Operational Mathematics*, McGraw-Hill Book Company, New York, 1958.

4. Hildebrand, F. B., *Advanced Calculus for Applications*, Prentice-Hall, New Jersey, 1962.

APPENDIX C

SUMMARY OF MHD GENERATOR TESTS OF ONE-FOURTH INCH CATHODE ARC GASEOUS ELECTRODE ASSEMBLY

SUMMARY OF MHD GENERATOR TESTS OF ONE-FOURTH INCH CATHODE ARC GASEOUS ELECTRODE ASSEMBLY

May 1, 1979

Fuel:	Propane
Test Frame:	Gaseous electrode (tungsten cathode)
Purpose:	To test diffuser repairs and high pressure propane pump.
Test Results:	Diffuser and combustor were rebrazed following failure during previous run. For the first time, propane booster pump was run to get high flow rates. Propane flow rate of 4.8 gpm was achieved. Cooling water outlet temperatures were about 46°C. Maximum open circuit voltage was 33 volts at 3.5 Tesla and approximately 1 kg/sec flow.

May 2, 1979

Fuel:	Diesel
Test Frame:	Gaseous electrode (copper cathode)
Purpose:	Setting of cooling water flow rates.
Test Results:	Gaseous electrode frame insulator burned and so the hot gas came out through the insulator gap.

May 8, 1979

Fuel:	Diesel
Test Configuration:	Flow straighteners are placed back into the system
Test Frame:	Solid electrode
Purpose:	To set cooling water flow rates.
Test Results:	With the first set of cooling water flow rates, the diffuser cooling water outlet temperature went to about 67°C at 2.48 gpm of diesel flow. Therefore, the cooling water flow was increased in the diffuser cooling circuit. With the increased cooling water flow rate, the outlet temperature of the water was 62°C at 2.49 gpm of diesel flow. The fuel flow was increased further up to 3.465 gpm, the outlet temperature of the cooling water for combustor, channel, diffuser, and nozzle were 69°C, 66.7°C, 69°C and 58.3°C, respectively. From our earlier attempts to run the generator, it has been observed that it is necessary to maintain the cooling water outlet temperature around 65 - 70°C to generate any reasonable amount of voltage. Therefore, the second set of cooling water flow rates were considered sufficient to run the generator.

May 9, 1979

Fuel (a):	Diesel
Test Frame:	Solid electrode
Purpose:	To establish MHD generator flow conditions for gaseous electrode (GE) test.
Test Results:	O_2/N_2 approximately 1.0. Seed 1% by weight. With a total flow rate of 1.1236 kg/sec and B-field of 3.8 Tesla, an open circuit voltage of 503 volts and a short circuit current of 19 amps were obtained. Cooling water outlet temperatures were between 65 to 70°C.
Fuel (b):	Propane
Test Frame:	Solid electrode
Purpose:	To determine MHD generator conditions for GE test.
Test Results:	O_2/N_2 approximately 1.0. Seed flow approximately 1% by weight. With a total flow rate of 1.134 kg/sec and B-field of 3.8 Tesla, an open circuit voltage of 342 volts and a short circuit current of 9.2 amps were obtained. Cooling water outlet temperatures were between 57 to 63°C.

May 16, 1979

Fuel:	Diesel
Test Frame:	Gaseous electrode (tungsten cathode)
Purpose:	To test the gaseous electrode in the generator.
Test Results:	First the tungsten cathode electrode ran for 2-3 minutes in situ at 1 to 3.5 Tesla fields without the MHD gas flowing. Then the combustor was started to test it under actual MHD flow conditions. After a few seconds, the system was shut down since an arc was observed between the flanges at inlet to diffuser. It was later found that the cooling water was leaking.

May 21, 1979

Fuel:	Diesel
Test Frame:	Gaseous electrode (copper cathode)
Purpose:	To test the gaseous electrode with copper cathode in MHD generator.
Test Results:	With N_2/O_2 approximately 1.0, seed flow of 1.13% K by weight, and 1.19 kg/sec gas flow, an open circuit voltage of 608 volts and a short circuit current of 23 amperes were obtained. The cooling water outlet temperature for the combustor, channel, and diffuser were 73, 66, and 72°C, respectively. For the first time, the copper cathode operated satisfactorily through the generator test, i.e., for about 25 minutes.

May 24, 1979

Fuel: Diesel

Test Frame: Gaseous electrode (copper cathode)

Purpose: To test the gaseous electrode under increased MHD interaction and to take a movie of the arc operation. The experiment was done with lower N_2/O_2 values. The results on May 21 indicated for N_2/O_2 approximately 1.0, and B-field of 3.8 Tesla, the open circuit voltage of 608 volts and short circuit current of 23.15 amps were obtained.

Test Results: By reducing (N_2/O_2) to 0.53 and keeping the total flow rate to 1.16 kg/sec, the maximum open circuit voltage of 1000 volts (transient) and a steady value of 800 volts were obtained. A short circuit current of greater than 100 amps was obtained. The B-field was 3.8 Tesla. The arc gaseous electrode was operated for more than 30 minutes under MHD operating conditions. A Fastax movie was taken of the arc gaseous electrode operation using the fiber optic system. The pressure profiles and voltage distribution were obtained. The split plate current for the gaseous electrode frame was observed to be higher in comparison with the values for other solid electrode frames.

TABLE C.1

MHD TEST DATA

Test Date: May 1, 1979

Flow Conditions:

Fuel:	Propane
Oxidizer:	Oxygen
Diluent:	Nitrogen
Seed Material:	KOH in CH_3OH
Amount of Seed:	0.6 - 1.2% K
Electrode:	Tungsten Cathode

Flow Rates for Full Power with N_2/O_2 = 1 and 1.5% K Seed

$\dot{m}_f$ = 0.141 kg/sec
$\dot{m}_o$ = 0.512 kg/sec
$\dot{m}_n$ = 0.448 kg/sec
$\dot{m}_s$ = 0.068 kg/sec

$\dot{m}_f$ kg/sec	$\dot{m}_o$ kg/sec	$\dot{m}_n$ kg/sec	$\dot{m}_s$ kg/sec	B Tesla	V_{oc} Volts	I_{sc} Amps
0.154	0.563	0.145	0.039	3.0	32	---
0.155	0.546	0.138	0.039	3.0	---	0.1
0.153	0.714	0.199	0.052	3.5	33.5	---

TABLE C.2

MHD TEST DATA

Test Date: May 9, 1979

Flow Conditions:

Fuel:	Propane
Oxidizer:	Stoichiometric amount of oxygen
Diluent:	nitrogen, N_2/O_2 = 1.0 by volume
Seed Material:	35% KOH in CH_3OH
Amount of Seed:	~1% potassium in flow by weight
Electrode:	Solid copper electrode

Flow Rates for Full Power with N_2/O_2 = 1 and 1.5% K Seed

$\dot{m}_f$ = 0.141 kg/sec
$\dot{m}_o$ = 0.512 kg/sec
$\dot{m}_n$ = 0.448 kg/sec
$\dot{m}_s$ = 0.068 kg/sec

$\dot{m}_f$ kg/sec	$\dot{m}_o$ kg/sec	$\dot{m}_n$ kg/sec	$\dot{m}_s$ kg/sec	B Tesla	V_{oc} Volts	I_{sc} Amps
0.141	0.445	0.512	0.04	2.0	120.5	---
0.141	0.446	0.511	0.04	2.0	---	1.95
0.141	0.445	0.513	0.04	2.0	118.5	---
0.141	0.444	0.512	0.05	3.0	300	---
0.141	0.444	0.512	0.04	3.0	---	5.6
0.141	0.443	0.511	0.04	3.8	341.5	---
0.140	0.443	0.510	0.04	3.8	---	9.2

Cooling Water Temperatures:

Combustor: T inlet - 50.5°C
T outlet - 57.8°C

Channel: T inlet - 48.5°C
T outlet - 61.7°C

TABLE C.3

MHD TEST DATA

Test Date: May 9, 1979

Flow Conditions:

Fuel:	Diesel
Oxidizer:	Stoichiometric amount of oxygen
Diluent:	Nitrogen, N_2/O_2 = 1.0 by volume
Seed Material:	35% KOH in CH_3OH
Amount of Seed:	0.9% potassium in flow by weight
Electrode:	Solid copper electrode

Flow Rates for Full Power with N_2/O_2 = 1 and 1.5% K Seed

$\dot{m}_f$ = 0.148 kg/sec
$\dot{m}_o$ = 0.508 kg/sec
$\dot{m}_n$ = 0.444 kg/sec
$\dot{m}_s$ = 0.068 kg/sec

$\dot{m}_f$ kg/sec	$\dot{m}_o$ kg/sec	$\dot{m}_n$ kg/sec	$\dot{m}_s$ kg/sec	B Tesla	V_{oc} Volts	I_{sc} Amps
0.146	0.44	0.506	0.04	2.0	229	---
0.145	0.44	0.504	0.04	2.0	---	6.6
0.146	0.44	0.502	0.04	3.0	377	---
0.147	0.44	0.50	0.04	3.0	---	15.85
0.146	0.44	0.502	0.04	3.8	503.5	---
0.146	0.44	0.50	0.04	3.8	---	18.95

Cooling Water Temperatures:

Combustor: T inlet - 54.5°C
T outlet - 71.4°C

Channel: T inlet - 50.5°C
T outlet - 66.4°C

TABLE C.4

MHD TEST DATA

Test Date: May 21, 1979

Flow Conditions:

Fuel:	Diesel
Oxidizer:	Oxygen
Diluent:	Nitrogen
Seed Material:	KOH in CH_3OH
Amount of Seed:	0.6 - 1.13% K
Electrode:	Arc gaseous electrode (copper cathode)

Flow Rates for Full Power with N_2/O_2 = 1 and 1.5% K Seed

$\dot{m}_f$ = 0.148 kg/sec
$\dot{m}_o$ = 0.508 kg/sec
$\dot{m}_n$ = 0.444 kg/sec
$\dot{m}_s$ = 0.068 kg/sec

$\dot{m}_f$ kg/sec	$\dot{m}_o$ kg/sec	$\dot{m}_n$ kg/sec	$\dot{m}_s$ kg/sec	B Tesla	V_{oc} Volts	I_{sc} Amps
0.146	0.561	0.441	0.028	3.0	510	---
0.146	0.560	0.441	0.031	3.0	---	13.05
0.146	0.559	0.438	0.050	3.0	---	15.25
0.146	0.560	0.440	0.049	3.0	441	---
0.146	0.558	0.438	0.051	3.8	522.5	---
0.146	0.557	0.437	0.050	3.8	---	23.15
0.146	0.557	0.436	0.051	3.8	608	---
0.105	0.371	0.347	0.043	3.0	488	---

TABLE C.5

MHD TEST DATA

Test Date: May 24, 1979

Flow Conditions:

Fuel:	Diesel
Oxidizer:	Oxygen
Diluent:	Nitrogen
Seed Material:	KOH in CH_3OH
Amount of Seed:	~ 1.17% K
Electrode:	Arc gaseous electrode (AGE)

Flow Rates for Full Power with N_2/O_2 = 1 and 1.5% K Seed

$\dot{m}_f$ = 0.148 kg/sec
$\dot{m}_o$ = 0.508 kg/sec
$\dot{m}_n$ = 0.444 kg/sec
$\dot{m}_s$ = 0.068 kg/sec

$\dot{m}_f$ kg/sec	$\dot{m}_o$ kg/sec	$\dot{m}_n$ kg/sec	$\dot{m}_s$ kg/sec	B Tesla	V_{oc} Volts	I_{sc} Amps
0.105	0.372	0.349	0.004	1.49	50.5	---
0.130	0.459	0.414	0.004	1.50	33.5	---
0.146	0.538	0.447	0.004	1.51	25	---
0.146	0.538	0.444	0.038	1.50	78	---
0.146	0.537	0.443	0.038	3.03	287.5	---
0.183	0.650	0.297	0.048	3.04	680.5	---
0.183	0.650	0.297	0.048	3.04	---	73.75
0.183	0.648	0.297	0.048	3.82	794	---
0.183	0.648	0.296	0.048	3.81	---	89.85
0.183	0.648	0.296	0.049	3.81	20	81.2
0.181	0.639	0.295	0.053	3.83	749	---
0.181	0.637	0.294	0.051	3.82	670.5	---
Electrode: No arc but purge flow						
0.183	0.654	0.281	0.047	3.83	862.5	---
0.183	0.653	0.282	0.047	3.82	---	>110
0.183	0.651	0.281	0.038	3.82	826	---
0.183	0.653	0.282	0.037	3.06	759	---

TABLE C.6

MHD TEST DATA

Test Date: June 28, 1979

Flow Conditions:

Fuel:	Diesel
Oxidizer:	Oxygen
Diluent:	Nitrogen
Seed Material:	KOH in CH_3OH
Amount of Seed:	1 - 1.5% K
Electrode:	Gaseous electrode (copper cathode)

Flow Rates for Full Power with N_2/O_2 = 1 and 1.5% K Seed

$\dot{m}_f$ = 0.141 kg/sec
$\dot{m}_o$ = 0.512 kg/sec
$\dot{m}_n$ = 0.448 kg/sec
$\dot{m}_s$ = 0.068 kg/sec

$\dot{m}_f$ kg/sec	$\dot{m}_o$ kg/sec	$\dot{m}_n$ kg/sec	$\dot{m}_s$ kg/sec	B Tesla	V_{oc} Volts	I_{sc} Amps
0.146	0.495	0.278	0.051	3.56	865	---
0.146	0.494	0.278	0.051	3.56	815	---
0.146	0.494	0.277	0.055	3.56	345	30.5
0.146	0.493	0.278	0.055	3.56	---	41.5
0.146	0.494	0.278	0.055	3.56	845	---
0.147	0.512	0.274	0.055	3.56	785	---
0.147	0.509	0.274	0.057	3.56	815*	---
0.147	0.510	0.274	0.057	3.56	340*	35
0.147	0.511	0.274	0.056	3.55	---	45.5*
0.147	0.509	0.274	0.057	3.44	885*	---
0.147	0.508	0.274	0.057	3.54	840*	---
0.115	0.394	0.364	0.058	0.43	35	---
0.146	0.505	0.281	0.069	3.56	790*	---
0.147	0.506	0.281	0.061	3.56	780x	---
0.146	0.506	0.281	0.061	3.56	325x	34.5
0.146	0.505	0.281	0.061	3.56	---	49.5x
0.146	0.505	0.281	0.061	3.56	730x	---
0.190	0.632	0.236	0.056	3.81	785*	---
0.189	0.631	0.232	0.056	3.81	560*	60.5
0.190	0.631	0.230	0.056	3.81	---	127*

*No AGE but with argon flow
xNo arc and no argon

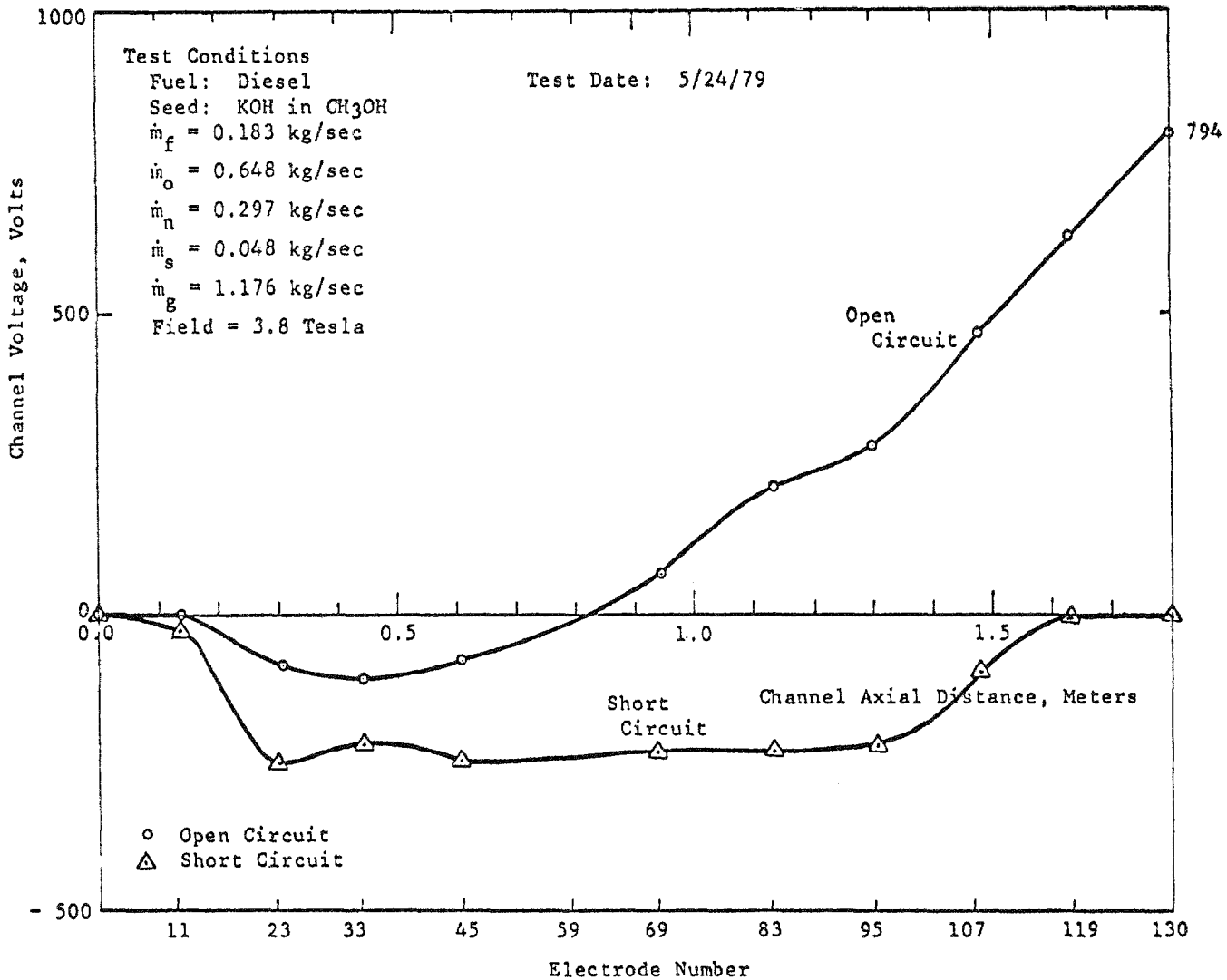

Fig. C.1 Voltage Profile in the Channel